

AD-A260 957



ION PAGE

Form Approved
OASD No. 0704-0188

(2)

ago 1 hour per response, including the time for reviewing instructions, searching existing data sources, collection of information. Send comments regarding this burden estimate or any other aspect of this information Headquarters Service, Directorate for Information Operations and Reports, 1215 Jefferson Avenue and Budget, Paperwork Reduction Project (0704-0188), Washington, DC 20303.

1. AGENCY USE ONLY (Leave blank)

2. REPORT DATE

20 January 1993

3. REPORT TYPE AND DATES COVERED

Final Technical 89/11/1 - 92/10/31

4. TITLE AND SUBTITLE

(U) Flame-Turbulence Interactions

5. FUNDING NUMBERS

PE - 61102F

PR - 2308

SA - BS

G - AFOSR 90-0025

6. AUTHOR(S)

Domenic A Santavicca

7. PERFORMING ORGANIZATION NAME(S) AND ADDRESS(ES)

Pennsylvania State University
Mechanical Engineering Department
University Park PA 16802

8. PERFORMING ORGANIZATION
REPORT NUMBER

AFOSR

3

9. SPONSORING/MONITORING AGENCY NAME(S) AND ADDRESS(ES)

AFOSR/NA
110 Duncan Avenue, Suite B115
Bolling AFB DC 20332-0001

10. SPONSORING/MONITORING
AGENCY REPORT NUMBER

11. SUPPLEMENTARY NOTES

DTIC
ELECTE
MAR 09 1993
S E D

12a. DISTRIBUTION/AVAILABILITY STATEMENT

Approved for public release; distribution is
unlimited

12b. DISTRIBUTION CODE

13. ABSTRACT (Maximum 200 words)

The interaction between individual vortices and a premixed laminar flame was investigated in order to characterize the underlying dynamics of flame-turbulence interactions and thereby gain an improved understanding of premixed turbulent flames. In addition, previous two-dimensional flame structure measurements made in turbulent premixed flames were re-analyzed in order to obtain flame curvature and orientation statistics.

93-04940

93 3 8 060



11609

14. SUBJECT TERMS

Premixed Turbulent Flames, Flame-Vortex Interactions,
Turbulence-Flame Interactions, Turbulent Flame Structure

15. NUMBER OF PAGES

118

16. PRICE CODE

17. SECURITY CLASSIFICATION
OF REPORT

Unclassified

18. SECURITY CLASSIFICATION
OF THIS PAGE

Unclassified

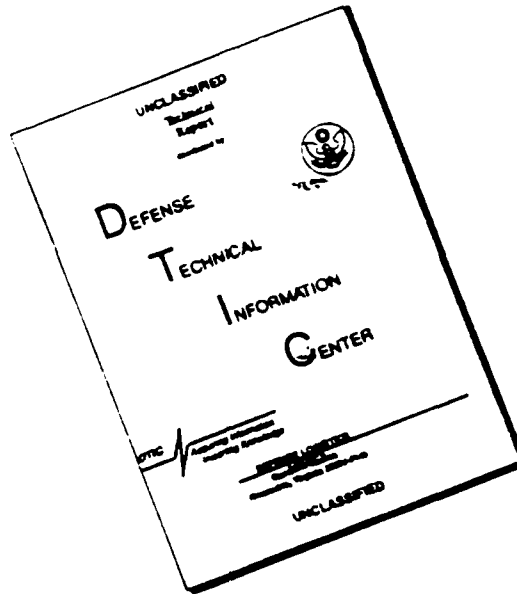
19. SECURITY CLASSIFICATION
OF ABSTRACT

Unclassified

20. LIMITATION OF ABSTRACT

UL

DISCLAIMER NOTICE



THIS DOCUMENT IS BEST QUALITY AVAILABLE. THE COPY FURNISHED TO DTIC CONTAINED A SIGNIFICANT NUMBER OF PAGES WHICH DO NOT REPRODUCE LEGIBLY.

TABLE OF CONTENTS

	<u>Page</u>
Cover Page	1
Table of Contents	2
Research Objectives	3
Research Results	3
Publications	7
Professional Personnel	7
Interactions	8
Appendix A: "Curvature and Orientation Statistics of Turbulent Premixed Flame Fronts," by T.-W. Lee, G. L. North and D. A. Santavicca, <i>Combustion Science and Technology</i> , Vol 84, pp. 121-132, 1992	9
Appendix B: "Surface Properties of Turbulent Premixed Propane/Air Flames at Various Lewis Numbers," by T.-W. Lee, G. L. North and D. A. Santavicca. Submitted to <i>Combustion and Flame</i>	21
Appendix C: "Flame Front Geometry and Stretch During Interactions of Premixed Flames with Vortices," by T.-W. Lee and D. A. Santavicca. Accepted for Publication in <i>Combustion Science and Technology</i>	50
Appendix D: "Local Response and Surface Properties of Premixed Flames During Interactions with Kármán Vortex Streets," by T.-W. Lee, J. G. Lee, D. A. Nye and D. A. Santavicca. Submitted to <i>Combustion and Flame</i>	85

Accession For	
NTIS CRA&I	<input checked="" type="checkbox"/>
DTIC TAB	<input type="checkbox"/>
Unannounced	<input type="checkbox"/>
Justification	
By	
Distribution /	
Availability Codes	
Dist	Avail and / or Special
A-1	

RESEARCH OBJECTIVES

There are a number of important, and to date unresolved, issues related to the structure and the propagation of premixed turbulent flames, including their geometric properties, the effect of flame stretch and Lewis number, and the sources of flame-generated turbulence. In order to address these issues, a more fundamental understanding of flame-turbulence interactions is required. In this study, the interaction between individual vortices and a premixed laminar flame was investigated in order to characterize the underlying dynamics of flame-turbulence interactions and thereby gain an improved understanding of premixed turbulent flames. In addition, previously obtained two-dimensional flame structure measurements made in turbulent premixed flames were re-analyzed in order to obtain flame curvature and orientation statistics.

RESEARCH RESULTS

The results of this research are described in detail in four papers which are included as Appendices A through D of this report. The first and second papers are entitled, "Curvature and Orientation Statistics of Turbulent Premixed Flame Fronts" and "Surface Properties of Turbulent Premixed Propane/Air Flames at Various Lewis Numbers," respectively, and present results of an analysis of previously reported flame structure measurements made over a range of u'/S_L from 1.42 to 5.71, and Le from 0.98 to 1.86. These are the same measurements for which we previously reported fractal dimensions, but now have re-analyzed in terms of flame curvature and orientation statistics in order to provide data which is more consistent with recent numerical predictions such as those of Pope, Poinso, and others. The major conclusions which we have drawn from this work are as follows:

- (1) The flamelet curvature distributions are symmetric with respect to the zero mean and can be approximated by Gaussian distributions.
- (2) The mean positive (negative) flamelet curvature increases (decreases) with increasing u'/S_L , and is governed by a nearly square-root dependence on u'/S_L .

- (3) The mean flamelet radius of curvature is approximately twice the Taylor scale of turbulence in the approach flow, suggesting that the length scale of turbulence has a more important role than u'/S_L or Le in determining the flame curvature.
- (4) The flame orientation exhibits an evolution from anisotropy toward a more uniform distribution with increasing u'/S_L at a similar rate for all Lewis numbers tested, and isotropy is estimated to occur for $u'/S_L \approx 10$.
- (5) The flame surface area ratio, P_T/P_L , is observed to vary from 2.9 to 5.2 when u'/S_L is increased from 1.42 to 5.71, while thermodynamically unstable mixtures ($Le < 1$) exhibit larger flame surface area by up to 30% in comparison to flames with $Le > 1$.
- (6) Pockets of both reactants and product gases in two-dimensional images are observed at the conditions studied accounting for up to 25% of the total flame area with the fraction of flame pocket area tending to be larger for $Le < 1$.

The third and fourth papers are entitled, "Flame Front Geometry and Stretch During Interactions of Premixed Flames with Vortices" and "Local Response and Surface Properties of Premixed Flames During Interaction with Kármán Vortex Streets," respectively, and present results from our study of flame-vortex interactions. The motivation for this work being the notion that the interaction between an individual vortex and a premixed laminar flame front can be viewed as the basic "building block" from which to develop an improved understanding of the underlying processes involved in flame-turbulence interactions. This work was initially intended to be entirely experimental; however, we have also had considerable success in developing a relatively simple model based on a kinematical relationship between convection due to fluid motion and normal flame propagation. From the experimental and numerical results obtained to date, we have drawn the following major conclusions:

- (1) The flame front geometry during the interaction of premixed laminar flames with Kármán vortex streets can be simulated by a kinematical relationship between

convection and flame propagation, although for quantitatively accurate reconstruction, the effect of the flame on the vortex properties needs to be considered.

- (2) Vortex strength, size and spacing are important parameters in determining the geometry of the wrinkled flame fronts; in particular, vortex spacing parallel and perpendicular to the flame affect the spatial frequency and the time for development of the wrinkled structures, respectively.
- (3) Flame stretch during flame-vortex interactions is non-uniform in space and time, with flow strain and curvature effects causing a spatial fluctuation from positive to compressive flame stretch while the overall flame stretch is positive and time-dependent.
- (4) Local flame properties during interactions with vortices exhibit responses consistent with the results of stretched laminar flame theories in that the OH LIF intensity increases when the local flame curvature becomes positive (negative) for thermodynamically unstable (stable) flames.
- (5) Departure of the peak OH LIF intensity for hydrogen flames ranges from 20 to 150% of the value for unstretched flames (zero flame curvature) for flame curvature ranging from -1.5 to 0.7 mm^{-1} , while for propane/air flames, the variation is within $\pm 20\%$ of the value at zero curvature. Thus, the widely-used approximation of assigning constant local flame speed in turbulent premixed flames may be subject to significant errors for hydrogen flames for which the magnitude of $(1/Le-1)$ is relatively large, while for typical hydrocarbon flames, this approximation appears to be more reasonable.
- (6) The variation in the averaged peak OH LIF intensity is nearly linear with respect to a variation in flame curvature from -1.2 to 0.8 mm^{-1} , indicating that the application of stretched laminar flame theory to turbulent premixed flames in which the local flame speed is a linear function of the flame stretch and Markstein length is reasonably accurate.

- (7) The flame area during interactions with Kármán vortex streets increases as a relatively weak function of u_0/S_L , while the vortex size affects the flame area, in that smaller vortices are less effective in generating flame area. The effect of Lewis number on the flame front is to enhance (suppress) the amplitude of the wrinkles generated by vortices for thermodynamically unstable (stable) flames, thus resulting in larger (smaller) flame area.
- (8) The flame curvature pdf's for flames interacting with Kármán vortex streets exhibit a bias toward positive flame curvature due to the large area of positively-curved flame elements that develop downstream along the V-flame. A decrease in vortex size tends to increase the flame curvature and thus broaden the pdf's, while u_0/S_L and Lewis number have relatively small effects on the flame curvature pdf's.
- (9) The flame orientation distribution is peaked near the normal direction of flame propagation for small u_0/S_L , while an increase in u_0/S_L results in broadening of the flame orientation distribution and a shift toward larger flame angle due to the increased distortions in the flame front and increases in the effective flame propagation speed, respectively. An increase in the vortex size and decrease of Lewis number below unity for similar reasons results in broadening and a shift of the flame orientation distributions, although the effect is not as pronounced.

PUBLICATIONS

Videto, B. D. and Santavicca, D. A., "A Turbulent Flow System for Studying Turbulent Combustion Processes," *Comb. Sci. and Tech.* 76:159-164 (1991).

Lee, T.-W., North, G. L. and Santavicca, D. A., "Curvature and Orientation Statistics of Turbulent Premixed Flame Fronts," *Spring Meeting of the WSSCI*, March 1991.

Nye, D. A. and Santavicca, D. A., "Two Color Particle Image Velocimetry," *Fall Meeting of the ESSCI*, October 1991.

Lee, T.-W., Lee, J. G., Nye, D. A., and Santavicca, D. A., "Interaction of Premixed Flames with Kármán Vortex Streets," *Fall Meeting of the ESSCI*, October 1991.

Lee, T.-W., North, G. L. and Santavicca, D. A., "Curvature and Orientation Statistics of Turbulent Flame Fronts," *Comb. Sci. and Tech.*, Vol. 84, pp. 121-132 (1992).

Lee, T.-W. and Santavicca, D. A., "A Numerical Investigation of Premixed Flame Fronts Interacting with Vortices," *Spring Meeting of the CSSCI*, March 1992.

Lee, T.-W. and Santavicca, D. A., "Flame Front Geometry and Stretch During Interactions of Premixed Flames with Vortices," Accepted for publication in *Comb. Sci. and Tech.* (1992).

Lee, T.-W., North, G. L. and Santavicca, D. A., "Surface Properties of Turbulent Premixed Propane/Air Flames at Various Lewis Numbers," submitted to *Comb. and Flame* (1992).

Lee, T.-W., Lee, J. G., Nye, D. A. and Santavicca, D. A., "Local Response and Surface Properties of Premixed Flames During Interactions with Kármán Vortex Streets," submitted to *Comb. and Flame* (1992).

Nye, D. A. and Santavicca, D. A., "Two-Color, Low Noise Particle Image Velocimetry," submitted to *Experiments in Fluids* (1992).

North, G. L., Lee, T.-W. and Santavicca, D. A., "Measurements of Small-Scale Flame Structures (Inner Cutoffs) in Turbulent Premixed Flames," submitted to *Comb. Sci. and Tech.* (1993).

PROFESSIONAL PERSONNEL

Prof. D. A. Santavicca, Principal Investigator

Dr. T.-W. Lee, Research Associate

Mr. J. G. Lee, Graduate Student

Dr. G. L. North, (AFRAPT Trainee), Ph.D. completed January 1992

Mr. D. A. Nye, Graduate Student (AFRAPT Trainee)

Dr. B. D. Videto, Ph.D. completed January 1992

INTERACTIONS

Results from this research have been presented to a number of university, government and industrial organizations through the following seminars:

"Gas Turbine Combustion Research at Penn State," presented at General Electric Corporate Research and Development Labs in April, 1990.

"Gas Turbine Combustion Research at Penn State," presented at General Electric Aircraft Engines in May, 1990.

"Gas Turbine and Liquid Rocket Related Combustion Research at Penn State, presented at Pratt & Whitney, Florida in September, 1990.

"Flame-Vortex Interactions," presented at DoE-sponsored DHC Meetings (involving participants from Ford, Chrysler, and Texaco), at Sandia in April 1991 and at Penn State in October, 1991.

"Flame-Turbulence Interactions," presented at Princeton University in April, 1992.

"Flame-Turbulence Interactions," presented at Massachusetts Institute of Technology in May, 1992.

"Flame-Vortex Interactions," presented at DoE-Sponsored STAR Meeting on Turbulent Reacting Flows at Cornell University in November, 1992.

Collaborative research programs have also been initiated with General Electric, both the Power Generation Division in Schenectady and the Aircraft Engine Division in Evandale. These programs pertain to the inter-relationship between fuel-air mixing, flame stabilization and NO_x/CO emissions in premixed gas turbine combustors. These programs are a direct outgrowth of this AFOSR-funded study of premixed turbulent flames. Funding for this work is being provided by GE Power Generation and GE Aircraft Engines. Meetings have been held at GE Schenectady (January and October 1991), at NASA Lewis (January 1991 and November 1992), and at Penn State (June 1991) to discuss this research. Four graduate students have been involved in this program, three of which were supported by the AFRAPT Program.

APPENDIX A

Curvature and Orientation Statistics of Turbulent Premixed Flame Fronts

T.-W. LEE, G. L. NORTH and D. A. SANTAVICCA *Turbulent Combustion Laboratory, Propulsion Engineering Research Center, Department of Mechanical Engineering, Penn State University*

(Received April 23, 1991; in final form September 17, 1991)

Abstract—The curvature of turbulent premixed flame fronts is an important spatial property that needs to be quantified over a range of turbulence conditions. In this study, measurements of flamelet curvature along with orientation statistics for $u'/S_L = 1.42$ – 5.71 are obtained from OH planar laser-induced fluorescence images of the flame boundary by applying a curve-tracing difference formula with interval length of the order of the inner cutoff scale. Use of this particular interval length is essential for accurate tracing of the flame boundary with implicit filtering of extraneous noise that can introduce significant errors in the curvature measurements. The distributions of flamelet curvature are found to be symmetric with respect to the zero mean, while the variance increases with increasing u'/S_L . These distributions can be approximated by Gaussian distribution functions. The positive and negative mean curvatures show a nearly square-root dependence on u'/S_L , whereas the mean flamelet radius of curvature is approximately a factor of two larger than the Taylor scale of turbulence in the approach flow. The effect of Lewis number on flamelet curvature is evidenced by a 20% increase in mean curvatures which is attributed to the unstable flame fronts at Lewis number less than unity. The evolution of flamelet orientation with increasing u'/S_L shows a trend toward isotropy, which is estimated to prevail when u' becomes an order of magnitude larger than S_L . For unstable flame fronts ($Le < 1$), flamelets are more randomly orientated and thus isotropy may be achieved for somewhat smaller ratio of u'/S_L .

INTRODUCTION

Recently, analyses of turbulent premixed combustion within the wrinkled laminar flamelet regime have involved the use of various spatial statistical properties of flame fronts. These include fractal analysis (Gouldin, 1989) in which the fractal dimension and cutoff scales determine the ratio of turbulent to laminar burning surface areas; the strained laminar flamelet calculations of Cant and Bray (1988), where the mean reaction rate is related to spatial or temporal flamelet crossing frequency; the stochastic flamelet model (Pope and Cheng, 1988) in which the effects of curvature and orientation on the evolution of the flamelet area are modelled under idealized conditions; and the spectral method of Weller *et al.* (1990) where the spectral distribution of flame wrinkling is computed. Experimental evaluations of spatial flame properties to date are numerous and include, for example, the measurements of fractal dimensions (Mantzaras *et al.*, 1989; North and Santavicca, 1990; Wu *et al.*, 1991), inner cutoff scales (Shepherd *et al.*, 1990; North *et al.*, 1991), spatial and temporal flamelet crossing frequencies and flamelet orientation (Cheng *et al.*, 1988; Chew *et al.*, 1990). However, thus far, measurements of flamelet curvature have not been reported, except in one instance (zur Loye and Bracco, 1987); and perhaps for this reason curvature characteristics have not been extensively treated in modelling efforts.

Since the local laminar flame speed is determined by the Lewis number and flame stretch, to which both flow strain and curvature contribute, curvature and its statistics are an essential component in a rigorous treatment of wrinkled flamelet combustion. Experimental and theoretical investigations have shown that the combined effects of curvature with preferential diffusion and flow strain can greatly affect flame speeds and extinction limits (Mikolaitis, 1984a and 1984b; Asato *et al.*, 1988). In addition,

experimental work of Echekki and Mungal (1990) reveals that flame speed is non-linearly dependent upon flame curvature and can increase by a factor of up to 6.25 with respect to unstrained flame speed in the presence of large curvature. Therefore, it is of considerable interest to determine the range of flamelet curvature encountered under turbulence conditions characteristic of practical combustion devices, as flamelet curvature has potentially significant effects on turbulent combustion. On the other hand, some authors (Cant and Bray, 1988; Becker *et al.*, 1990) have argued that the overall effect of flamelet curvature on the burning rate integrates to zero if the curvature distribution is symmetric. Thus, an experimental investigation of flamelet curvature and its statistics at this point would prove to be useful.

Furthermore, there are some interesting questions concerning the orientation of the flamelets that need to be answered for accurate modelling as well as for fundamental understanding of the phenomena. For example, within the stochastic flamelet model (Pope and Cheng, 1988) the area-reduction term that determines the development of flamelet element area becomes infinite if flamelets are assumed to be randomly orientated, thus requiring a correction term called the orientation factor. At relatively low turbulence intensities, the flamelet crossing angle data by Chew *et al.* (1990) show a high degree of anisotropy in flamelet orientation indicated by the predominance of "forward-facing" flamelets. However, as the turbulence level increases, it is intuitively obvious that the flame front will become more convoluted resulting in a more randomly distribution of flamelet orientation angles. At sufficiently high turbulence intensities, the flamelet orientation is expected to be isotropic; and an assessment of the evolution of the flamelet orientation distribution toward isotropy is an issue that is addressed in this investigation.

Finally, as Pope *et al.* (1989) have considered the curvature of material surfaces in isotropic turbulence using direct numerical simulation, a parallel consideration of the curvature of a flame front, which is a nonuniformly propagating surface, is of interest. Such a comparison of curvature together with an examination of flamelet orientation distribution can provide insight into how propagation modifies the curvature of material surfaces and conversely how turbulence affects the geometry of flame fronts. In view of this, the aim of the present investigation is to experimentally determine the curvature and orientation statistics at various turbulence intensities and equivalence ratios, and examine the consequent implications on the interaction between turbulence and premixed flame fronts.

EXPERIMENTAL METHODS

Nearly one-dimensional, freely propagating, premixed turbulent flames were produced in an experimental device called a pulse flame flow reactor, which is schematically illustrated in Figure 1. Using this device, flames propagating downward into a high-intensity turbulence approach flow can be repetitively generated for ensemble-averaging of various flame properties. Details of the operation of this device are published elsewhere (Videto and Santavicca, 1991). In order to investigate various spatial properties of flame fronts, OH planar laser-induced fluorescence (PLIF) was used. The schematic of this setup is shown in Figure 2. The second harmonic of a Nd:YAG was used to pump a tunable pulsed dye laser, the output of which was frequency-doubled to generate a 284 nm uv-beam of *ca.* 10 ns in pulse duration. Following beam expansion to 20 mm diameter, a spherical-cylindrical lens combination was used to produce a beam sheet with a measured thickness of approximately 150 μm . The excitation-detection scheme involved excitation of the blended $Q_2(8)$ and

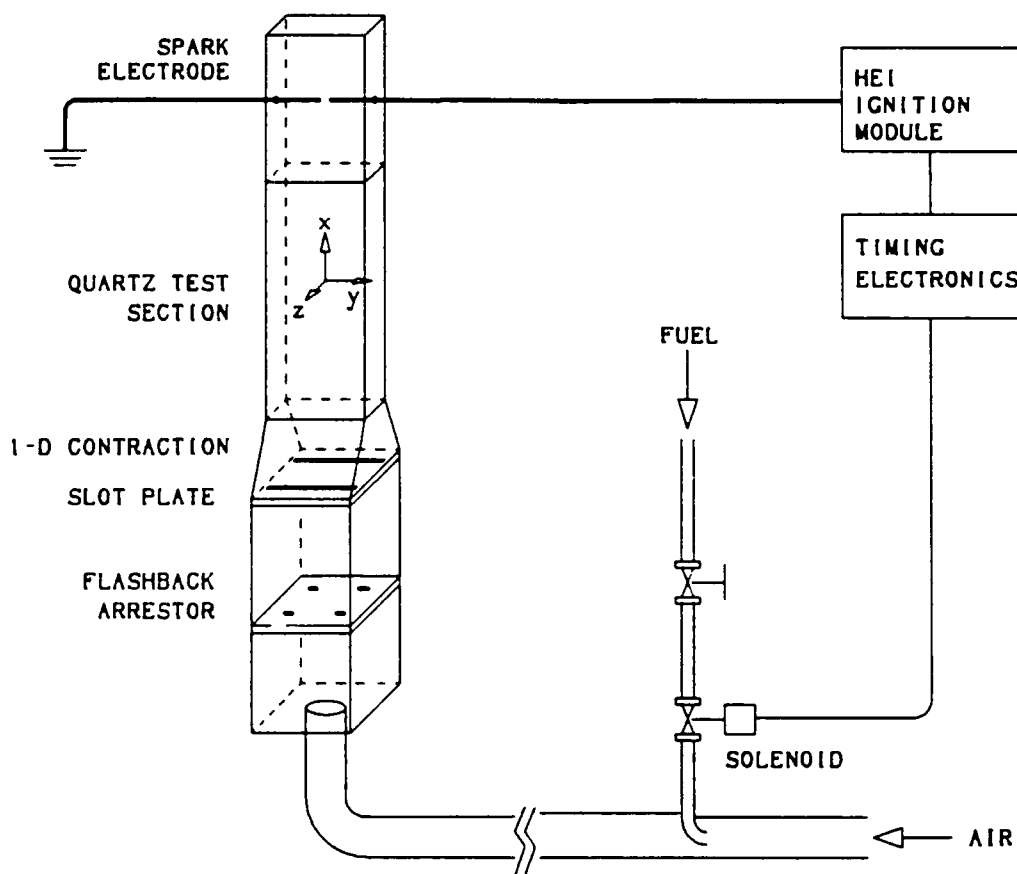


FIGURE 1 Pulsed-flame flow reactor.

$Q_1(9)$ lines in the $(1,0) A^2\Sigma^- - X^2\Pi$ transition, followed by broadband detection of the rovibrationally relaxed $(1,1)$ and $(0,0)$ fluorescence signal near 315 nm. 8 mm \times 8 mm images of the flame fronts were taken using a uv-transmitting camera lens (f/1.1) in conjunction with a dual microchannel-plate intensified Reticon camera. The image acquisition process was initiated by the trigger signal from an optical flame arrival detector indicating flame arrival within the field of view (North and Santavicca, 1990).

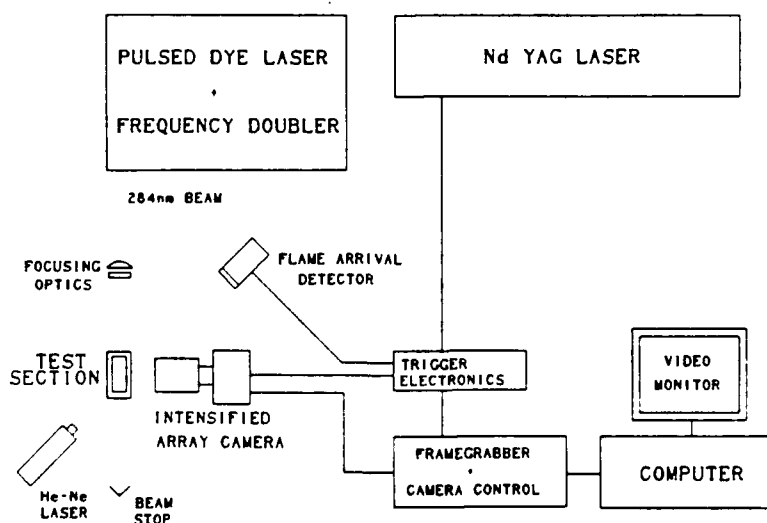


FIGURE 2 Schematic of OH PLIF imaging system.

TABLE I

Summary of test conditions

ϕ	u' (m/sec)	u'/S_L	Re_L	Da	Le	$\langle H \rangle$ (mm ⁻¹)	σ_H (mm ⁻¹)	a_1
0.75	0.5	1.42	154	56	1.86	0.017	0.664	0.75
0.75	1.0	2.85	314	29	1.86	-0.007	1.075	0.65
0.75	1.5	4.29	500	20	1.86	-0.017	1.117	0.65
0.75	2.0	5.71	667	15	1.86	0.112	1.677	0.65
1.00	0.6	1.42	185	67	1.40	0.001	0.804	0.75
1.25	0.5	1.42	154	56	0.98	0.025	0.827	0.75

This trigger signal caused the laser to pulse while simultaneously activating the gate on the intensified array camera. An intensifier gate of *ca.* 1 μ m was sufficient to eliminate the ambient noise due to flame luminescence.

Propane/air mixtures of equivalence ratios ranging from 0.75 to 1.25 were used. At a fixed equivalence ratio of 0.75, the turbulence intensity was varied from $u' = 0.5$ m/sec to 2.0 m/sec, corresponding to u'/S_L values from 1.42 to 5.71. Also, at a fixed u'/S_L of 1.42, the equivalence ratio was varied from 0.75 to 1.25, resulting in a Lewis number variation of 0.98 to 1.84. The test conditions are summarized in Table I.

CURVATURE ANALYSIS

From the OH PLIF images, a threshold pixel intensity was identified as the minimum value between bimodal intensity peaks corresponding to the burned and unburned gas regions in the intensity histogram. Using this threshold, the images were put into a binary format, from which the perimeters demarcating the burned/unburned regions were detected and digitized into numerical coordinates. A 4th-order Newton's divided difference formula, which is a 5-point curve-fitting scheme allowing for uneven interval lengths, was then applied to obtain a polynomial function for these perimeters. In a separate study (North *et al.*, 1991), fractal analysis was applied to the same OH PLIF images (included in the aforementioned article) in order to resolve inner cutoff scales, *i.e.*, the smallest scales of the flame fronts, yielding inner cutoffs ranging from 0.4 to 1 mm. Therefore, interval lengths in the difference formula were restricted to values between 0.25 and 0.625 mm. This is an important element in the present analysis in that interval lengths much smaller than the inner cutoff can result in false tracking of small-scale digitization noise in the perimeter while interval lengths larger than the inner cutoff can cause the perimeter tracing routine to miss relevant features in the flame front. Using 0.5 mm as the interval length for most of the perimeters, accurate tracing of the flame boundaries resulted with implicit filtering of extraneous noise smaller than the minimum scale present in the flame front. This method eliminates any ambiguities associated with analyzing perimeters containing noise, and is consistent with the concepts of fractal geometry in that using intervals of the order of the inner cutoff insures correct tracing of the perimeters.

As the difference formula cannot accept perimeters with infinite slopes, a threshold value in the vertical slope was set and detection of slopes higher than this threshold caused a 90° rotation in the coordinate system, resulting in high slopes being converted into nearly zero slopes. This method was also used to handle what would otherwise be intractable multi-valued perimeters. Another threshold in the horizontal slope was also set since the 90° rotation of the coordinate system can convert nearly zero slopes into unacceptably high slopes. Simultaneous detection of slopes exceeding both the

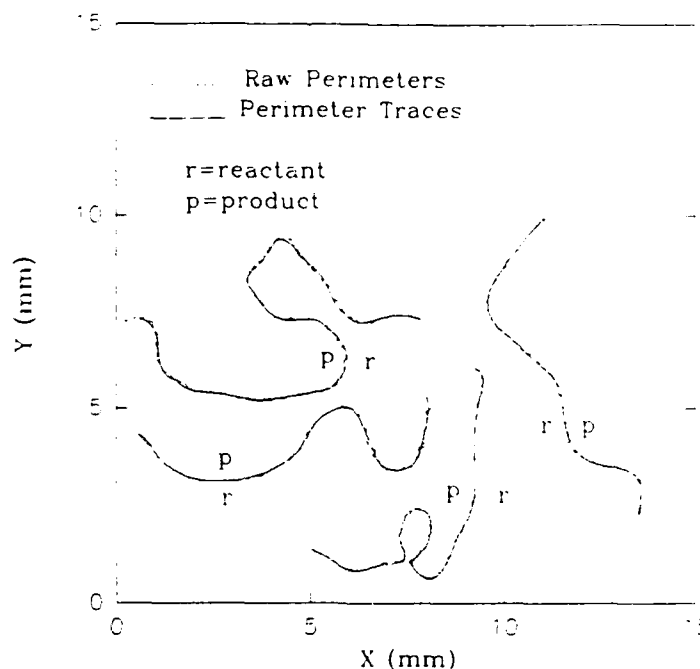


FIGURE 3 Typical performance of the perimeter tracing routine.

vertical and horizontal thresholds resulted in the rejection of that particular segment of the perimeter. Since the simultaneous occurrence of slopes exceeding both threshold limits is not directly dependent on curvature but on the coincidental orientation of two or more sections of the perimeter, this is not expected to introduce a bias in the subsequent analysis of curvature. In any event, the analysis provided better than a 90% acceptance rate; thus, bias associated with the thresholding in the perimeter tracing routine, if any, is expected to be minimal. After the polynomial function was obtained in this manner from the raw perimeter, the coordinate system was rotated back 90° to restore the original direction of flame propagation. As the accuracy of data obtained from these perimeters is critically dependent upon the accuracy of the perimeter traces, the entire set of ca., 250 perimeter traces was plotted and checked by directly comparing with the raw perimeters, as in Figure 3 where typical performance of the perimeter tracing routine is shown. Figure 3 is a sampling of flame perimeters obtained from four separate realizations; and the direction of propagation is globally from top to bottom as noted by the reactant and product sides of the flame perimeters. Local degradations of the raw perimeters can occur due to digitization noise, slight misfocussing and the effects of beam nonuniformity even after beam normalization. The importance of using the inner cutoff as the interval length is demonstrated in Figure 3, where it can be seen that selection of an interval length much smaller than the inner cutoff would cause the tracking of occasional small-scale noise and result in erroneously large curvature measurements.

Once the 4th-order polynomial functions of the perimeters were thus obtained and checked, the orientation and curvature of the flamelets represented on the perimeters could be analyzed in a straightforward manner since the first derivative of the polynomial gave the tangent from which the normal direction could easily be computed and the second derivative could be used to calculate the curvature. Curvature was defined positive for flamelets convex toward the reactants, while the orientation angle was measured with respect to the positive horizontal axis. 400 to 500 flamelet

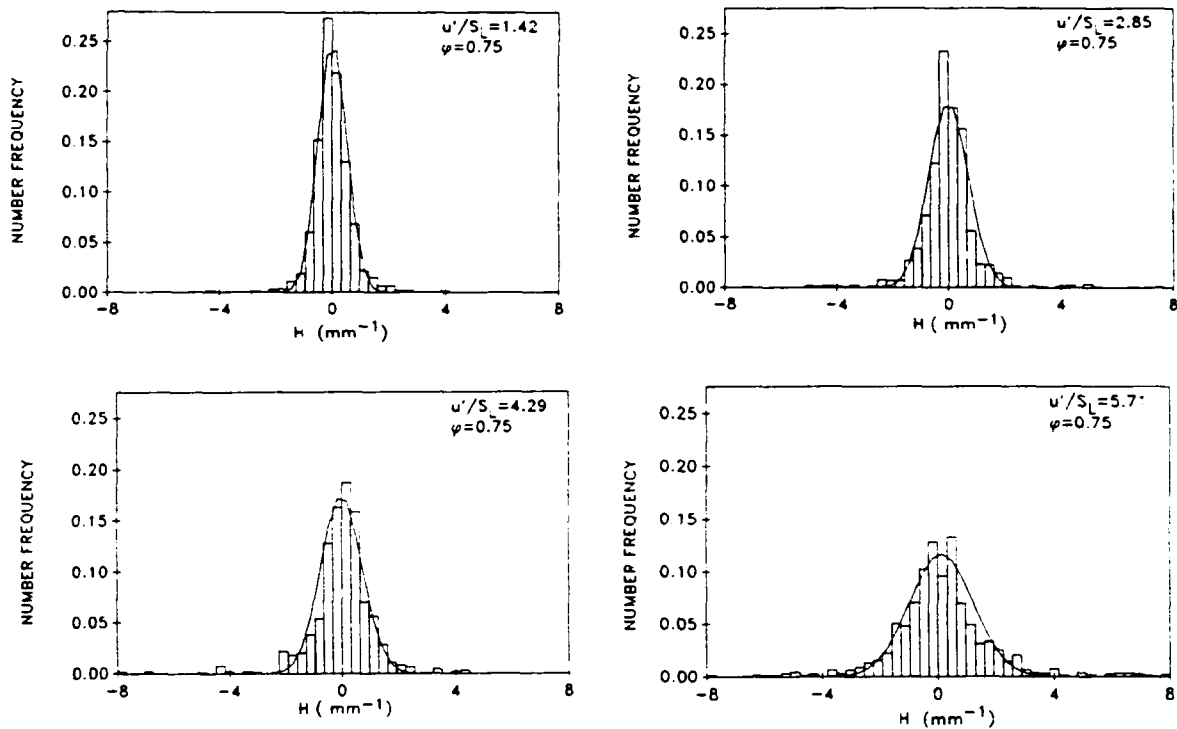


FIGURE 4 Evolution of flamelet curvature probability density functions for $u'/S_L = 1.42$ – 5.71 at $\phi = 0.75$.

elements of *ca.* 0.5 mm in length were analyzed for each condition, while the slight variations in flamelet element length were accounted for by statistical area-weighting.

RESULTS AND DISCUSSION

The evolution of the probability density function (pdf) of flamelet curvature with increasing u'/S_L at a fixed equivalence ratio of 0.75 is shown in Figure 4. Inspection of the pdf's and the flame perimeters indicate that the cusping of the flame front toward the product side which is observable in weakly turbulent flames is seldom observed at these conditions; and flamelets with large curvature are as likely to be convex as they are to be concave toward the product side. The pdf's exhibit a symmetric shape with respect to the zero mean, while the width (variance) increases, as expected, with increasing u'/S_L . At high u'/S_L , the ability of the flame to dampen the wrinkles caused by turbulence is reduced resulting in increased flamelet curvature. Moreover, with increasing u' or turbulence Reynolds number the relevant scales in the turbulent flow become smaller, again contributing to increased flamelet curvature. More will be said later on the scales of turbulence and their effects on flamelet curvature. The maximum statistically significant curvature, *i.e.*, maximum curvature with nonnegligible number frequency, ranges from 1.5 mm^{-1} at $u'/S_L = 1.42$ to 3 mm^{-1} at $u'/S_L = 5.71$. Comparing these results with flame speed measurements as a function of flame curvature reported by Echekki and Mungal (1990), flamelet curvature in this range is sufficient to cause more than a three-fold increase in local laminar flame speed with respect to the unstrained value. Flamelet curvature as high as 8 mm^{-1} is observed, translating to radius of curvature of 0.125 mm. Presence of radii of curvature smaller than the inner cutoff, however, does not contradict the inner cutoff results of the fractal analysis since isolated occurrences of high curvature does not lead to an increased surface length.

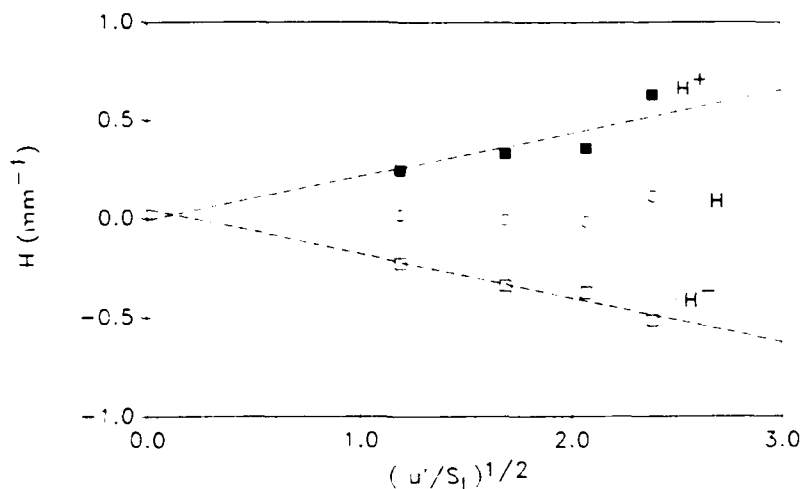


FIGURE 5 Mean flamelet curvatures as a function of $(u'/S_L)^{1/2}$ at $\phi = 0.75$.

The flamelet curvature pdf's can be approximated by Gaussian distributions as shown in Figure 4. The parameters used in the Gaussian distribution are the measured mean and variance of the flamelet curvature, where the variance is corrected by a factor close to 0.7 in order to account for the overestimation of the variance due to outlying data points. This correction is necessary for the Gaussian fit due to the non-zero probability of flamelets with high curvature while statistically significant curvatures are bounded by this Gaussian fit as shown in Figure 4. The correction factors, a_1 , are listed in Table I along with the means and variances.

From the measured pdf's of flamelet curvature, positive and negative components can be separately averaged to yield respective means. A logarithmic plot of these mean curvatures against u'/S_L yields slopes near 0.5. Thus anticipating a dependence of flamelet curvature proportional to $(u'/S_L)^{1/2}$, mean curvatures are plotted against the square root of u'/S_L as in Figure 5. Here, the flamelet curvatures plotted are unnormalized due to ambiguities in defining the flame thickness, which in any case is estimated to be $60 \mu\text{m}$ for these conditions. It can be observed in Figure 5 that there is an approximately linear increase (decrease) for positive (negative) components of flamelet curvature while the overall mean stays near zero. Least-square fit lines through the data points extrapolate toward zero curvature at u'/S_L goes to zero, which is reasonable since in the limit of zero turbulence intensity or infinite laminar flame speed the flame front is expected to be perfectly planar exhibiting no wrinkles in the absence of intrinsic instabilities. These observations indicate that the two-dimensional behaviour of flame front curvature is governed by a nearly square-root dependence on u'/S_L .

Next, we take the arithmetic mean of the absolute value of positive and negative flamelet curvatures at a given u'/S_L , and then compute the inverse of that quantity, to yield the mean radius of curvature which is plotted in Figure 6. The mean flamelet radii of curvature encountered range from 4.2 mm at $u'/S_L = 1.42$ to 1.8 mm at $u'/S_L = 5.71$. Mean flamelet radius of curvature of 1.6 mm has been reported for premixed-charge flames at $u'/S_L \approx 4.0$ in an IC engine by zur Loye and Bracco (1987), although the inner cutoff data being unavailable at the time the step size in the perimeter analysis of that study was varied as a parameter that sensitively affected the resultant measurements. Normalizing by the estimated flame thickness of $60 \mu\text{m}$ and again referring to Echekki and Mungal (1990), it is found that curvature effects alone can result in 10–30% change of flame speed in the mean from the unstrained laminar

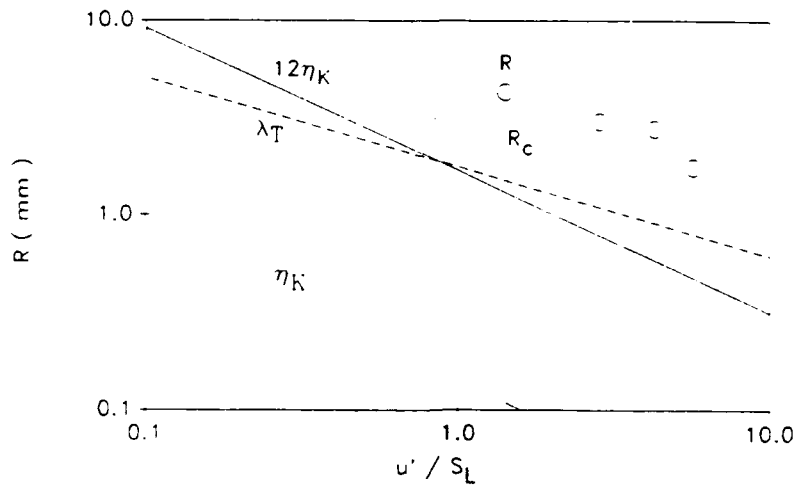


FIGURE 6 Mean flamelet radius of curvature as a function of u'/S_L at $\phi = 0.75$.

flame speed. Also plotted in this figure are the Taylor (λ_T) and Komogoroff (η_k) scales of turbulence in the approach flow, calculated through dimensional arguments (Hinze, 1975) using the measured turbulence intensity and integral scale, and also the Kolmogoroff scale multiplied by 12. This last quantity is of importance because through direct numerical simulation performed at a Taylor Reynolds number of 39 (Pope *et al.*, 1989), which is roughly comparable to $Re_\lambda = 48$ at $u'/S_L = 1.42$ in the present data, it has been found that the mean radius of curvature of material surfaces in isotropic turbulence is approximately 12 times the Kolmogoroff scale. Although this result is restricted to a single turbulence Reynolds number, some interesting observations can be made by comparing the mean flame radius of curvature with this scale as well as other relevant scales of turbulence. It is also of interest to note that in the numerical simulation by Pope *et al.* (1989) $12 \eta_k$ is found to roughly coincide with the Taylor scale of turbulence at this condition.

Before any direct comparison is made, the present data must be corrected for three-dimensional effects since $12 \eta_k$ is the radius of curvature of three-dimensional material surface defined as:

$$R_c = (H_1^2 + H_2^2)^{1/2},$$

where H_1 and H_2 are the principal components of curvature. Here, for flamelet curvature the orthogonal components is taken to be equal to the measured curvature, *i.e.*, $H_1 = H_2$, yielding $R_c = 1/\sqrt{2}R$. This correction is reasonable since the measured curvature is a random sampling of flamelet curvatures with no preferred direction. Recently, Ashurst (1991) used a zero-thickness, constant-density premixed flame model to show that the three-dimensional geometry of the flamelets are asymmetrical in that one curvature component is at least three times larger than the orthogonal component. However, random two-dimensional sampling of flamelet curvature in this geometry results in a correction factor of $1/\sqrt{2.5}$, which is a relatively small deviation from the present correction factor. Therefore, for the comparison discussed below the correction factor of $1/\sqrt{2}$ is retained. The comparison in Figure 6 shows that the corrected mean radius of curvature of the flame front, as expected, is larger than that of the material surface, represented by $12\eta_k$, while the slope of *ca.*, -0.55 is closer to that of λ_T (-0.46) than $12\eta_k$ (-0.74). Multiplying λ_T by two roughly gives the corrected flamelet radius of curvature, with agreement diminishing at higher u'/S_L . Thus, if material surfaces in isotropic turbulence can be assumed to possess a mean

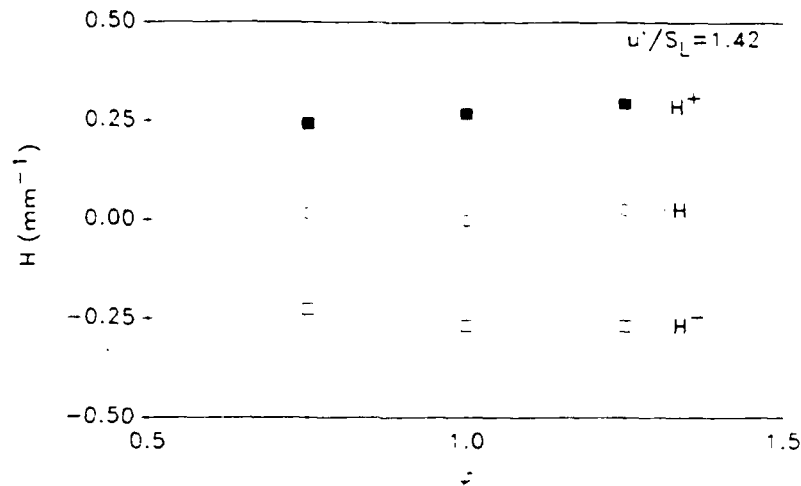


FIGURE 7 Mean flamelet curvatures as a function of equivalence ratio at $u'/S_L = 1.42$.

radius of curvature of the order of λ_T or $12\eta_k$ even at higher turbulence Reynolds numbers, then a possible mechanism for curvature generation in flame fronts is that turbulence by itself produces mean radius of curvature close to λ_T and the effect of flame propagation is to smoothe this surface and thereby increase the radius of curvature by a factor of up to 2, which possibly depends on the effects of Lewis number and flame stretch.

The effect of Lewis number on flamelet curvature is also investigated by fixing u'/S_L at 1.42 and varying the equivalence ratio from 0.75 to 1.25, corresponding to a variation between diffusively stable ($Le = 1.84$) and marginally unstable ($Le = 0.98$) conditions. The result is illustrated in Figure 7. For the stoichiometric case, u' was increased in order to keep u'/S_L constant, while for equivalence ratios of 0.75 and 1.25 the laminar flame speeds are identical and adjustment of u' was not necessary. Here, again curvature is plotted without normalizing by flame thickness since this would imply that flamelet curvature scales with flame thickness whereas we have seen in Figure 6 that flamelet curvature is more likely to scale with the length scale of turbulence in the approach flow. The increase in flamelet curvature resulting from unstable flame fronts is reflected by an almost 20% increase in the absolute values of positive and negative mean curvatures and a similar increase in the variance.

It is worth mentioning that the mean flamelet radius of curvature of 3.6 mm at $\phi = 1.25$ is comparable to the integral scale of flame wrinkling measured by Chew *et al.* (1990), which was found to be nearly constant at ca., 4 mm for similar u'/S_L and equivalence ratio; although in that study a Bunsen flame has been used and turbulence characteristics are somewhat different. Flamelet radius of curvature has been used as a representative length scale in theoretical studies (Matalon and Matkowsky, 1982), and is a natural scale defining the characteristics of flame front wrinkling. Also, since curvature directly contributes to the modification of the local laminar flame speed due to stretch effects, the distribution of flamelet radius of curvature, along with the orientation statistics to be presented next and fractal data such as the fractal dimension and cutoff scales, can provide a complete spatial characterization of turbulent premixed flame fronts.

The orientation of the flamelet, α , is defined in the present analysis as the angle that the normal vector of the flamelet element makes with respect to the positive horizontal axis, yielding -90° as the direction of downward propagation. Figure 8 shows the

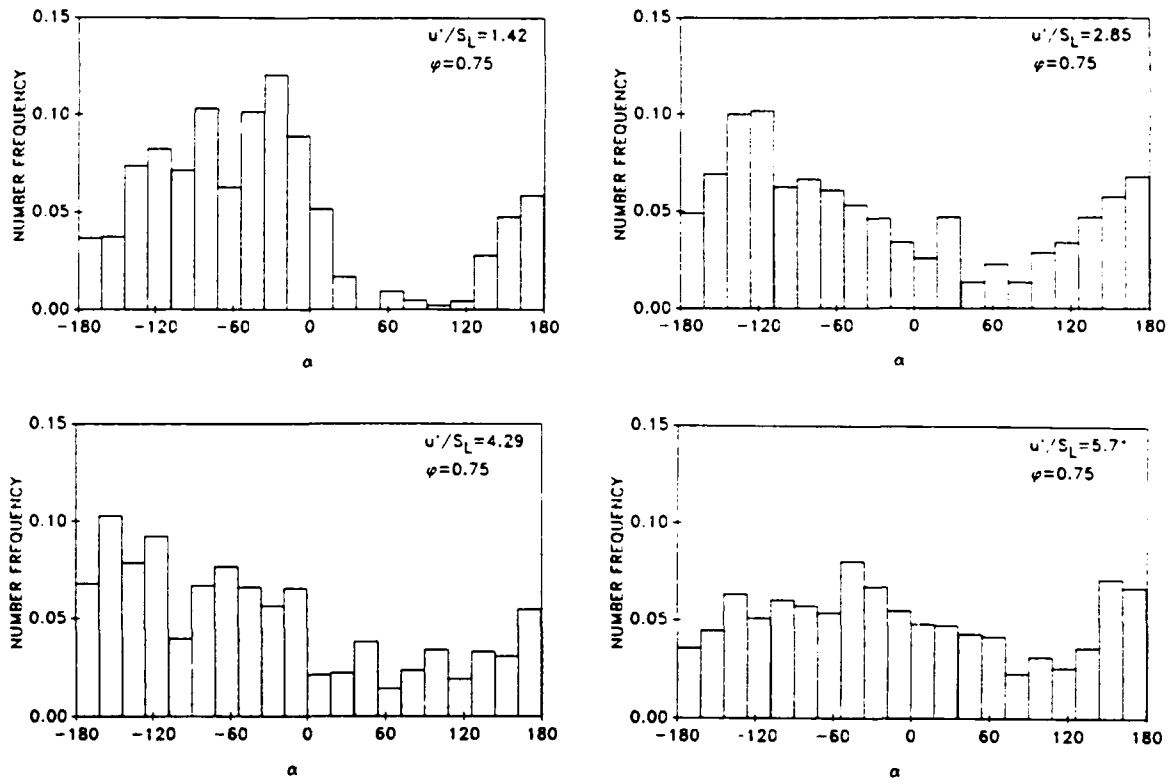


FIGURE 8 Evolution of flamelet orientation distributions for $u'/S_L = 1.42$ – 5.71 at $\phi = 0.75$.

evolution of the flamelet orientation distribution with increasing u'/S_L at an equivalence ratio of 0.75. The distribution at $u'/S_L = 1.42$ is qualitatively very similar to the distribution of flamelet crossing angle measured by Chew *et al.* (1990) as most of the flamelets propagate in the forward direction with orientation angle between -180° and 0° while “reversed” flamelets, *i.e.*, propagating upward with orientation angle between 0° and 180° , are less frequent in occurrence. Although in the present analysis the orientation angle is simply the normal direction of flamelets whereas the flamelet crossing angle data of Chew *et al.* (1990) are measured with respect to surfaces of constant mean reaction progress variable, it is reasonable to expect that the distribution of these quantities will behave in a similar manner since the surface of constant reaction progress variable in the present experiment, where flames propagate freely downward, is likely to be nearly horizontal. With increasing u'/S_L , the orientation becomes more uniformly distributed, *i.e.*, from mostly forward facing orientations at $u'/S_L = 1.42$ the flamelets tend toward isotropy at $u'/S_L = 5.71$ where all directions of propagations are observed in significant number frequencies. However, complete uniformity in the orientation distribution is not achieved even at $u'/S_L = 5.71$, indicating that the flamelets at this condition are not yet completely isotropic.

A measure of the anisotropy of flamelet orientation is the variance in the number frequency of orientation angle with respect to the mean number frequency normalized by the mean number frequency, denoted $\sigma_f/\langle f \rangle$. For a uniform distribution, the variance of number frequency is zero since the number frequencies are all identical, thus $\sigma_f/\langle f \rangle$ equals zero. An estimate of the isotropy condition can be made by plotting $\sigma_f/\langle f \rangle$ against u'/S_L and extrapolating to find u'/S_L where $\sigma_f/\langle f \rangle$ goes to zero as shown in Figure 9; here for consistency $\sigma_f/\langle f \rangle$ is plotted against the square-root of u'/S_L . A least-square fit line through the data points show that in order for $\sigma_f/\langle f \rangle$ to be zero $(u'/S_L)^{1/2} \approx 3.3$ or $u'/S_L \approx 10$. Therefore, u' must be approxi-

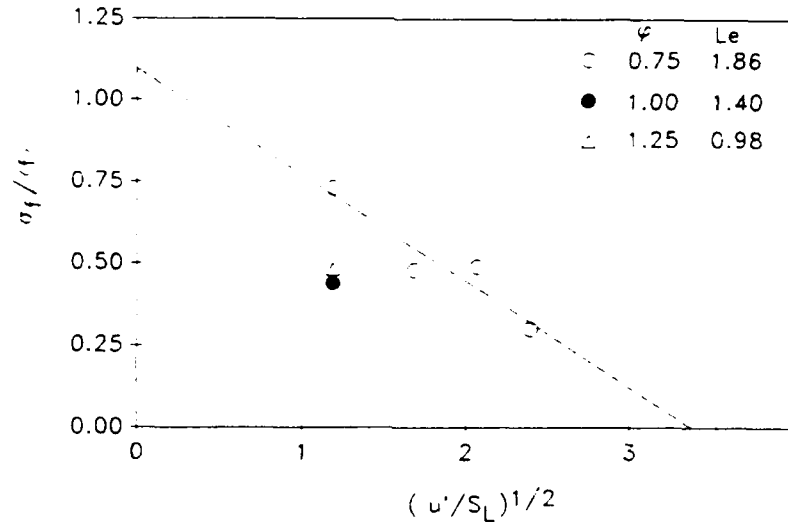


FIGURE 9 Estimate of isotropy condition.

mately an order of magnitude larger than S_L for isotropy to be achieved. Inspection of OH PLIF images show that multiply-connected flamelets, *i.e.*, packets of burned and unburned gases occur at negligible frequency at $u'/S_L = 1.42$, while this frequency increases with increasing u'/S_L . Although three-dimensional topology of flame fronts cannot accurately be assessed using a single-sheet two-dimensional methods (Mantzaras *et al.*, 1988) such as used in this study, shadowgraph measurements by Abdel-Gayed *et al.* (1989) demonstrates the possible mechanisms of flame front fragmentation and pocket formations. Therefore, for $u' \gg S_L$ it may be hypothesized that the flame front can no longer be singly-connected resulting in so-called "packet" combustion and within this regime since flame fronts form many separate and locally closed surfaces the flamelet orientation is likely to be isotropic. Strictly, however, the present results apply only to the two-dimensional behavior of the flame fronts. If the flame front is thermodynamically unstable, $\sigma_f/\langle f \rangle$ becomes smaller as shown in Figure 9 where two additional data points corresponding to equivalence ratios of 1.00 and 1.25 are included, indicating that the flamelets are more randomly orientated and that isotropy may be achieved for slightly smaller u'/S_L .

CONCLUSIONS

From the considerations above, the following conclusions are made concerning the curvature and orientation statistics of turbulent premixed flame fronts:

- (1) The flamelet curvature distributions are symmetric with respect to the zero mean and can be approximated by Gaussian distributions.
- (2) The mean positive (negative) flamelet curvature increases (decreases) with increasing u'/S_L , and is governed by a nearly square-root dependence on u'/S_L .
- (3) The mean flamelet radius of curvature is larger than but of the order of Taylor scale of turbulence in the approach flow.
- (4) The mean flamelet curvature increases when the flame front becomes diffusively unstable ($Le < 1$).
- (5) Isotropy in flamelet orientation is estimated to occur for u' nearly an order of magnitude larger than S_L , whereas the required ratio is expected to be somewhat smaller for unstable flame fronts.

ACKNOWLEDGEMENTS

The support for this work has been provided by the Air Force Office of Scientific Research under Grant AFOSR-87-0097, Dr. Julian Tishkoff contract manager.

REFERENCES

- Abdel-Gayed, R. G., Bradley, D., and Lung, F. K.-K. (1989). Combustion Regimes and the Straining of Turbulent Premixed Flames. *Comb. Flame* **76**, 213.
- Asato, K., Kawamura, T., and Ban, T. (1988). Effects of Curvature on Extinction of Premixed Flames Stabilized in Stagnation Flow. *Twenty-Second Symposium (International) on Combustion*, p. 1509.
- Ashurst, Wm. T. (1991). Geometry of Premixed Flames in Three-Dimensional Turbulence, presented at the Western States Section/The Combustion Institute 1991 Spring Meeting, Boulder, Colorado.
- Becker, H., Monkhouse, P. B., Wolfrum, J., Cant, R. S., Bray, K. N. C., Maly, R., Pfister, W., Stahl, G., and Warnatz, J. (1990). Investigation of Extinction in Unsteady Flames in Turbulent Combustion by 2D-LIF OH Radicals and Flamelet Analysis. *Twenty-Third Symposium (International) on Combustion*, Combustion Institute, p. 817.
- Cant, R. S. and Bray, K. N. C. (1988). Strained Laminar Flamelet Calculations of Premixed Turbulent Combustion in a Closed Vessel. *Twenty-Second Symposium (International) on Combustion*, Combustion Institute, p. 791.
- Cheng, R. K., Shepherd, I. G., and Talbot, L. (1988). Reaction Rates in Premixed Turbulent Flames and Their Relevance to the Turbulent Burning Speed. *Twenty-Second Symposium (International) on Combustion*, Combustion Institute, p. 771.
- Chew, T. C., Dray, K. N. C., and Britter, R. E. (1990). Spatially Resolved Flamelet Statistics for Reaction Rate Modelling. *Comb. Flame* **80**, 65.
- Echekki, T. and Mungal, M. G. (1990). Flame Speed Measurements at the Tip of a Slot Burner: Effects of Flame Curvature and Hydrodynamic Stretch. *Twenty-Third Symposium (International) on Combustion*, Combustion Institute, p. 455.
- Gouldin, F. C. (1987). An Application of Fractals to Modeling Premixed Turbulent Flames. *Comb. Flame* **68**, 249.
- Hinze, J. O. (1975). *Turbulence*, McGraw-Hill, 2nd Edition, p. 225.
- Mantzaras, J., Felton, P. G., and Bracco, F. V. (1988). Three-Dimensional Visualization of Premixed-Charge Engine Flames: Islands of Reactants and Products; Fractal Dimensions; and Homogeneity. SAE Paper No. 881635.
- Mantzaras, J., Felton, P. G., and Bracco, F. V. (1989). Fractals and Turbulent Premixed Engine Flames. *Comb. Flame* **77**, 295.
- Matalon, M. and Matkowsky, B. J. (1982). Flames as Gasdynamic Discontinuities. *J. Fluid Mech.* **124**, 239.
- Mikolaitis, D. W. (1984a). The Interaction of Flame Curvature and Stretch, Part 1: The Concave Premixed Flame. *Comb. Flame* **57**, 25.
- Mikolaitis, D. W. (1984b). The Interaction of Flame Curvature and Stretch, Part 2: The Convex Premixed Flame. *Comb. Flame* **58**, 23.
- North, G. L. and Santavicca, D. A. (1990). The Fractal Nature of Premixed Turbulent Flames. *Comb. Sci. and Tech* **72**, 215.
- North, G. L., Lee, T.-W., and Santavicca, D. A. (1991). Fractal Analysis of Small-Scale Structures in Premixed Turbulent Flames. *Comb. Sci. and Tech.*, submitted.
- Pope, S. B. and Cheng, W. K. (1988). The Stochastic Flamelet Model of Turbulent Premixed Combustion. *Twenty-Second Symposium (International) on Combustion*, Combustion Institute, p. 781.
- Pope, S. B., Yeung, P. K., and Girimaji, S. S. (1989). The Curvature of Material Surface in Isotropic Turbulence. *Physics of Fluids A*, **1**, 2010.
- Shepherd, I. G., Cheng, R. K., and Goix, P. J. (1990). The Spatial Structure of Premixed Turbulent Stagnation Point Flames. *Twenty-Third Symposium (International) on Combustion*, Combustion Institute, p. 781.
- Videto, B. D. and Santavicca, D. A. (1991). A Turbulent Flow System for Studying Turbulent Combustion Processes. *Comb. Sci. and Tech.*, in press.
- Weller, H. G., Morooney, C. J., and Gosman, A. D. (1990). A New Spectral Method for the Time-Varying Area of a Laminar Flame in Homogeneous Turbulence. *Twenty-Third Symposium (International) on Combustion*, Combustion Institute, p. 629.
- Wu, M. S., Kwon, S., Driscoll, J. F., and Faeth, G. M. (1991). Preferential Diffusion Effects on the Surface Structure of Turbulent Premixed Hydrogen/Air Flames. *Comb. Sci. and Tech.*, to appear.
- zur Loye, A. O. and Bracco, F. V. (1987). Two-Dimensional Visualization of Premixed-Charge Flame Structure in an IC Engine. SAE Paper No. 870454.

APPENDIX B**SURFACE PROPERTIES OF TURBULENT PREMIXED PROPANE/AIR FLAMES AT
VARIOUS LEWIS NUMBERS**

T.-W. Lee, G.L. North and D.A. Santavicca
Turbulent Combustion Laboratory
Department of Mechanical Engineering
Propulsion Engineering Research Center
Penn State University

ABSTRACT- Surface properties of turbulent premixed flames including the wrinkled flame perimeter, fraction of the flame pocket perimeter, flame curvature and orientation distributions have been measured for propane/air flames at Lewis numbers ranging from 0.98 to 1.86 and $u'/S_L = 1.42$ -5.71. The wrinkled flame perimeter is found to be greater for the thermodynamically unstable Lewis number ($Le < 1$) by up to 30% in comparison to the most stable condition ($Le = 1.86$) tested, while the fraction of the flame pocket perimeter shows a similar tendency to be greater for $Le < 1$. The flame curvature probability density functions are nearly symmetric with respect to the zero mean at all Lewis numbers throughout the range of u'/S_L tested, and show a much stronger dependence on u'/S_L than on the Lewis number. Similarly, the flame orientation distributions show a trend from anisotropy toward a more uniform distribution with increasing u'/S_L at a similar rate for all Lewis numbers. Thus, for turbulent premixed propane/air flames for a practical range of Lewis number from 0.98 to 1.86, the effect of Lewis number is primarily to affect the flame structures and thereby flame surface areas and flame pocket areas, while the flame curvature and orientation statistics are essentially determined by the turbulence properties.

INTRODUCTION

Within the laminar flamelet regime of turbulent premixed combustion, the turbulent burning velocity as a first approximation can be set equal to the ratio of the wrinkled flame area to the undisturbed laminar flame area. In spite of this simplification, a rigorous method of estimating the turbulent burning velocity as a function of the turbulence and mixture properties remains elusive. For this reason, recent modelling and experimental research efforts have focused on the surface properties of turbulent premixed flames. One modelling approach to predict the turbulent flame surface area is based on the fractal analysis [1] where the fractal dimension and cutoff scales as a function of turbulence intensity provide a quantitative description of convoluted turbulent flame surface areas. Experimental measurements in support of the fractal analysis include those of Mantzaras et al. [2], Shepherd et al. [3], North and Santavicca [4], Wu et al. [5], North et al. [6] and references cited therein. Other approaches to estimate the flame surface area include the works of Cant et al. [7] and Weller et al. [8]; while experimentally investigators have considered surface properties such as the flame surface areas measured directly using laser tomography [5,9], spatial and temporal flamelet crossing frequency [3,10,11] and flame curvature [9,12] and orientation [3,12]. Recently, direct numerical simulations of turbulent premixed flames under simplifying assumptions of either two-dimensional turbulence or zero heat release [13-15] have also been important in extending the knowledge of the surface properties of turbulent premixed flames.

Insofar as the flame surface properties are concerned in the laminar flamelet regime, flame surface area, flame curvature and orientation statistics provide a complete set of geometrical descriptions of turbulent premixed flame surfaces [16], although additional topological information such as the fraction of the flame pocket area would be required for corrugated flamelets, i.e. flames involving multiply-connected flamelets. The flame surface area is important as an indicator of the degree of flame front wrinkling, as well as being a measure of the turbulent burning velocity. The flame curvature probability density function (pdf) indicates how the flame wrinkle scales are

distributed, while the flame orientation data shows the distribution of flame normal vectors in space. Furthermore, since flame curvature contributes to flame stretch, considerations of flame stretch effects on turbulent premixed flames require a knowledge of the flame curvature distributions. Many flamelet models of turbulent premixed combustion [17,18] have considered only the effect of tangential flow strains on the flame, while neglecting the contribution of flame curvature to flame stretch. Recent computational results of Haworth and Poinso [14] have indicated that the local flame properties at non-unity Lewis numbers correlate more strongly with flame curvature than with the tangential strain rates, thus further necessitating the knowledge of flame curvature distributions at various turbulence conditions and Lewis numbers. The flame orientation is also important as a fundamental flame surface property as well as having potential applications in several modelling approaches, in which the flame crossing angle is required for the computation of the local mean reaction rate [19] and modelling of source terms in the governing equation for the flame surface-to-volume ratio [7].

In addition to turbulence properties, the Lewis number is an important independent variable in determining the surface properties of turbulent premixed flames. Not only the local flame properties at a given flame stretch vary at different Lewis numbers, but also the flame surface undergoes significant changes depending on whether the thermodiffusive instabilities amplify or suppress the wrinkles caused by turbulence. For example, larger flame areas have been observed for $Le < 1$ in turbulent premixed flames [5,9,14], while the Lewis number enters into consideration in order to rationalize the observed variations in turbulent burning velocities when different fuel/air mixtures are tested [20]. Another important aspect of turbulent premixed combustion is the propensity of the flames to form pockets under certain conditions, since this contributes to an increase in flame area as well as having an effect on pollutant formation processes [21,22]. In view of this, the aim of the present investigation is to characterize the flame surface properties in terms of the flame surface area or wrinkled flame perimeter observable in two-dimensional images, fraction

of flame pocket perimeters, flame curvature and orientation distributions for turbulent premixed propane/air flames at various turbulence conditions and Lewis numbers.

EXPERIMENTAL METHODS

Premixed flames propagating freely toward a nearly isotropic turbulent flow field were generated in a device called a pulsed-flame flow reactor, schematically shown in Fig. 1. A slug of propane/air mixture is produced upstream by introducing the fuel into the air flow for a selected interval via a solenoid valve controlling the fuel flow. Intense turbulence was generated as the mixture went through the slot plate and one-dimension contraction section. Once ignited by the spark electrodes above the test section, a turbulent flame propagated downward into the test section until it reached the end of the propane/air mixture. This process of generating the fuel/air mixture slug and igniting the mixture could be repeated in approximately 1/4 Hz cycles in order to obtain ensemble averages of flame properties over many realizations. The turbulence properties were quantified by measuring the intensity and the integral length scales in the longitudinal and transverse directions, which were nearly identical verifying the isotropy of the turbulent flow field within the test section. Using this device, turbulence intensity, u' , ranging from 0.4 to 2.0 m/s for mean flow velocities of 1.2 to 4.8 m/s could be obtained with corresponding turbulence Reynolds number, Re_L , of 150 to 670. Further details of the experimental apparatus and turbulence measurements which shows that the turbulence properties are well-characterized and reasonably uniform within the test section can be found in Videto and Santavicca [23]. For a given turbulence condition, three different equivalence ratios, ϕ , were used in order to assess the effects of Lewis number on flame surface properties. Equivalence ratios of 0.75, 1.0 and 1.25 for propane/air mixtures corresponded to Lewis numbers of 0.98, 1.40, and 1.98, respectively. Complete test conditions are tabulated in Table 1. The laminar flame speed, S_L , was identical at $\phi = 0.75$ and 1.25, while it is higher at stoichiometry. Thus, in order to isolate the Lewis number effects from the effects of u'/S_L , the turbulence intensity for

$\phi=1.0$ was raised by an amount necessary to keep u'/S_L constant at all equivalence ratios. However, since the turbulence intensity was already near the maximum capability of the pulsed-flame flow reactor at $u'/S_L = 5.71$, only $\phi = 0.75$ and 1.25 mixtures were tested at $u'/S_L = 5.71$.

Two-dimensional images of the turbulent flames were obtained using OH planar laser-induced fluorescence (PLIF). As is well known, OH radicals exist in large quantities within the preheat zone and in the burned gas regions, and provide a convenient marker for flame fronts. A Nd:YAG laser-pumped tunable dye laser was used to produce a laser beam of ca. 10 ns pulse duration tuned to an excitation wavelength of OH radicals. A cylindrical-spherical lens combination was used to obtain a beam sheet with a measured minimum thickness of approximately 150 μm . The resultant fluorescence signal was collected by a UV-transmitting camera lens and focused onto an intensified array camera. Further details of the OH PLIF setup can be found in Lee et al. [9]. In order to capture the propagating flame within the camera field of view, the image acquisition process was synchronized to a trigger signal from an optical flame arrival detector which indicated the presence of a flame within the field of view when a He-Ne laser beam was deflected off a photodiode by the density gradients at the flame tip. The trigger signal caused the laser to pulse, while activating the image acquisition hardware. An intensifier gate of ca. 1 μs was used to eliminate the noise due to flame luminescence. For each condition, typically ten 20 mm x 20 mm images were taken which have pixel and feature resolutions of 150 μm and 300 μm , respectively; and comparison with 8 mm x 8 mm images (pixel and feature resolutions of 60 μm and 125 μm , respectively) showed that the flame curvature and orientation statistics were nearly identical between the two fields of views, while there is less bias for the measurements of the total and pocket flame perimeters when larger field of view of 20 mm x 20 mm is used. Thus, the results presented in this study represents those obtained from 20 mm x 20 mm images, while the 8 mm x 8mm images provided via fractal analysis the required interval length used in the curvature analysis.

For the OH PLIF images thus obtained, a threshold pixel intensity selected from the intensity

histogram was used as a cutoff to differentiate burned and unburned regions during the binarization of the images. The intensity histograms typically yielded nearly bimodal distributions as most of the pixels were located in burned or unburned regions while a small percentage of the pixels in the preheat zone exhibited pixel intensities between these two peak intensities. The use of the threshold intensity as the average of these two peak intensities resulted in well-characterized flame boundaries due to the small thickness of the preheat zone and nearly parallel nature of the OH LIF iso-intensity lines within the preheat zone. From the binarized images, the flame perimeters were detected and their Cartesian coordinates stored for analyses. A 4th-order Newton's divided difference formula, which is a 5-point curve-fitting scheme, was then applied to obtain the flame coordinates as smoothed functions of a variable, s , which is the distance along the flame front from a fixed origin on the flame front. The curvature, H , then can be obtained in a straight-forward manner using: $H = [(d^2x/ds^2)^2 + (d^2y/ds^2)^2]^{1/2}$. Use of the independent variable, s , provides an improvement over the previous analytical method [12] since the flame curvature and orientation can be analyzed regardless of the slope and complexity of the flame contours. The flame curvature is defined positive if the flame element is convex toward the reactant. The orientation angle, α , which denotes the angle that the flame normal vector makes with the positive horizontal axis, can also be computed from the flame coordinates. The interval length used in the curve-fitting scheme was kept within 0.5 to 0.9 mm range, which corresponded to the inner cutoff scales obtained for these flames from fractal analysis [6], i.e., the smallest scales of flame front wrinkles. The fractal analysis [6] has shown that the inner cutoff is of the order of the flame thickness and invariant with respect to the changes in turbulence conditions; therefore interval length of the order of the flame thickness can be used in similar analyses of flame curvature and perimeters. The choice of the inner cutoff scale as the interval length in the curvature analysis is important for both flame curvature and flame perimeter measurements since by sampling of the digitized flame coordinates at too close intervals can result in tracking of small-scale digitization noise leading to excessively large curvatures; and conversely, use

of large interval lengths can cause the curve-fitting scheme to miss relevant features in the flame fronts. The wrinkled flame perimeter was also measured using this interval length by adding all the intervals traced on the flame perimeter. With the interval length within 0.5 to 0.9 mm, the number of flame elements analyzed per condition ranged from 400 to 750, with the number being larger for higher u'/S_L due to the larger wrinkled flame perimeter observed per image. With the number of samples analyzed, the mean flame curvature, for example, is accurate within $\pm 10\text{-}15\%$ with 95% confidence. Both flame curvature and orientation statistics were weighted by the length of each analyzed flame element.

RESULTS AND DISCUSSION

Typical binarized images of the turbulent flames at $u'/S_L = 1.42 - 5.71$ are shown in Figs. 2-4 for Lewis numbers of 1.86, 1.40 and 0.98, respectively (equivalence ratios of 0.75, 1.0 and 1.25). With increasing u'/S_L at all Lewis numbers, smaller scales of flame front wrinkles are observed which contribute to the increase in flame surface area. In addition, large scale "folding" of the flame sheets (e.g. Figs. 2(a)-(d)) similarly can increase the flame area; i.e., the flame structure in Fig. 2(a) is that of a curved flame front with small-scale fluctuations, while with increasing u'/S_L the large scale undulations such as a "peninsula" at $u'/S_L = 2.85$ and several layers of folded flame sheets at $u'/S_L = 4.29$ and 5.71 become more prominent in Figs. 2(b)-(d). Formation of flame pockets is another contributor to the flame area. Although pockets of reactants and products are observable at relatively low u'/S_L , they become increasingly frequent in occurrence at high u'/S_L and for thermodynamically unstable mixture, e.g., Figs. 4(c) and (d). While the variations in the flame structures with increasing u'/S_L are substantial for $Le=1.86$, more dramatic changes in the flame structures can be observed for the thermodynamically unstable flame fronts ($Le<1$) in Figs. 4(a)-(d). For example, the flame front tends to be very strongly convoluted along with the presence of flame

pockets (e.g. Figs. 4(c) and (d)). Comparisons with the flame front images at $Le=1.86$ at identical u'/S_L 's show that the flame fronts are in general more convoluted and exhibit larger wrinkled flame areas with flame pockets being observed in higher frequency. These observations of the flame structures indicate that the higher degree of flame front distortions at higher u'/S_L and at thermodynamically unstable condition results in larger flame surface areas and greater frequency of flame pockets, as will be quantified subsequently. Moreover, at all the Lewis numbers the curvature of the flame front wrinkles increases with increasing u'/S_L which is noticeable even in cursory visual examinations. However, at a fixed u'/S_L the changes in flame curvature at different Lewis numbers does not appear to be pronounced. Another important observation from these flame front images is the relative lack of cusps at any Lewis number under consideration, which has an important impact on the flame curvature distributions. As for the flame orientation, the increase in u'/S_L leads to changes in the flame structures such as the appearance of small-scale wrinkles, large-scale folding of the flame sheets, and flame pockets, which can contribute to the increasing randomness in the flame orientation distributions. However, the large-scale folding of flame sheets in Fig. 2(d) and fragmented flame fronts with flame pockets in Figs. 4(c) and (d) can contribute in equal degrees to the changes in length-weighted flame orientation statistics, and the effect of the Lewis number on the flame orientation distribution may be relatively minor in spite of the differences in the appearance of the flame fronts at different Lewis numbers. In the subsequent quantitative analyses of these flame front images, first the flame curvature and orientation statistics will be presented, to be followed by the wrinkled flame perimeters and the fraction of the flame pocket perimeters.

Flame curvature pdf's at various u'/S_L and Lewis numbers are shown in Fig. 5. Similar to earlier results at a single equivalence ratio of 0.75 ($Le=1.86$) [12], the flame curvature pdf's are nearly symmetric with respect to the zero mean at all Lewis numbers under consideration, while the width of the pdf's increases with u'/S_L in a nearly identical manner for all Lewis numbers. The number frequency at zero flame curvature decreases by a factor of two for a four-fold increase in

u'/S_L , also indicating that the flame curvatures are distributed at larger curvatures for higher u'/S_L . Although a very weak bias toward positive flame curvature is observed at some conditions, the degree of departure from symmetry is within the experimental uncertainties and no firm conclusions can be drawn from it. The maximum curvatures range from approximately 2.0 mm^{-1} at $u'/S_L = 1.42$ to 4.5 mm^{-1} at $u'/S_L = 5.71$, which converts to radii of curvature of 0.2 to 0.5 mm that are roughly in the order of the laminar flame thickness. The symmetry of the flame curvature pdf's along with the flame front image of Figs. 2-4 indicate that throughout the range of Lewis numbers covered in the present study the cusping of the flame fronts associated with weakly turbulent and/or thermodiffusively unstable flames are seldom observed. Cusped flame fronts typically involve a large area of positively curved (convex toward the reactant) flame front terminated by a cusp, so that the corresponding curvature pdf's contain a strong bias toward positive curvature while the cusp manifests itself as a large negative curvature with small frequency of occurrence due to the negligible flame area that it occupies. The mechanism of cusp formation in weakly turbulent flames is that once the flame front is wrinkled by the velocity fluctuations normal flame propagation causes the positively-curved (convex toward the reactant) flame elements to grow in area while the negatively-curved flame elements move toward and eventually collide with one another, thus resulting in a cusp. Thus, for cusps to occur, the velocity fluctuations in the turbulent flow field needs to be weak and spatially sparse so that the flame front wrinkles have time to develop their features. For turbulent flow fields where the strength and spatial distribution of the vortices are such that the flame front is continuously wrinkled by the vortices and not allowed to fully develop its features through normal flame propagation, the flame curvature pdf's exhibit nearly symmetric shape, as shown in Fig. 5. Another important observation is the insensitivity of the flame curvature pdf's for the Lewis number variation from 0.98 to 1.86. This is in apparent contrast to the observed changes in flame structures when the mixture becomes thermodiffusively unstable in Figs. 4(a)-(d). A possible explanation for the insensitivity of the curvature pdf's to Lewis number variations is that if the amplitude of the flame front wrinkles alone

is increased due to the thermodiffusive instabilities then both large curvatures at the "crest" and "trough" of the wrinkles and small curvatures in between are generated with equal contributions to the length-weighted flame curvature pdf's. That is, the flame structures and flame area can be affected by thermodiffusive instabilities due to the increase in the amplitudes of the wrinkles, with length-weighted flame curvature statistics subject to relatively minor changes. Thus, Fig. 5 shows that flame curvatures are strongly dependent on u'/S_L and relatively insensitive to the variations in the Lewis number for u'/S_L from 1.42 to 5.71. In a stagnation flame configuration, Goix and Shepherd [9] have also observed that at low u'/S_L of 1.2 the flame curvature pdf's are symmetric with respect to the zero mean and insensitive to the changes in the Lewis number even though there is a substantial increase in the flame surface area. Recent computational results similarly indicate that the flame curvature pdf's for constant-density [13] and two-dimensional turbulent flames [14] are nearly symmetric with respect to the zero mean; the maximum flame curvature does not exceed the inverse of the flame thickness; and the flame curvature pdf's are relatively insensitive to the variations in Lewis number ($Le=0.8-1.2$) [14].

From the flame curvature pdf's, the positive, negative and overall mean flame curvatures, $\langle H^+ \rangle$, $\langle H^- \rangle$ and $\langle H \rangle$ respectively, can be computed. The positive and negative mean curvatures, when plotted against $(u'/S_L)^{1/2}$ in Fig. 6, show a nearly linear dependence and tend toward zero curvature when u'/S_L is extrapolated to zero, indicating that the mean curvatures scale reasonably well with $(u'/S_L)^{1/2}$ for all Lewis numbers under consideration. This square-root dependence is interesting in view of the fact that the length scale of flame curvature, defined as $\langle R \rangle = 2/(\langle H^+ \rangle + |\langle H^- \rangle|)$, is for all the test conditions as shown in Table 1 approximately twice the Taylor scale of turbulence in the approach flow, which has a square-root dependence on the turbulence Reynolds number. Since the measured integral length scale varies by a small amount from 4.9 to 5.2 mm, the Taylor scale in the present experiment has a nearly square-root dependence on u' . Thus, a possible explanation for the square-root dependence of mean flame curvatures on u'/S_L

is that an appropriate length scale of turbulence, the Taylor scale in this case, determines the mean flame curvatures. For material surface in isotropic turbulence, the mean curvature has been found to be close to 12 times the Kolmogoroff scale which equals the Taylor scale for the turbulence flow field investigated by Pope et al. [24]. A related study of flame/vortex interactions [25] has shown that the mean flame curvature of a premixed flame front wrinkled by an array of vortices has been found to be of the order of the vortex diameter, while the vortex rotational velocity normalized by the laminar flame speed, comparable to u'/S_L in this study, certainly acts to increase the flame area but has relatively minor effect on the characteristic flame curvature. Thus, above results indicate that the length scale of turbulence has significant influence on the mean flame curvatures of turbulent premixed flames. Various length scales of turbulence for the present test conditions along with the overall mean, $\langle H \rangle$, and variance in flame curvature are included in Table 1.

The distributions of flame orientation angles, α , are plotted in Fig. 7 for various equivalence ratios. As noted earlier, the flame orientation angle is measured with respect to the positive horizontal axis, and thus the downward direction of normal flame propagation is assigned the value of -90° . It can be observed in Fig. 7 that for low $u'/S_L = 1.42$ and 2.85 , the flame orientation is predominantly in the downward direction ($-180^\circ < \alpha < 0^\circ$) due to the fact that wrinkling of the flame front is not sufficiently strong to cause extensive local reversal in the flame propagation consistent with the observations in the flame front images of Figs. 2-4. Similar observations of flame orientation distributions centered around the normal direction of flame propagation have been observed for premixed Bunsen burner flames [10] at low turbulence levels ($u'/S_L \approx 1.9$). At higher u'/S_L , the appearance of the small-scale wrinkles, large-scale folding of the flame fronts and increased frequency of pocket formations cause the flame elements to be oriented randomly in space and contribute to the flame orientation distributions tending toward isotropic distributions. In spite of the differences in the flame structures at different Lewis numbers as observed in Figs. 2-4, no consistent trend is observed in Fig. 7 concerning any dependence of the flame orientation on the

Lewis number due to the fact that small-scale wrinkles, large-scale folding of flame sheets and the presence of flame pockets can contribute in equal degrees to randomizing the flame orientation distributions.

As Fig. 7 shows, the flame orientation distribution evolves from a highly anisotropic one toward a more uniform distribution with increasing u'/S_L . A measure of the degree of isotropy in the flame orientation is the variance of the number of frequencies with respect to the mean number frequency in the flame orientation distributions [12] in Fig. 7. That is, for a perfectly isotropic flame front the variance in the number frequency about the mean number frequency will be zero since the distribution is perfectly uniform at all angles, while for a highly anisotropic flame front the variance will be large. The variance in the number frequency in the flame orientation distribution normalized by the mean number frequency, $\sigma_f/\langle f \rangle$, at various Lewis numbers is plotted as a function of u'/S_L in Fig. 8. In spite of scatter in these data at low u'/S_L , Fig. 8 shows a trend toward isotropy, i.e., $\sigma_f/\langle f \rangle$ approaching zero with increasing u'/S_L , while the effect of the Lewis number is difficult to discern due to the scatter in the data. An extrapolation of the data in Fig. 8 indicates that the isotropy in the flame orientation is achieved for $u'/S_L \approx 10$, similar to earlier results from this laboratory [12].

The wrinkled flame perimeter normalized by a reference laminar flame perimeter, P_T/P_L , are plotted in Fig. 9 as a function of u'/S_L at various Lewis numbers. The reference laminar flame perimeter is defined as the distance between the maximum and minimum horizontal coordinates of the flame front in a given image. Typically, since the field of view in the image is filled with the flame front, this reference flame perimeter is equal to the width of the field of view. P_T/P_L is not only an indicator of the degree of flame front wrinkling, but also a measure of the turbulent burning velocity if the local flame speed does not differ appreciably from the unstrained laminar flame speed. P_T/P_L in Fig. 9 ranges from 2.9 to 5.2 when u'/S_L is varied from 1.42 and 5.71, and these values are well within the range of observed turbulent burning velocities as compiled by Abdel-Gayed et al. [20],

although the rate of increase in P_T/P_L as a function of u'/S_L is somewhat lower than the observed slope of the compiled data [20] possibly due to the fact that P_T/P_L is a two-dimensional wrinkled flame perimeter data and owing to the differences in the detailed turbulence properties such as the length scales, the spatial intermittency of velocity fluctuations, and burner configurations. As noted earlier, increase in the frequency of small-scale wrinkles, large-scale folding of flame sheets, and formation of pockets contribute to the increase in flame surface areas with increasing u'/S_L . This effect appears to be accelerated for the thermodynamically unstable mixtures ($Le=0.98$) as indicated by the higher flame perimeters in Fig. 9 at nearly all u'/S_L in comparison with mixtures with larger Lewis numbers. Amplification of flame front wrinkles and an increase in the propensity to form flame pockets at the unstable condition thus leads to changes in flame structures, as observed in flame front images of Figs. 2-4, and higher wrinkled flame perimeters by up to 30% as shown in Fig. 9. Similar increases in flame surface areas for thermodynamically unstable flames has been observed by Wu et al. [5] for hydrogen/air premixed flames; by Haworth and Poinot [14] for premixed flames in two-dimensional turbulence; and by Goix and Shephard [9] for stagnation flames. Thus, for turbulent premixed flames for u'/S_L from 1.42 to 5.71 at the range of Lewis number considered in this study, the effect of the Lewis number is primarily to affect the flame structures and enhance the flame surface areas while the flame curvature and orientation statistics are essentially determined by the turbulence properties.

The tendency of the turbulent flames to form pockets can also be quantified by measuring the ratio of the flame pocket perimeter and the total wrinkled flame perimeter, which is plotted in Fig. 10. Formation of a reactant pocket is a purely kinematical phenomenon in which fluid dynamic straining and normal flame propagation cause different flame elements to collide with one another thus forming a closed surface enveloping the reactant, and is easily observed in turbulent premixed flames [5] and in flame/vortex interactions [21,22]. Formation of a product pocket, however, involves local quenching or "tearing" of the flame front for the pocket to be separated from the contiguous

flame front; and two-dimensional images are insufficient to conclude that observed product pockets are truly separate pockets of product gases in three-dimensions [26]. However, experimental evidence using shadowgraph photography exists in support of the formation of product pockets in sufficiently strong turbulence [27]; and in any event, we adopt a two-dimensional definition of product pockets since they contribute to an apparent increase in two-dimensional flame surface areas. Within this definition, the entire perimeter of the flame pockets should be observable within the field of view for the objects to be classified as flame pockets. It can be observed in Fig. 10 that for a given u'/S_L the flame pocket perimeter tends to be larger for $Le=0.98$ ($\phi = 1.25$), although at stoichiometry the flame pocket perimeter exhibits relatively small values. The instability mechanism can enhance pocket formations since the increase in the amplitudes of the flame front wrinkles increases the probability that the different flame elements will be contacted thus forming a pocket of reactant; furthermore local quenching of the flame can cause separations from the contiguous flame front to form pockets of products. The flame pocket perimeter ranges from 5-25% of the total wrinkled flame perimeter; thus for strong turbulence and/or thermodiffusively unstable mixtures, formation of pockets can be an important contributor to the increase of turbulent burning velocities, and constitutes an important feature of turbulent premixed flames at these conditions.

CONCLUSIONS

From these results, the following conclusions concerning the surface properties of turbulent premixed propane/air flames are made:

1. Two-dimensional images of turbulent premixed propane/air flames have been obtained for $u'/S_L=1.42-5.71$ and $Le=0.98-1.86$, which show that the flame fronts are more strongly convoluted with increasing u'/S_L and for thermodiffusively unstable mixtures ($Le<1$). Flame structures at these conditions include such features as small-scale wrinkles, large-scale folding of flame sheets and flame

pockets.

2. The flame curvature probability density functions are found to be nearly symmetric with respect to the zero mean for all the Lewis numbers and turbulence conditions tested; and the mean flame radii of curvature are approximately twice the Taylor scale of turbulence in the approach flow, suggesting that the length scale of turbulence has a more important role than u'/S_L or Lewis number in determining the flame curvature.
3. The flame orientation exhibits an evolution from anisotropy toward a more uniform distribution with increasing u'/S_L at a similar rate for all Lewis numbers tested, and isotropy is estimated to occur for $u'/S_L \approx 10$.
4. The normalized wrinkled flame perimeter, P_T/P_L , is observed to vary from 2.9 to 5.2 when u'/S_L is increased from 1.42 to 5.71, while thermodynamically unstable mixture ($Le < 1$) exhibits larger wrinkled flame perimeter by up to 30 % in comparison to flames with $Le > 1$.
5. Pockets of both reactants and product gases in two-dimensional images are observed at these conditions accounting for up to 25% of the total wrinkled flame perimeters with the fraction of the flame pocket perimeters tending to be larger for $Le < 1$.

ACKNOWLEDGEMENTS

The support for this research has been provided by the Air Force Office of Scientific Research under Grant AFOSR-87-0097, with Dr. Julian Tishkoff as program manager.

REFERENCES

1. Gouldin, F. C., Combust. Flame 68:249-266 (1987).
2. Mantzaras, J., Felton, P. G. and Bracco, F. V., Combust. Flame 77:295-310 (1989).
3. Shepherd, I. G., Cheng, R. K. and Goix, P. J., Twenty-Third Symposium (International) on Combustion, The Combustion Institute, Pittsburgh, 1990, p. 781.

4. North, G. L. and Santavicca, D. A., Combust. Sci. Tech. 72:215-232 (1990).
5. Wu, M.-S., Kwon, S., Driscoll, J. F. and Faeth, G. M., Combust. Sci. Tech. 73:327-350 (1990).
6. North, G. L., Lee, T.-W. and Santavicca, D. A., Combust. Sci. Tech., submitted.
7. Cant, R. S., Pope, S. B. and Bray, K. N. C., Twenty-Third Symposium (International) on Combustion, The Combustion Institute, Pittsburgh, 1990, p. 809.
8. Weller, H. G., Marooney, C. J. and Gosman, A. D., Twenty-Third Symposium (International) on Combustion, The Combustion Institute, Pittsburgh, 1990, p. 629.
9. Goix, P. J. and Shepherd, I. G., Combust. Sci. Tech., to appear.
10. Chew, T. C., Bray, K. N. C. and Britter, R. E., Combust. Flame 80:65-82 (1990).
11. Cheng, R. K., Shepherd, I. G. and Talbot, L., Twenty-Second Symposium (International) on Combustion, The Combustion Institute, Pittsburgh, 1988, p. 771.
12. Lee, T.-W., North, G. L. and Santavicca, D. A., Combust. Sci. Tech. 84:121-132 (1992).
13. El-Tahry, S. H., Rutland, C. and Ferziger, J., Combust. Flame 83:155-173 (1991).
14. Haworth, D. C. and Poinso, T. J., Combust. Sci. Tech., in press.
15. Kwon, S., Wu, M.-S., Driscoll, J. F. and Faeth, G. M., Combust. Flame 88:221-238 (1992).
16. Pope, S. B., Int. J. Engng. Sci. 26:445-469 (1988).
17. Abdel-Gayed, R. G., Bradley, D. and Lau, A.K.C., Twenty-Second Symposium (International) on Combustion, The Combustion Institute, Pittsburgh, 1988, p. 731.
18. Cant, R. and Bray, K. N. C., Twenty-Second Symposium (International) on Combustion, The Combustion Institute, Pittsburgh, 1988, p. 791.
19. Bray, K. N. C., Champion, M. and Libby, P. A., Twenty-Second Symposium (International) on Combustion, The Combustion Institute, Pittsburgh, 1988, p. 763.
20. Abdel-Gayed, R. G., Bradley, D. and Lawes, M., Proc. R. Soc. Lond. A 414:389-413 (1987).
21. Poinso, T., Veynante, D. and Candel, S., J. Fluid Mech. 228:561-606 (1991).
22. Roberts, W. L., Driscoll, J. F., Drake, M. C. and Ratcliffe, J. W., Twenty-Fourth Symposium

(International) on Combustion, in press.

23. Videto, B. D. and Santavicca, D. A., Combust. Sci. Tech. 76:159-164 (1991).
24. Pope, S. B., Yeung, P. K. and Girimaji, S. S., Physics of Fluids A 1:2010-2018 (1989).
25. Lee, T.-W. and Santavicca, D. A., Combust. Sci. Tech., in press.
26. Mantzaras, J., Felton, P. G. and Bracco, F. V., SAE Paper No. 881635, 1988.
27. Abdel-Gayed, R. G. and Bradley, D. and Lung, F.K.-K., Combust. Flame 76:213-218 (1989).

Table 1. Summary of test conditions.

ϕ	U^a (m/s)	u' (m/s)	u'/S_L	δ_L^b (mm)	Le	Re_L	L^c (mm)	λ_T^d (mm)	$\langle R \rangle^e$ (mm)	σ_H^f (mm ⁻¹)
0.75	1.2	0.5	1.42	0.7	1.86	154	4.8	1.5	3.0	0.93
0.75	2.4	1.0	2.85	0.7	1.86	314	4.9	1.1	2.7	0.99
0.75	3.6	1.5	4.29	0.7	1.86	500	5.2	0.9	2.3	1.22
0.75	4.8	2.0	5.71	0.7	1.86	667	5.2	0.8	1.5	1.92
1.00	1.4	0.6	1.42	0.6	1.40	185	4.8	1.4	3.1	0.88
1.00	2.9	1.2	2.85	0.6	1.40	377	4.9	1.0	2.7	0.99
1.00	4.3	1.8	4.29	0.6	1.40	600	5.2	0.8	2.1	1.35
1.25	1.2	0.5	1.42	0.7	0.98	154	4.8	1.5	3.1	0.95
1.25	2.4	1.0	2.85	0.7	0.98	314	4.9	1.1	2.3	1.24
1.25	3.6	1.5	4.29	0.7	0.98	500	5.2	0.9	1.9	1.51
1.25	4.8	2.0	5.71	0.7	0.98	667	5.2	0.8	1.8	1.54

^aMean flow velocity; ^bflame thickness ($\delta_L = 4.6\alpha/S_L$ where α is the mean thermal diffusivity); ^cintegral length scale; ^dTaylor length scale ($\lambda_T = L(15/Re_L)^{1/2}$); ^emean flame radius of curvature ($\langle R \rangle = 2/(\langle H^+ \rangle + \langle H^- \rangle)$); ^fvariance in flame curvature.

Figure Captions

Fig. 1. Pulsed-flame flow reactor.

Figs. 2(a)-(d). Binarized flame front images at $\phi=0.75$ ($Le=1.86$) for $u'/S_L=1.42-5.71$ (20 mm x 20 mm field of view; black represents the reactant and the direction of global flame propagation is from top to bottom).

Figs. 3(a)-(c). Binarized flame front images at $\phi=1.00$ ($Le=1.40$) for $u'/S_L=1.42-4.29$.

Figs. 4(a)-(d). Binarized flame front images at $\phi=1.25$ ($Le=0.98$) for $u'/S_L=1.42-5.71$.

Fig. 5. Flame curvature probability density functions.

Fig. 6. Mean flame curvatures.

Fig. 7. Flame orientation distributions.

Fig. 8. Variance in number frequency of the flame orientation angles normalized by the mean number frequency.

Fig. 9. Normalized wrinkled flame perimeter as a function of u'/S_L for $Le=0.98-1.86$.

Fig. 10. Ratio of the flame pocket perimeter to the total wrinkled flame perimeter.

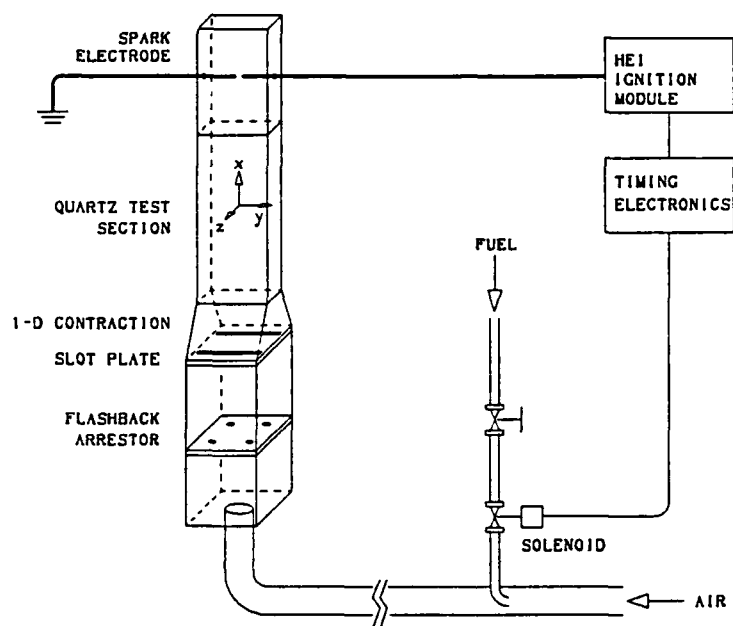
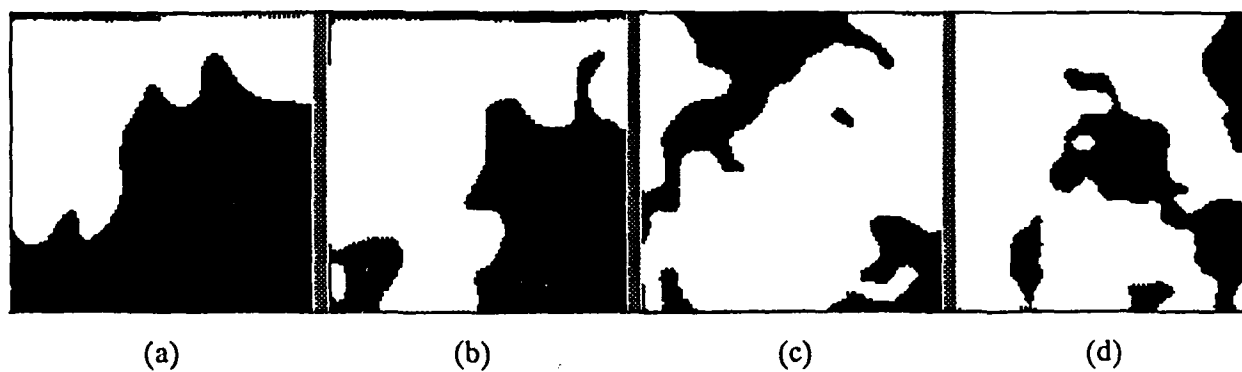
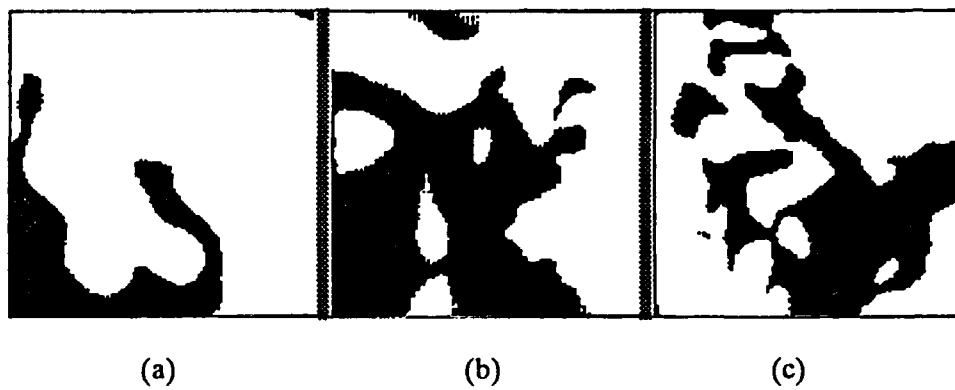


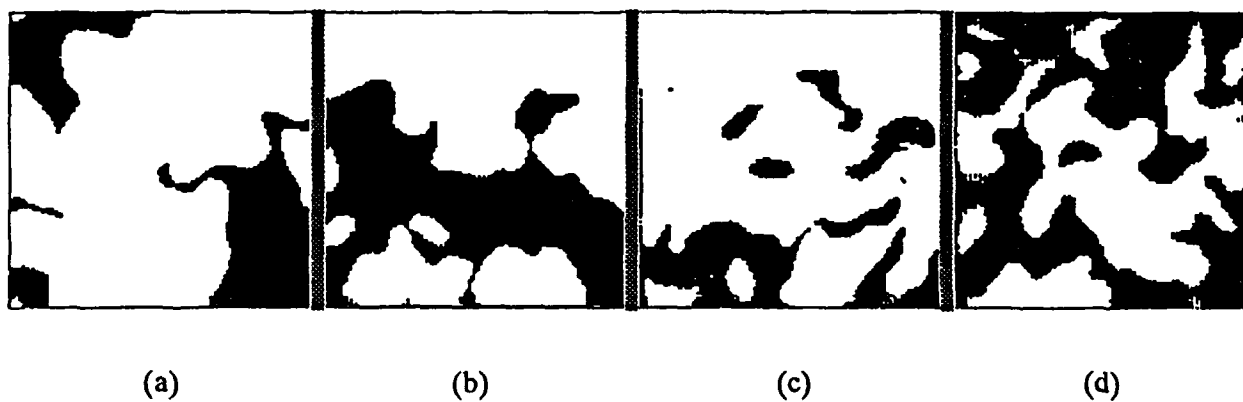
Fig. 1. Pulsed-flame flow reactor.



Figs. 2 (a)-(d). Binarized flame front images at $\phi=0.75$ ($Le=1.86$) for $u'/S_L=1.42-5.71$ (20 mm x 20 mm field of view; black represents the reactant and the direction of global flame propagation is from top to bottom).



Figures 3 (a)-(c). Binarized flame front images at $\phi=1.00$ ($Le=1.40$) for $u'/S_L=1.42-4.29$.



Figures 4 (a)-(d). Binarized flame front images at $\phi=1.25$ ($Le=0.98$) for $u'/S_L=1.42-5.71$.

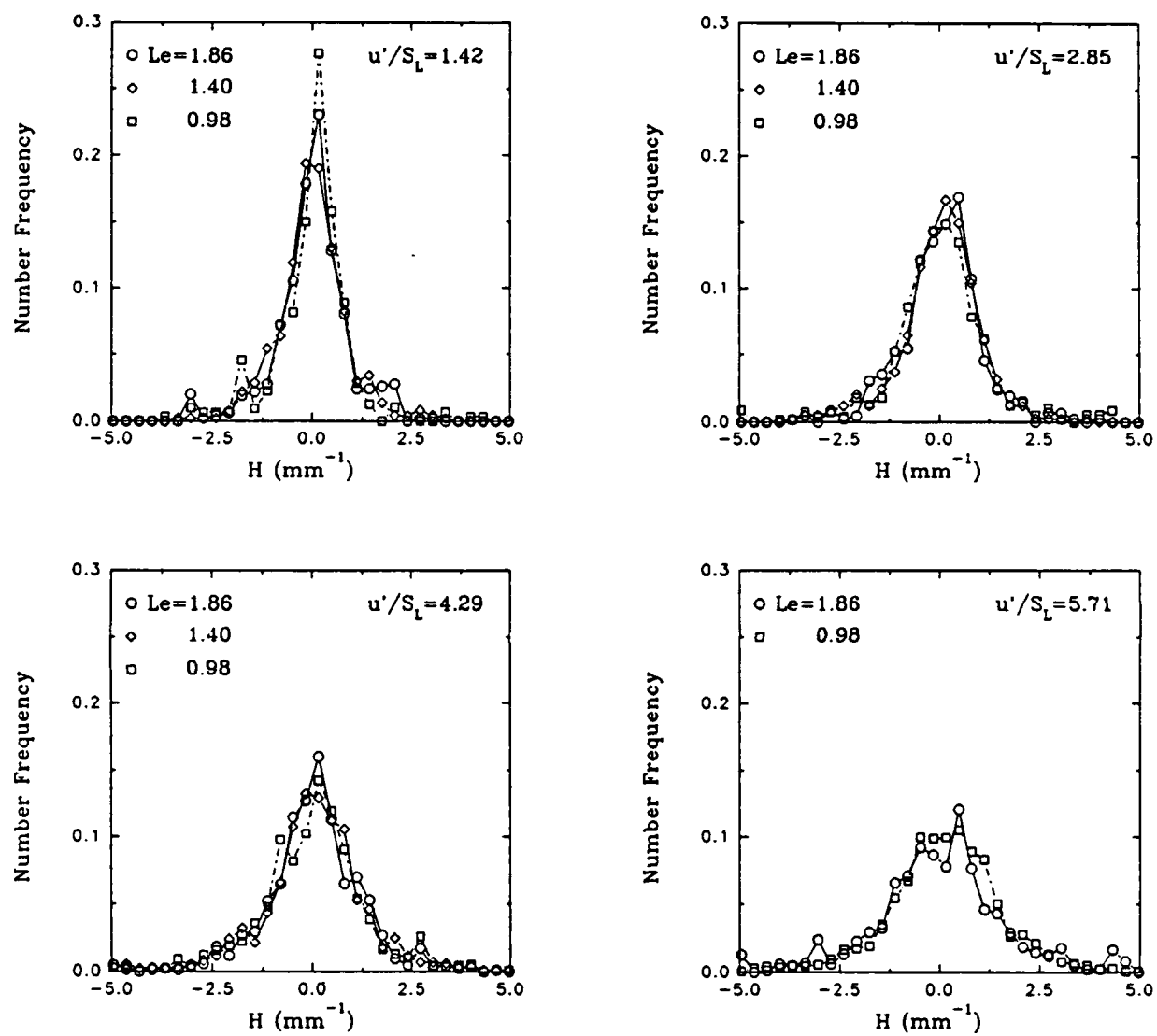


Fig. 5. Flame curvature probability density functions.

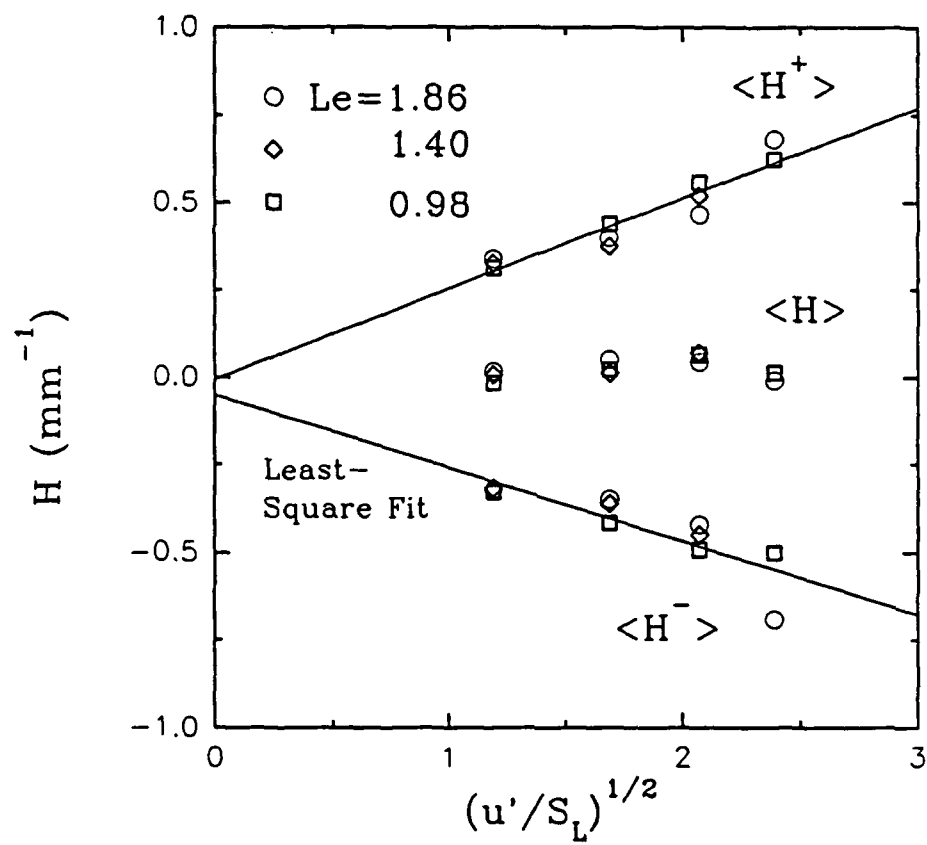


Fig. 6. Mean flame curvatures.

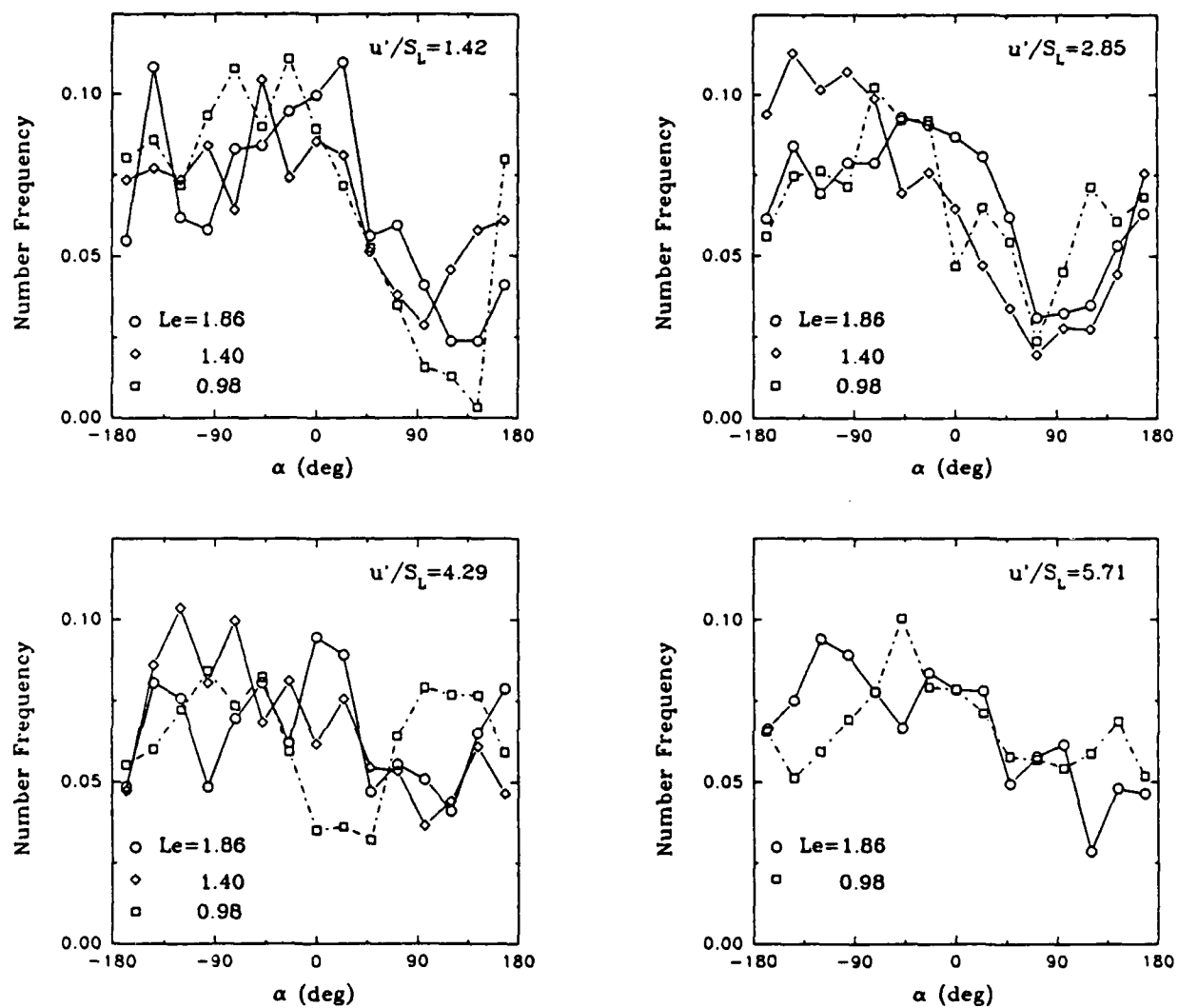


Fig. 7. Flame orientation distributions.

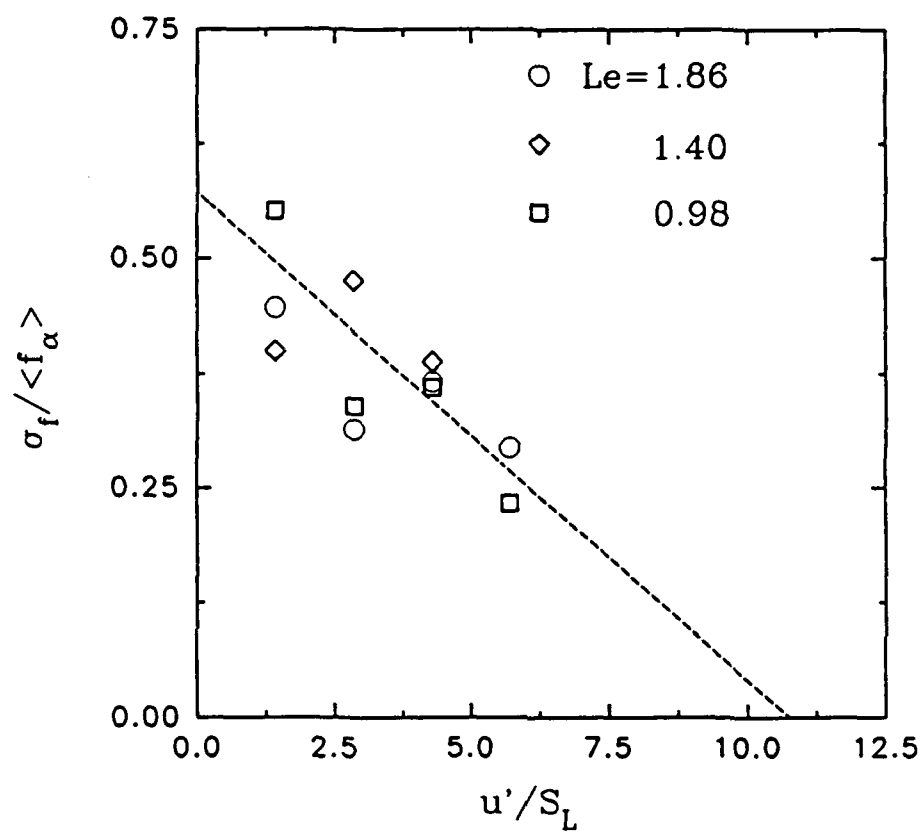


Fig. 8. Variance in number frequency of the flame orientation angles normalized by the mean number frequency.

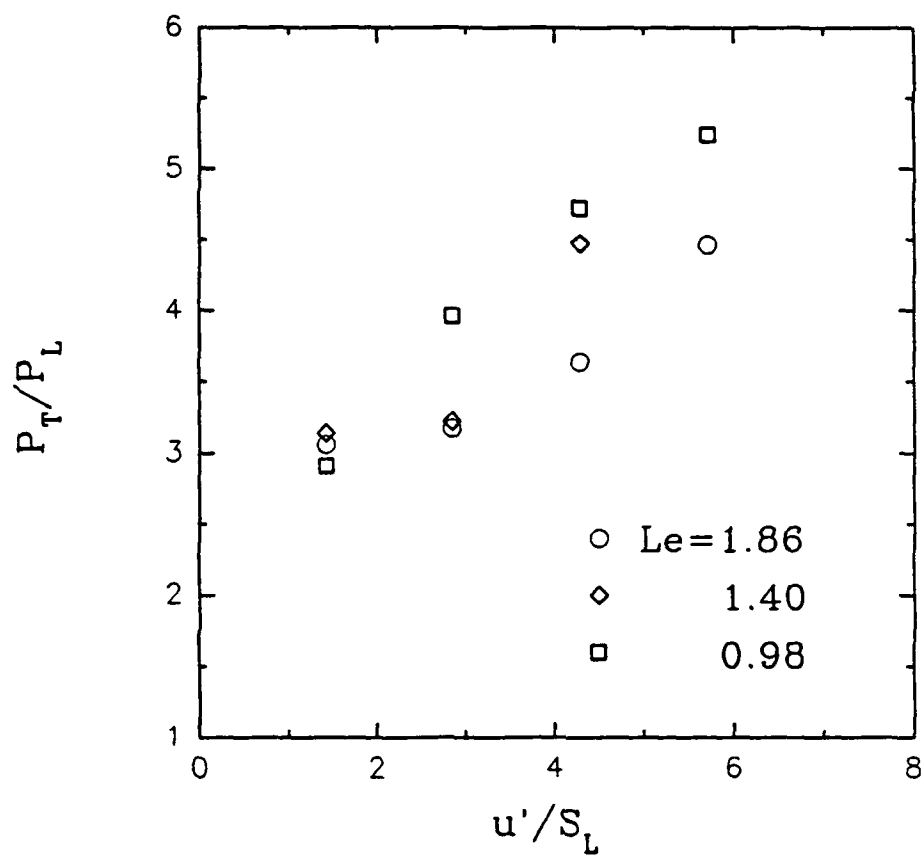


Fig. 9. Normalized wrinkled flame perimeter as a function of u'/S_L for $Le=0.98-1.86$.

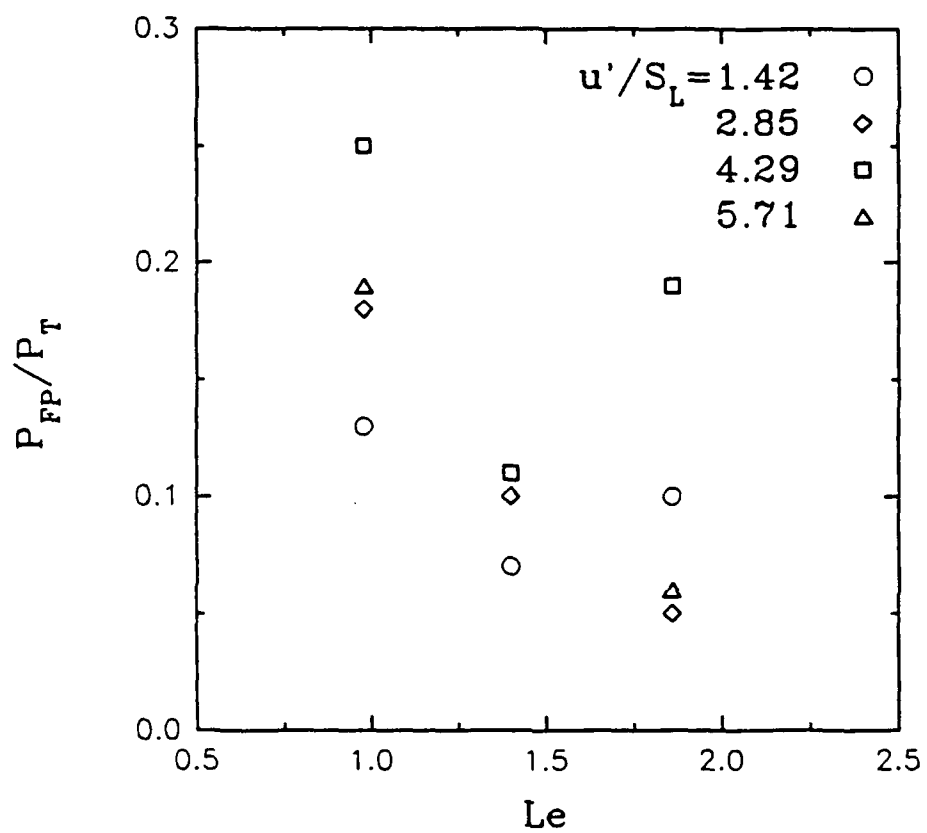


Fig. 10. Ratio of the flame pocket perimeter to the total wrinkled flame perimeter.

FLAME FRONT GEOMETRY AND STRETCH DURING INTERACTIONS OF PREMIXED FLAMES WITH VORTICES

T.-W. Lee and D.A. Santavicca

Turbulent Combustion Laboratory
Department of Mechanical Engineering
Propulsion Engineering Research Center
Penn State University

Abstract- Flame front geometry and flame stretch during interactions of premixed flames with vortices at various configurations are computationally investigated using a kinematical relationship between vortex-induced velocity and flame propagation velocity, in conjunction with Lagrangian coordinates to represent the flame front. The maximum flame stretch that can occur during an interaction with a single vortex is found to be very close to $U_\theta/r_m + S_L/2r_m$, while the mean flame stretch has a maximum that asymptotes to 18 - 23 % of this value for vortex radii between 1.25 and 5.0 mm as U_θ/S_L is increased to 2. For flames interacting with a counter-rotating vortex pair, the flame stretch near the flow symmetry axis increases when the spacing between the vortices increase to align the velocity vectors with the flame front; while the flame stretch away from this region is relatively independent of the action of the opposite vortex and is determined primarily by the vortex velocity and length scale similar to the single vortex case. For flame contours caused by vortex arrays, the flame curvature scales more strongly with vortex size than vortex velocity; and the mean flame curvatures for both vortex arrays and a single vortex are bounded between $1/d_m$ and $1/(2d_m)$ except in an instance where the vortex produces negligible wrinkles on the flame front. The effect of decreasing the tangential spacing in the vortex array is to increase the coupling of actions of adjacent vortices which leads to an increase in flame area and a positive shift in the flame curvature pdf; while variations of normal vortex spacing have less effect on the flame front geometry. The maximum flame stretch for flames interacting with vortex arrays is found to be close to the value caused by a single vortex, whereas the mean flame stretch and higher statistical moments are significantly different due to the additional strains caused by the coupling of actions of adjacent vortices.

NOMENCLATURE

A_o	undisturbed flame area
A_w	wrinkled flame area
d_m	characteristic vortex diameter ($2r_m$)
H	flame curvature
K_{max}	maximum flame stretch during interaction
$\langle K \rangle_{s,max}$	maximum in area-weighted mean flame stretch during interaction
K^*	estimate of maximum flame stretch during interaction
\underline{n}_f	unit flame normal vector
r	radial distance from vortex center
r_m	characteristic vortex radius
Re_D	Reynolds number based on the vortex generating rod diameter
Re_L	turbulence Reynolds number
s	distance along flame contour
S_L	laminar flame speed
t	time
\underline{u}_f	flame element velocity vector
\underline{U}_i	vortex-induced velocity vector
\underline{U}_m	mean flow velocity vector
U_θ	maximum vortex tangential velocity
x	horizontal distance
\underline{x}_f	flame element position vector
y	vertical distance
Γ'	vortex strength parameter

δ_L	laminar flame thickness
Δ_n	normal vortex spacing
Δ_t	tangential vortex spacing
μ_K	skewedness in flame stretch
σ_K	variance in flame stretch
τ_c	characteristic interaction time
$\langle + \rangle$	area-weighted positive mean
$\langle - \rangle$	area-weighted negative mean

INTRODUCTION

Current understanding and predictive capabilities for turbulent premixed flames are limited in spite of their wide practical applications and their importance as one of the central problems in combustion fluid dynamics. One of the well-known difficulties is the lack of a rigorous method to predict the turbulent flow field. One approach devised in order to circumvent this difficulty is to describe the turbulent flow field as an array of deterministic vortices that obey a certain energy distribution and focus on the behavior of premixed flames responding to this flow field. This approach has been used by Ghoneim et al. (1983) and Ashurst and coworkers (1983,1987) to model turbulent premixed flames by simulating the flow field with a set of discrete vortices and computing the flame front motion via a simple-line interface calculation (SLIC) algorithm (Noh and Woodward, 1976). Another similar approach is to consider the effect of a unit vortex on the premixed flame and to integrate the effects of individual vortices over a hierarchy of vortex scales that make up the turbulent flow field. For example, a method by Weller et al.(1990) considers the flame area

generated by a vortex of a given scale and integrates over the eddy strength distributions, while including the interaction between different eddy scales. A recent model by Meneveau and Poinso (1991) similarly superposes the flame stretch imposed by a single vortical structure over the vortex spectrum in order to calculate the overall flame stretch.

In this regard, two important elements of flame-vortex interactions emerge as fundamental components in understanding and modeling of turbulent premixed flames. First, the full characteristics of flame fronts interacting with the simplest vortex structure, i.e. a "unit" vortex, need to be accurately known. The most fundamental unit vortex is, of course, a single isolated vortex. However, flames interacting with a counter-rotating vortex pair have received recent research attention (Poinso et al., 1991; Roberts and Driscoll, 1991; Wu and Driscoll, 1992) due to the convenience with which the results can be compared with experimental data since a single isolated vortex is not easily generated experimentally. During such an interaction, of interest are (1) the changes in fluid dynamic properties across the flame such as the baroclinic vorticity generation and changes in vortex structures due to heat release effects, (2) the flame surface properties such as the flame area increase, flame curvature and topological changes (singly-connected or multiply-connected flames); and (3) the flame stretch distribution along the flame front since this can lead to departure of flame properties from unstrained laminar values and under severe flame stretch to quenching. Some of these issues have been, or are actively being, investigated by various researchers (Rutland and Ferziger, 1991; Ashurst and McMurtry, 1988, Poinso et al., 1991; Roberts et al., 1992; Chate and Cant, 1988). The second important element in flame-vortex interactions is the effect of multiple vortices upon the above-mentioned characteristics, since usefulness of the above-mentioned information depends in some applications on the knowledge of how the effects of individual vortices can be integrated to yield an overall picture of turbulent premixed flames.

In view of this, this study will investigate aspects of premixed flame fronts interacting with vortices at various configurations by using a numerical scheme that simulates flame front motion via

a kinematical relationship between vortex-induced velocity and flame propagation velocity. In particular, flame stretch, flame curvature and their dependence on vortical properties and configurations will be investigated by examining interactions with a single vortex, a vortex pair, and a vortex array. The information concerning the interaction with a single vortex can clarify some of the issues regarding the flame behavior caused by a unit vortex, while results concerning vortex pairs and vortex arrays are expected to bring insight as to how the presence of multiple vortices affect the nature of these fundamental flame-vortex interactions.

NUMERICAL METHODS

The present numerical algorithm considers the flame as a two-dimensional propagating surface convected by the fluid motion while advancing at the local laminar flame velocity. The flame front is represented by discrete points whose coordinates evolve in time according to the kinematical relationship between the vortex-induced rotational velocity (\underline{U}_i), the normal propagation velocity ($S_L \underline{n}_f$) and the mean flow velocity (\underline{U}_m):

$$\underline{u}_f(\underline{x}_f, t) = \sum_i \underline{U}_i + S_L \underline{n}_f + \underline{U}_m \quad (1)$$

where \underline{u}_f and \underline{n}_f are the velocity and the unit normal vectors of a point at \underline{x}_f on the flame front, respectively. The principle embodied in Eq. (1) has been used by various researchers (Ghoniem et al., 1983; Ashurst, 1987; Kwon et al., 1992) in conjunction with SLIC algorithm for simulations of turbulent premixed flames and also for statistical treatment of flame surface properties in isotropic turbulence (Pope, 1988). Use of Lagrangian grid points on the flame front in the present numerical algorithm in place of SLIC has advantages in enhanced spatial resolution with minimal computational requirements and in its unique ability to directly compute local flame stretch rates at each time step,

while the self-intersections of flame fronts at cusp points can be detected and excluded by comparing simultaneously the positions and slopes of all the points on the flame front. However, detection of the self-intersections itself requires moderate computational time; and in instances where the self-intersections of the flame fronts are so numerous as in high Reynolds number turbulent flames it may be preferable to use the G equation method or SLIC method similar to Ashurst and Sivashinsky (1991) and Kwon, et al. (1992), respectively.

The positions of the vortices are fixed in space, while the rotational velocity of an individual vortex is given the same functional form used by Rutland and Ferziger (1991):

$$|\underline{U}_i| = (\Gamma' r / r_m^2) \exp(-r^2 / 2r_m^2) \quad (2)$$

where Γ' and r are the vortex strength parameter and distance from the vortex center, respectively. The maximum vortex rotational velocity of $U_\theta = \Gamma' e^{-1/2} / r_m$ occurs at the radial distance of r_m , and these quantities are used as the characteristic vortex velocity and length scales, respectively. For multiple flame-vortex interactions, the effects of individual vortices are summed as in Eq. (1). The flame speed, S_L , is assumed to be constant, although the local instantaneous flame stretch along the flame front is available from the computation and can be used to determine the modified local laminar flame speed. Also, implicit in this formulation is the assumption of constant properties across the flame. The most important consequence of this assumption is that the vortex properties are "frozen" (Rutland and Ferziger, 1991) across the flame when in reality the vortices become dilated and elongated as they pass through the flame. This assumption of fluid dynamics being unaffected by the presence of the flame is widely used in studies of turbulent premixed flames (Ashurst and Sivashinsky, 1991; Yakhot, 1988; Kwon et al., 1992; Cant et al., 1990) and flame-vortex interactions (Chate and Cant, 1988; Wu and Driscoll, 1992), since the alternative is to perform a direct numerical simulation which is certainly not feasible at present for high Reynolds number turbulent flows. The

limitation of this assumption therefore should be further investigated since baroclinic vorticity generation and heat release effects on the flow field can have feedback effects on the flame structures. For flame-vortex interaction studies, the full coupling of fluid dynamics and heat release has been treated by Rutland and Ferziger (1991), Ashurst and McMurtry (1988), and Poinso et al. (1991), although the limitations of the frozen vortex assumption have not been directly addressed in these studies. A detailed consideration of the validity and limitations of this assumption is outside the scope of the study and will be addressed elsewhere (Lee et al., 1992b).

The computational procedure is schematically illustrated in Fig. 1. Equidistant grid points are embedded along an undisturbed planar flame front far from the vortices. Initially, there is no flow disturbance due to the vortices, thus each point on the flame surface propagates normal to itself. As the flame front approaches the vortices, the rotational velocity of the individual vortices starts to wrinkle the flame front. The first step in the computation involves putting the flame coordinates in an (r, θ) coordinate system and calculating the flame normal vector components using centered differencing. Next, the distance and angle from the vortex centers to each point on the flame front are calculated to give the magnitude and direction of the vortex tangential velocities. Finally, the normal flame propagation and vortex velocity components are added in (r, θ) coordinates, and the flame front motion is advanced in time using Euler integration. Due to fluid dynamic strain and flame curvature, i.e., flame stretch effects, initially equidistant surface points can drift further apart or be compressed closer together. By computing the time rate of change of the distance between adjacent points, the local instantaneous flame stretch along the flame front can be conveniently calculated. This is a unique feature in the present computation that allows an efficient calculation of flame stretch in contrast to the conventional method which involves tedious calculations of the scalar product between the strain tensor and the flame tangent vector while simultaneously computing the flame curvature contribution (Candel and Poinso, 1990). The number of grid points necessary to achieve optimum spatial resolution depends on the flame stretch imposed on the flame front: 400-

4000 points encompassing 40 mm in real space are used for U_θ / S_L ranging from 0.25 to 2.0. Computations are performed on a VAX-11 computer and typically require less than 1 hour of CPU time.

RESULTS AND DISCUSSION

Figures 2(a) and (b) show, respectively, flame contours caused by a counter-rotating vortex pair and a single isolated vortex for a characteristic vortex radius of 5 mm. Flame contours similar to those in Figure 2(a) have been observed experimentally by Roberts and Driscoll (1991) for flames interacting with a three-dimensional vortex ring, which in two dimensions can be represented by a pair of counter-rotating vortices; although the relative velocity between the flame and the vortices are fixed in this case at the flame propagation speed. Figure 2(a) shows that for sufficiently high U_θ / S_L , fluid dynamic straining can overtake the flame propagation velocity that can result in the formation of reactant pockets similar to the experimental findings (Roberts and Driscoll, 1991). For $U_\theta / S_L = 2.0$, the flame front elements near the symmetry axis will propagate toward one another and intersect before the flame elements in the concave region can propagate and consume the reactants in the pocket. This pocket formation process is due to the kinematics between flame propagation and fluid dynamic straining; thus, not only U_θ / S_L and r_m but also the vortex spacing and the number and sense of rotation of vortices determine the propensity of flames to form reactant pockets. For example, for a single vortex with identical strength the formation is somewhat more difficult as shown in Figure 2(b), since a much stronger roll-up action is required to close the small concave region near the vortex center before flame elements propagate toward one another to "fill" this region. The flame contours for a single vortex in Figure 2(b) are comparable to the results of direct numerical simulations performed by Rutland and Ferziger (1991) for both full and frozen vortex interactions, although for frozen vortex computations at similar U_θ / S_L the direct numerical simulations show a

somewhat more extensive concave (toward the reactant) region. In Figure 2(b), the convex region is extended due to the outward flame propagation at positively curved (convex toward the reactant) regions. This difference may be due to finite flame thickness in the direct numerical simulations and the difference in the time at which the flame contours have been sampled.

In Rutland and Ferziger (1991), attention is focused on the changes in vorticity distribution across the flame and the effect of Damköhler number on the nature of the flame-vortex interaction, but flame stretch during the interaction is not included in the computations. Flame stretch is an important characteristic of flame-vortex interactions since it not only defines the rate at which the flame area is growing but also determines the departure of flame properties from unstrained values. In a related work, Candel and Poinso (1990) derive a general expression for flame stretch, but only compares the contribution of curvature and strain to flame stretch at the flow symmetry axis for one condition. A more extensive computation of flame stretch can be found in Meneveau and Poinso (1991); however, in that work, the growth rate of the total reaction rate was assumed to be the characteristic flame stretch for flames interacting with a vortex pair. While this is useful information and in fact has been used in their model to predict quenching of turbulent premixed flames, two aspects of flame stretch during flame-vortex interactions should be further investigated in flame stretch calculations. First, the growth rate of the total reaction rate is more representative of mean flame stretch during a flame-vortex interaction, and it would be worthwhile to examine the entire flame stretch distribution along the flame contour since local variations in curvature and strain can lead to significant departures from the mean flame stretch that can cause, if severe enough, local quenching of the flame. Secondly, while vortex pairs are observed in turbulent flows, a more fundamental vortex structure is a single isolated vortex; thus, it would be useful to study the flame stretch during an interaction with a single vortex for various vortex velocities and sizes.

Figure 3 shows the flame stretch distribution for the single vortex configuration shown in Figure 2(b) as a function of the distance along the flame front, s , at various times during the interaction.

The variable s increases from negative to positive as y increases from zero to 0.04 m in Figure 3(b). Initially, when the flame front is relatively far from the vortex strain field, there is only a simple weak fluctuation from negative to positive flame stretch. As time increases, a structure in flame stretch along the flame front develops where peaks in positive and negative flame stretch appear near the vortex center; while the flame stretch structures in the outer region are primarily due to curvature effects, since the distance from the vortex center is relatively large and thus fluid dynamic strain relatively weak. The region associated with the maximum positive flame stretch grows more and more extensive due to the positive flame curvature that causes the flame front to propagate outward, thus increasing the flame area. Outward flame propagation also decreases the flame curvature; and at later times when flame front moves away from the vortex, diminishing contributions from both curvature and strain cause the positive flame stretch to decrease after reaching its peak. The peak in the negative flame stretch, on the other hand, is associated with negative flame curvature whose magnitude increases in time with inward flame propagation. Thus, the negative peak grows indefinitely in time until finally a cusp is formed on the flame front. In real flames, the flame curvature is limited by the flame thickness and the magnitude of the minimum negative flame stretch is expected to be of the order of S_L/δ_L and highly localized to a small region.

From flame stretch distributions such as those shown in Figure 3, three quantities are of interest. One is the maximum positive flame stretch since this determines the maximum departure of flame properties from unstrained values, aside from cusp points. Similarly, area-weighted mean flame stretch defines the mean change in the flame properties from unstrained values, as well as determining the growth rate of the overall flame area. Finally, the characteristic interaction time represents the duration that the flame front is subject to flame stretch in the absence of additional translational velocities.

These quantities are plotted in Figures 4 and 5. In Figure 4, the maximum flame stretch encountered during the interaction, K_{\max} , normalized by U_θ/r_m does not differ appreciably for

different vortex radii, indicating that K_{\max} can be scaled by the inverse of the vortex radius. However, the ratio of K_{\max} to U_{θ}/r_m ranges from about 3 to 1 as U_{θ}/S_L is increased from 0.25 to 2, which suggests that K_{\max} does not scale with U_{θ} in a simple fashion. This is due to the fact that at low U_{θ}/S_L , curvature contribution to flame stretch can be significant and the estimate of fluid dynamic strain alone represented by U_{θ}/r_m underestimates the actual maximum flame stretch by a factor of 2-3 when U_{θ}/S_L is less than one. As U_{θ}/S_L increases, however, $K_{\max}/(U_{\theta}/r_m)$ approaches one, which is reasonable since fluid dynamic strain contribution to flame stretch is expected to dominate over flame curvature at high U_{θ}/S_L . It has been customary to use the ratio of fluid dynamic velocity and length scale, U_{θ}/r_m in this case, to estimate the characteristic flame stretch in premixed flames; however, Figure 4 shows two things in regard to this estimate: (1) quantitatively, U_{θ}/r_m should be associated with the maximum local flame stretch that occurs for a given flow field; and (2) flame curvature effects should be included in order to obtain a generalized expression for the maximum flame stretch that is valid throughout the range of U_{θ}/S_L . In fact, by adding $S_L/2r_m$, a curvature contribution term, to U_{θ}/r_m and plotting it on the same graph, a very good agreement between this estimate (K^*) and the actual maximum flame stretch during flame-vortex interactions can be obtained. This is tantamount to approximating the characteristic flame curvature that contributes to the maximum flame stretch with $1/2r_m$; and in instances where the vortex strength is so weak that no wrinkles are produced on the flame front the characteristic flame curvature is obviously zero and the curvature contribution to the maximum flame stretch is also zero. The maximum in area-weighted mean flame stretch, $\langle K \rangle_{s,\max}$ also approaches a constant value as U_{θ}/S_L increases; however, $\langle K \rangle_{s,\max}$ asymptotes to different values depending on the vortex size, ranging from 18-23% of K_{\max} for vortex radius of 5 to 1.25 mm. This trend is similar to the correlation of Meneveau and Poinso (1991) where the characteristic flame stretch is equated with the ratio of the vortex velocity and length scales multiplied by a correction factor that tends to be larger for larger vortices. However, one major difference is that the vortex pair size or the distance between two counter-rotating vortices

was used to characterize the vortex length scale in Meneveau and Poinso (1991), whereas the vortex core radius is used in this case as the fundamental vortex length scale.

A characteristic vortex interaction time, τ_c , is defined as the time interval between K_{\max} and $e^{-1}K_{\max}$ and is plotted in Figure 5 after normalization by r_m/U_θ and by $1/K^*$. Again, normalized interaction time does not differ significantly for different vortex radii, while it increases monotonically with increasing U_θ/S_L . The interaction time tends to be of the order of r_m/U_θ or inverse of K^* , although due to the decay period following the occurrence maximum flame stretch the actual interaction times are longer than τ_c by approximately a factor of two.

The results thus far pertain to flame fronts interacting with a single isolated vortex. An important extension, therefore, is an examination of configurations involving multiple vortices, since turbulent flames involve the superposition of effects of many vortex scales acting upon the flame front. Thus, it is worthwhile to consider flames wrinkled by vortex arrays in order to study how the characteristics of a unit flame-vortex interaction is altered by the presence of multiple vortices. As an intermediate step, we will briefly examine the flame stretch for premixed flames wrinkled by a counter-rotating vortex pair, since this configuration has received considerable attention recently in both computational and experimental investigations (Poinso et al., 1991; Roberts and Driscoll, 1991).

Figure 6 shows that the top half of the flame contours and flame stretch profiles caused by a counter-rotating vortex pair at various vortex spacings denoted by Δ_l , sampled at a reference time that corresponds to the instant when an undisturbed flame front would intersect the vortex centers. For multiple vortices, vortex spacing becomes an additional variable, as can be observed by the changes in flame front geometry and flame stretch, particularly near the symmetry axis in Figure 6. At $\Delta_l/r_m = 1$, the velocity vectors are nearly perpendicular to the flame front at the centerline ($y = z = 0$), and therefore the tangential strain rate is very small. Thus, due to the negative flame curvature at this point, the resultant flame stretch is weakly negative, as shown in Figure 6. As Δ_l/r_m increases, the velocity vectors induced by two vortices become more aligned with the flame front, and since they

point in opposite directions, extensive tangential strain occurs to cause positive flame stretch at the symmetry axis. The flame stretch in the outer region, however, is subject to relatively small change with respect to the variation in Δt due to the fact that the vortex action here is far and independent from the action of the opposite vortex. The changes in flame stretch when vortex spacing is varied has also been observed in direct numerical simulations of Poinso et al. (1991), who demonstrated that when vortices are brought to close proximity, the increase in negative flame curvature at the symmetry axis offsets the positive fluid dynamic straining to prevent flame quenching. The vortex spacing, as defined in this work, corresponds to vortex size as defined in Poinso et al. (1991); however, as shown in Figure 6, the flame stretch near the symmetry axis is affected by the vortex spacing, while the flame stretch in the outer region is similar to that caused by a single vortex. In Poinso et al. (1991) and Roberts et al. (1992), flame quenching, when it occurs, takes place near the symmetry axis; whereas in Figure 6 the flame stretch at the centerline is less than the maximum flame stretch that occurs elsewhere. However, the condition for flame quenching is given at U_θ/S_L of nearly 30, for example in Poinso et al. (1991), and thus is not comparable to the condition in Figure 6, where $U_\theta/S_L = 1$. At such high U_θ/S_L , a stronger tangential strain at the symmetry axis may cause a more severe flame stretch. Furthermore, if there is an additional translation velocity component to the vortex pair, flow stagnation at the leading edge of the vortex structure may cause additional positive tangential strain.

In order to examine the effect of multiple vortices, we can construct a vortex array such as shown in Figure 7. Turbulent flames can be viewed as flames interacting with a series of vortex arrays depicted in Figure 7, where the constituent vortices obey a certain energy spectrum and spatial distribution. The flame fronts in Figure 7 are subject to the coupling of actions of adjacent vortices, not only in the direction parallel but also perpendicular to the flame front. This is an inherent feature in turbulent flames in which many vortices simultaneously act upon curved flame fronts already wrinkled by preceding vortices. Thus, vortex configurations shown in Figure 7 can be used

to investigate the manner in which effects of individual vortices are superposed on the flame front. In contrast to a turbulent flow field, each vortex in the array is assigned the same value of U_θ/S_L and r_m in order to remove the complexity of multiple vortex scales, while tangential and normal vortex spacings (Δt and Δn , respectively, as defined in Figure 7) are fixed for a given configuration. In Figure 7, features reminiscent of turbulent flames are observed in spite of the relative simplicity of the vortex configuration and fixed values of vortex velocity and scale. Furthermore, very different flame shapes result through a simple permutation of vortex signs or vortex sense of rotations. In turbulent flames, the vortex velocity, size, tangential and normal vortex spacings, and vortex signs continuously vary giving rise to an astronomical number of permutations of possible vortex configurations that can act upon the flame front, thus resulting in complex flame shapes. In the following, flame curvature and stretch statistics are obtained by analyzing and averaging over the three representative configurations shown in Figure 7 at a fixed reference time that corresponds to the instant when an undisturbed flame front coincides with the centers of the top and bottom vortices.

The effects of vortex velocity and size on the flame front geometry are exemplified in Figure 8, where flame contours and area-weighted flame curvature probability density functions (pdf's) are plotted. The flame curvature is analyzed by a 5-point curve-fitting routine with a 1 mm interval length and is calculated by:

$$H = [(d^2x/ds^2)^2 + (d^2y/ds^2)^2]^{1/2} \quad (3)$$

The interval length of 1 mm is used for computational efficiency but primarily to avoid near-infinity curvature at cusp points by smoothing over these points with a step size of the order of the flame thickness. Thus, cusp points manifest as negative flame curvature close to the inverse of the interval length of 1 mm in flame curvature pdf's. Flame contours shown in Figure 8 show that at a fixed

vortex radius, higher U_θ/S_L produces more flame area, but there does not appear to be a significant difference in local flame curvature when U_θ/S_L is varied by a factor of two. A more obvious change in flame curvature is observed when the vortex radius is increased by a factor of two at fixed U_θ/S_L . The increase in the scale of the flame wrinkles caused by the larger vortex size has a more direct effect on the flame curvature. This effect is verified in the flame curvature pdf's which shows that when U_θ/S_L is decreased from 1.0 to 0.5 at a fixed vortex radius, there is a shift in the flame curvature distribution toward weak negative curvature; however, this change is small in comparison to that corresponding to a variation in the vortex radius that causes the pdf to sharply peak at a small flame curvature when vortex radius is increased to 5 mm. This suggests that the flame curvature depends more sensitively on vortex size than vortex velocity.

This trend can be verified by plotting mean positive and negative flame curvatures as a function of vortex radius for $U_\theta/S_L = 0.25-1.0$, as in Figure 9. It can be observed that at a fixed vortex radius, higher U_θ/S_L increases the flame curvature; but a more significant variation occurs with changes in vortex size. The two data points that lie outside the dotted band correspond to a condition where the vortices are not sufficiently strong to cause appreciable flame front wrinkling. With that exception, the mean flame curvatures are observed to scale with the inverse of the vortex size and are bounded by $1/d_m$ and $1/(2d_m)$. Furthermore, the mean flame curvature caused by a single vortex (represented by the dark symbols in Figure 9) also tends to be of the order of d_m^{-1} , similar to vortex arrays in spite of the complex flame shapes caused by multiple vortices. The scaling trend observed in Figure 9 may explain the experimental observation that the mean flame curvature in turbulent flames is inversely proportional to the Taylor scale of the approach flow turbulence for Re_L ranging from 140 to 570 (Lee et al., 1992), although a hierarchy of vortex scales exists in turbulent flows and further study is needed to resolve the behavior of flame curvature in the presence of multiple vortex scales. Nonetheless, flame curvature is an important property that not only characterizes the flame surfaces, but also contributes to flame stretch regardless of the shape of the flame curvature pdf; and

scaling behavior shown in Figure 9 can assist in estimating and incorporating flame curvature effects in turbulent flame modeling.

The effect of tangential and normal vortex spacing is investigated, as shown in Figure 10. A prevalent modeling approach in turbulent premixed flames is to consider the effects of a unit vortex on the flame and integrate these effects over the spectrum of vortices that make up the turbulent flow field in a linear superposition. An example is the approach by Meneveau and Poinso (1991) mentioned earlier where characteristic flame stretch is correlated with a vortex of a given velocity and length scale and the mean flame stretch, for instance, is obtained by integrating the characteristic flame stretch over the vortex scale distribution. An implicit assumption in this approach is that the distance between adjacent vortices is sufficiently large so that the action of an individual vortex is independent from the actions of other vortices or that the coupling of actions of adjacent vortices are simple enough so that a modelling constant can fully account for this effect. However, turbulent flames are a complex amalgam of actions of neighboring vortices, and as the vortex spacing becomes of the order of the vortex diameter, nonlinear effects on the flame front geometry and flame stretch result which cannot be treated through a simple superposition procedure. Figures 10 (a) and (b) show, in this regard, the effect of vortex spacing on the flame curvature pdf and flame area. For example, at $\Delta_t/r_m = 2$ the flame curvature pdf undergoes a pronounced shift toward positive curvature from a pdf with very small asymmetry at $\Delta_t/r_m = 4$. This is due to the fact that the flame curvature distribution for a single vortex at this reference time has a very small asymmetry with respect to zero curvature; and as the tangential vortex spacing increases, the vortices are acting upon the flame front in a nearly independent manner from the interference from the neighboring vortices thus causing a flame curvature distribution not significantly different from that of a single vortex. In contrast, the effect of the normal vortex spacing is such that the flame front is wrinkled by the leading vortex, but in time, this wrinkle relaxes to yield a weak curvature that interacts with subsequent vortices, and thus, the changes in both flame area and flame curvature pdf are minimal. Figure 10

(b) illustrates the significant effect of tangential vortex spacing on the flame area. At large Δ_t/r_m of 4, the coupling of actions of neighboring vortices is weak and yields relatively small flame area increase, while for Δ_t/r_m of 2 the fractional area increase is nearly a factor of two larger at all U_θ/S_L . The fractional area increase for Δ_t/r_m of 4 does not differ appreciably from the single vortex data (dark symbols), which is reasonable since for a relatively large Δ_t/r_m each vortex in the array acts upon the flame in a nearly independent manner from the actions of adjacent vortices.

Area-weighted flame stretch statistics can also be examined as shown in Figure 11. In typical Eulerian computations of flame stretch, the strain tensor is calculated at all of the grid points and a scalar product with flame tangent vectors is obtained, which gives the fluid dynamic tangential strain rate. In addition, curvature along a constant property surface, say a constant reaction progress variable, is computed to give the flame curvature contribution to flame stretch. This type of computation can obviously be expensive. In contrast, a relatively simple algorithm involving Lagrangian coordinates used in the present method allows an efficient calculation of flame stretch along the flame front exactly according to the definition of flame stretch. Figure 11 shows the flame stretch pdf's for U_θ/S_L ranging from 0.25 to 1.0 while the other vortex parameters are kept constant. In addition, the pdf for HS_L , i.e., the curvature contribution to flame stretch, at $U_\theta/S_L = 1.0$, is included to assess the importance of flame curvature in flame stretch statistics. The expected increase in flame stretch with increasing U_θ/S_L is shown in Figure 11. The pdf's at all U_θ/S_L are characterized by predominance of positive flame stretch which becomes more pronounced with increasing U_θ/S_L , while severe negative flame stretch occurs in very small probabilities since this is mostly associated with the small area near the cusp points. In direct numerical simulations of premixed turbulent flames, prevalent tangential strain rates are also observed (Haworth and Poinso, 1992) with pdf's qualitatively similar to those in Figure 11. The major differences, in this case, are that there is an additional contribution from asymmetric flame curvature distribution and that a single vortex velocity and length scale is present; thus, a direct comparison with fully turbulent cases is difficult. The

curvature contribution at $U_\theta/S_L = 1$, as can be seen in Figure 11, is significant as the HS_L pdf occupies a large proportion of the total flame stretch.

In Figure 11, the maximum flame stretch is found to be similar to the values encountered during an interaction with a single vortex. Table I lists the various statistical moments of flame stretch for both the vortex array and a single vortex. The data for the single vortex has been sampled at the instant that an undisturbed flame front coincides with the vortex center, comparable to the reference time defined for the vortex arrays. It can be seen that the largest difference in K_{\max} is only about 10%, indicating that the information contained in Figure 4 regarding the maximum flame stretch is applicable to situations where a number of vortices act upon the flame front. However, the actual flame stretch statistics are very different between vortex arrays and single vortices, as shown in Table I. The mean flame stretch, for example, is substantially larger for the vortex arrays at all U_θ/S_L values. In fact, for a very small U_θ/S_L the mean flame stretch for the single vortex at this instant can be slightly negative, although the mean flame stretch soon thereafter recovers to positive values associated with the weak increase in flame area. The fact that the vortex arrays generate higher mean flame stretch not only indicates that multiple vortices produce significantly higher flame areas, as has been previously observed in Figure 10 (b), but also that the mean departure of flame properties from unstrained values are higher for the vortex arrays. The positive mean flame stretch ($\langle K^+ \rangle_s$) and skewedness (μ_K) both show that the bias toward positive flames stretch is much stronger for vortex arrays than for single vortices. The results in Table I suggest that a simple summing of the effects of individual vortices is far removed from realistic situations where the coupling of actions of adjacent vortices can produce very different flame stretch statistics.

CONCLUSIONS

From the considerations above, the following conclusions are made concerning the flame front

geometry and flame stretch during flame-vortex interactions:

(1) A kinematical relationship between vortex-induced velocity and flame propagation velocity can be used, in conjunction with Lagrangian coordinates to represent the flame front, to efficiently calculate not only the flame motion but more importantly spatially-resolved time-dependent flame stretch during flame-vortex interactions.

(2) The maximum flame stretch during an interaction with a single vortex can be estimated by $K^* = U_\theta/r_m + S_L/2r_m$, which includes the curvature contribution term; while the maximum in mean flame stretch asymptotes to 18 -23 % of K^* for $r_m = 1.25 - 5$ mm as U_θ/S_L is increased to 2 and beyond. The flame-vortex interaction time is of the order of the $(K^*)^{-1}$.

(3) For flames interacting with a counter-rotating vortex pair, the flame stretch near the flow symmetry axis increases when the spacing between the vortices increase to align the velocity vectors with the flame front, while the flame stretch structure away from this region is relatively independent of the action of the opposite vortex and is determined primarily by the vortex velocity and length scale similar to the single vortex case.

(4) For flame contours caused by vortex arrays, the flame curvature scales more strongly with vortex size than vortex velocity; and the mean flame curvatures for both vortex arrays and single vortices are bounded between $1/d_m$ and $1/(2d_m)$ except in an instance where the vortex produces negligible wrinkles on the flame front. The effect of decreasing the tangential spacing in the vortex array is to increase the coupling of actions of adjacent vortices that leads to an increase in flame area and significant changes in flame curvature statistics, while variations of normal vortex spacing have less effect on the flame front geometry.

(5) The maximum flame stretch for flames interacting with vortex arrays is found to be close to the value caused by a single vortex; while the mean flame stretch and higher statistical moments are significantly different due to the additional strains caused by coupling of actions of adjacent vortices.

ACKNOWLEDGEMENTS

The support for this research has been provided in part by the Air Force Office of Scientific Research under Grant AFOSR-90-0025, Dr. Julian Tishkoff as program monitor.

REFERENCES

- Ashurst, W. T. and Barr, P. K. (1983). Stochastic Calculation of Laminar Wrinkled Flame Propagation Via Vortex Dynamics. Combust. Sci. Tech., 34, 227.
- Ashurst, W. T. (1987). Vortex Simulation of Unsteady Wrinkled Laminar FLAMES. Combust. Sci. Tech., 52, 325.
- Ashurst, W. T. and Sivashinsky, G. I. (1991). On Flame Propagation Through Periodic Flow Fields. Combust. Sci. Tech., 80, 159.
- Candel, S. M. and Poinso, T. J. (1990). Flame Stretch and the Balance Equation for the Flame Area. Combust. Sci. Tech., 70, 1.
- Cant, R. S., Pope, S. B. and Bray, K. N. C. (1990). Modelling of Flamelet Surface-to-Volume Ratio in Turbulent Premixed Combustion. Twenty-Third Symposium (International) on Combustion, The Combustion Institute, Pittsburgh, pp. 809-815.
- Chate, H. and Cant, R. S. (1988). Relevant Scales in the Corrugated Flamelet Regime. Combust. Flame, 74, 1.
- Ghoneim, A. F., Marek, C. J. and Oppenheim, A. K. (1983). Modeling Interface Motion of Combustion (MIMOC), NASA TP-2132.
- Haworth, D. C. and Poinso, T. J. (1992). Numerical Simulation of Lewis Number Effects in Turbulent Premixed Flames. Combust. Sci. Tech., to appear.
- Kwon, S., Wu, M. -S., Driscoll, J. F. and Faeth, G. M. (1992). Flame Surface Properties of Premixed

- Flames in Isotropic Turbulence: Measurements and Numerical Simulations. Combust. Flame, 88, 221.
- Lee, T. -W., North, G. L. and Santavicca, D. A. (1992a). Curvature and Orientation Statistics of Turbulent Premixed Flame Fronts. Combust. Sci. Tech., 84, 121.
- Lee, T. -W., Lee, J. G., Nye, D. A. and Santavicca, D. A. (1992b). Interaction of Premixed Flames with Kármán vortex streets, in preparation.
- Meneveau, C. and Poinso, T. (1991). Stretching and Quenching of Flamelets in Premixed Turbulent Combustion. Combust. Flame, 86, 311.
- Noh, W. T. and Woodward, P. (1976). SLIC, Simple Line Interface Calculations. Fifth International Conference on Numerical Methods in Fluid Dynamics (A. I. Vooren and D. J. Zanbergen, Eds.), Springer-Verlag, Berlin, pp. 330-339.
- Poinso, T., Veynante, D. and Candel, S. (1991). Quenching Processes and Premixed Turbulent Combustion Diagrams. J. Fluid Mech., 228, 561.
- Pope, S. B. (1988). Evolution of Surfaces in Turbulence. Intl. J. Engng. Sci., 26, 445.
- Roberts, W. L. and Driscoll, J. F. (1991). A Laminar Vortex Interacting with a Premixed Flame: Measured Formation of Pockets of Reactants. Combust. Flame, 87, 245.
- Roberts, W. L., Driscoll, J. F., Drake, M. C. and Ratcliffe, J. W. (1992). OH Fluorescence Images of the Quenching of a Premixed Flame During an Interaction with a Vortex. Twenty-Fourth Symposium (International) on Combustion, The Combustion Institute, Pittsburgh, to appear.
- Rutland, C. J. and Ferziger, J. H. (1991). Simulations of Flame-Vortex Interactions. Combust. Flame, 84, 343.
- Wu, M.-S. and Driscoll, J. F. (1992). A Numerical Simulation of A Vortex Convected Through a Laminar Premixed Flame. Combust. Flame, to appear.

List of Tables

Table I. Comparison of flame stretch statistics for vortex arrays and single vortices.

List of Figures

Figure 1. A schematic of the computational procedure.

Figures 2 (a) and (b). Flame contours caused by (a) a counter-rotating vortex pair and (b) a single isolated vortex.

Figure 3. Flame stretch along the flame contour in Figure 3 (b) at various times.

Figure 4. Maximum flame stretch during an interactions with a single vortex.

Figure 5. Characteristic interaction times: $\tau_c = t(K_{\max}) - t(e^{-1}K_{\max})$.

Figure 6. Flame contours and flame stretch during interactions with a counter-rotating vortex pair.

Figure 7. Flame contours caused by vortex arrays.

Figures 8 (a) and (b). Effects of the vortex velocity and size on (a) flame contours (top) and (b) flame curvature pdf's (bottom).

Figure 9. Dependence of mean flame curvatures on vortex radius.

Figures 10 (a) and (b). Effects of vortex spacings on (a) flame curvature pdf's (top) and (b) fractional flame area increase (bottom).

Figure 11. Flame stretch pdf's at various U_θ/S_L .

Table I. Comparison of flame stretch statistics for vortex arrays and single vortices*.

U_θ/S_L	0.25	0.5	1.0	0.25	0.5	1.0
	<u>Vortex Array</u>			<u>Single Vortex</u>		
$\langle K \rangle$	12.73	23.88	47.60	-0.74	3.63	28.99
σ_K	34.12	48.60	64.55	26.97	51.97	71.78
μ_K	121.4	168.7	1028.9	-189.8	-391.6	674.24
$\langle K^+ \rangle$	19.44	32.12	56.36	7.81	18.29	41.66
σ_K^+	19.32	26.65	38.67	11.15	23.86	45.15
$\langle K^- \rangle$	-6.70	-8.23	-8.76	-8.54	-14.66	-12.67
σ_K^-	17.04	25.49	26.39	19.18	35.12	32.18
K_{\max}	73.5	107.5	177.5	62.3	105.1	161.9

* $r_m = 2.5\text{mm}$; units are in s^{-1} for flame stretch statistics.

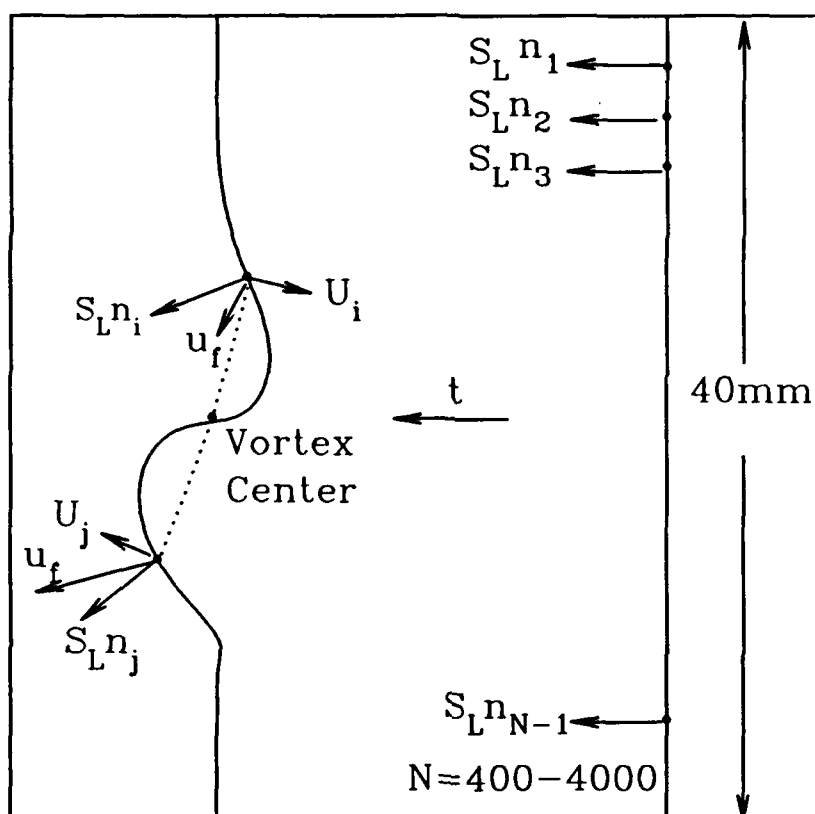
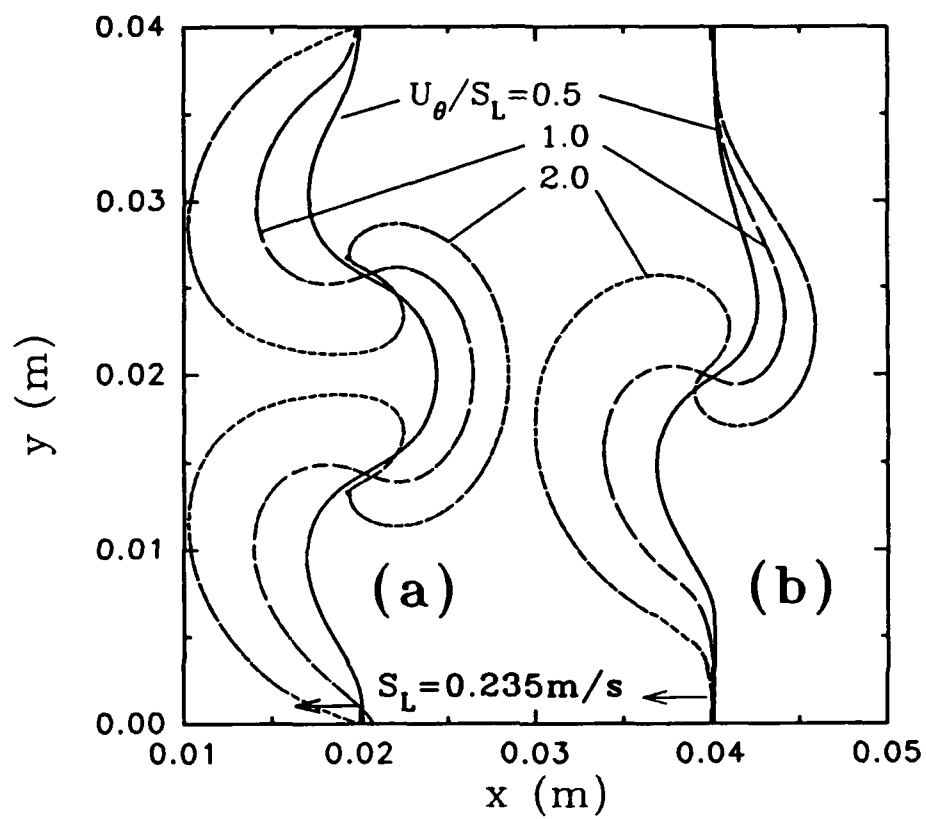


Figure 1. A schematic of the computational procedure.



Figures 2 (a) and (b). Flame contours caused by (a) a counter-rotating vortex pair and (b) a single isolated vortex.

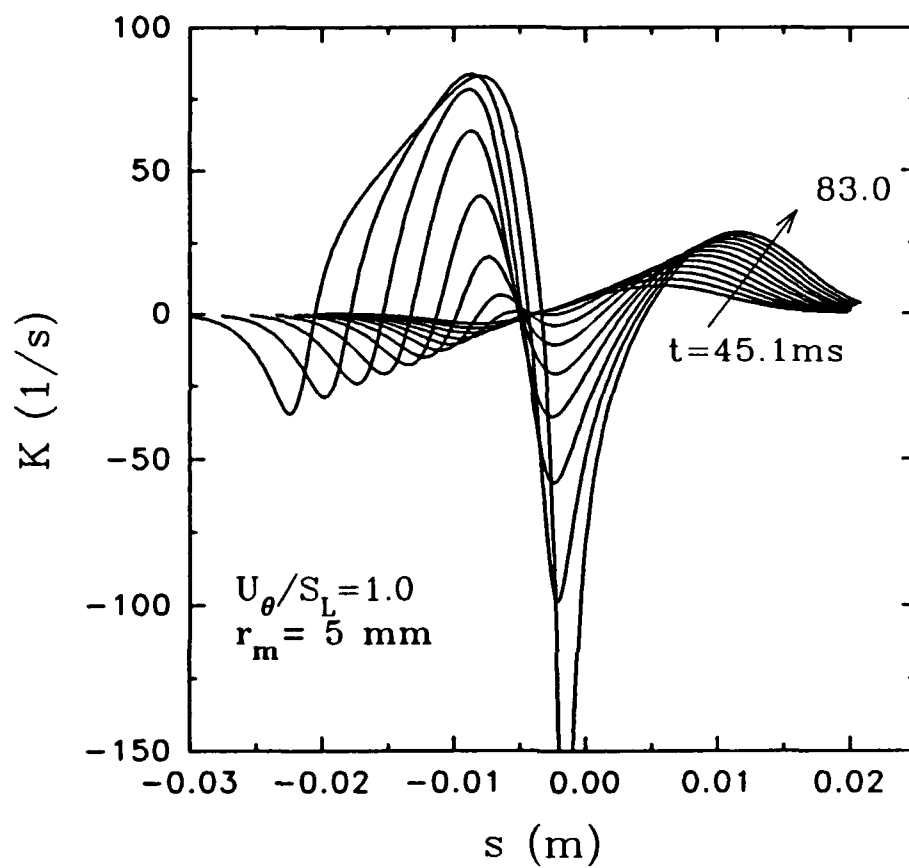


Figure 3. Flame stretch along the flame contour in Figure 3 (b) at various times.

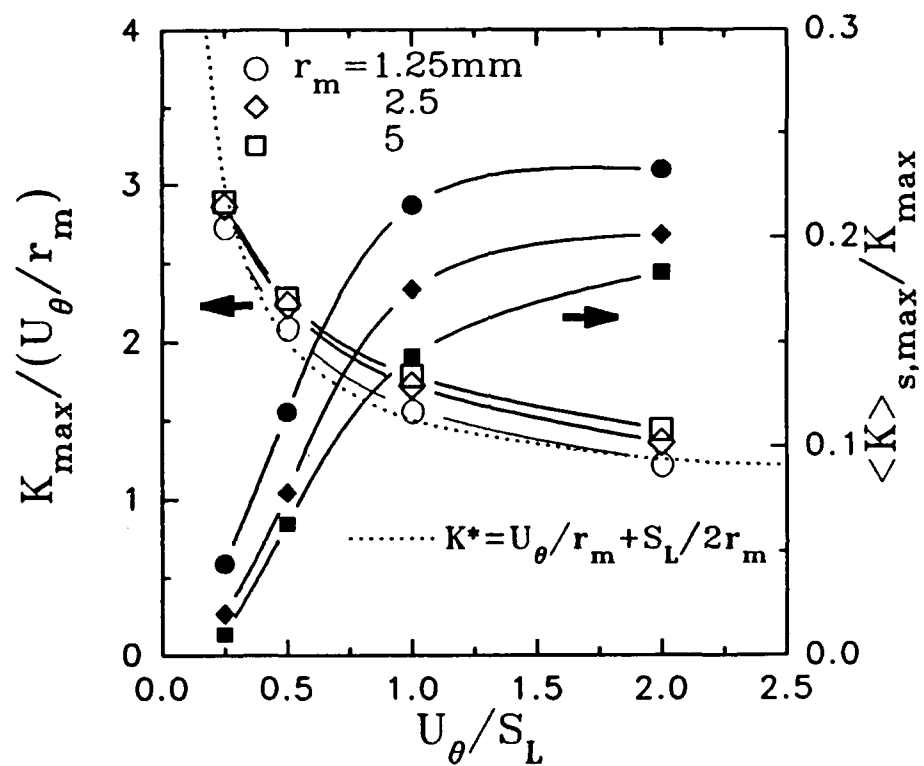


Figure 4. Maximum flame stretch during an interactions with a single vortex.

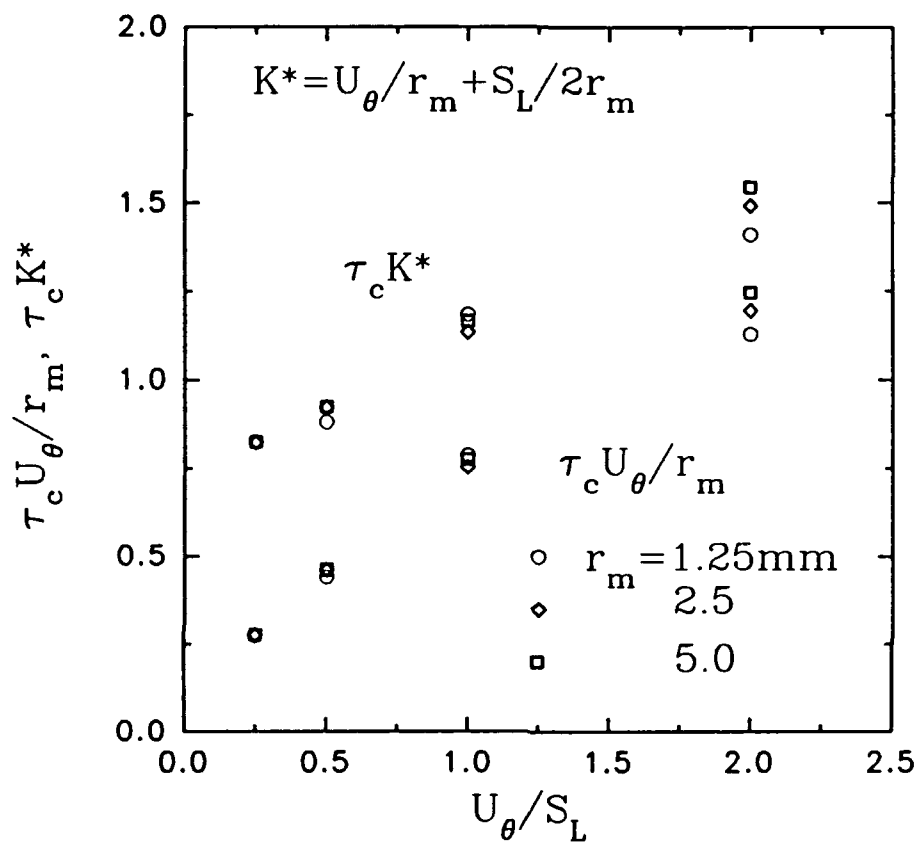


Figure 5. Characteristic interaction times: $\tau_c = t(K_{\max}) - t(e^{-1}K_{\max})$.

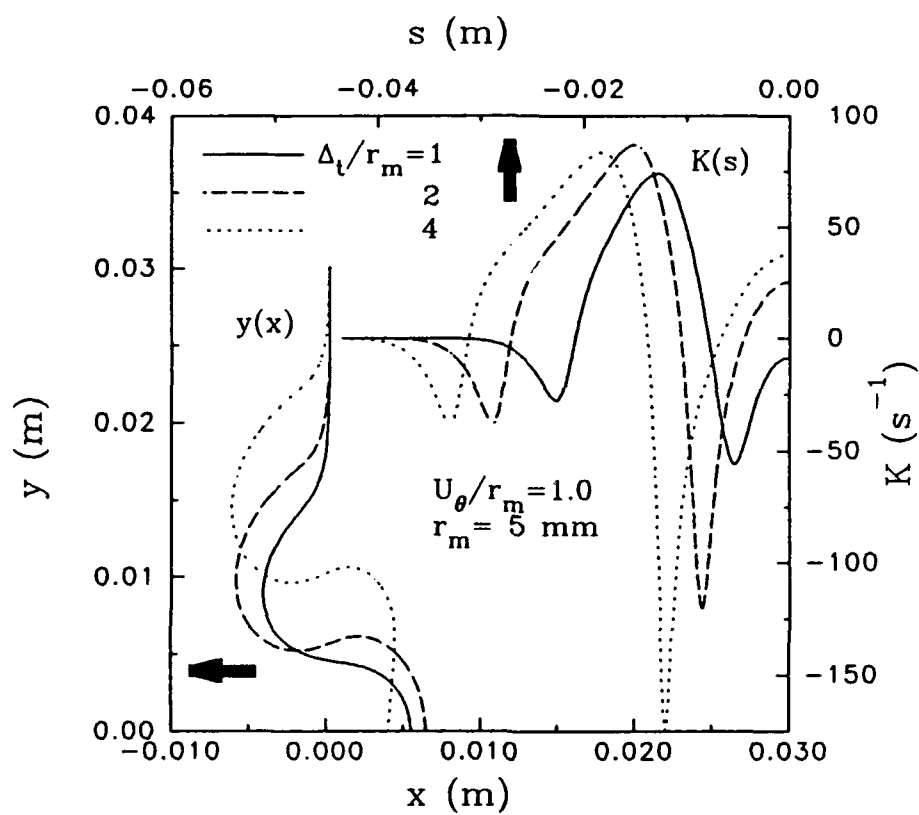


Figure 6. Flame contours and flame stretch during interactions with a counter-rotating vortex pair.

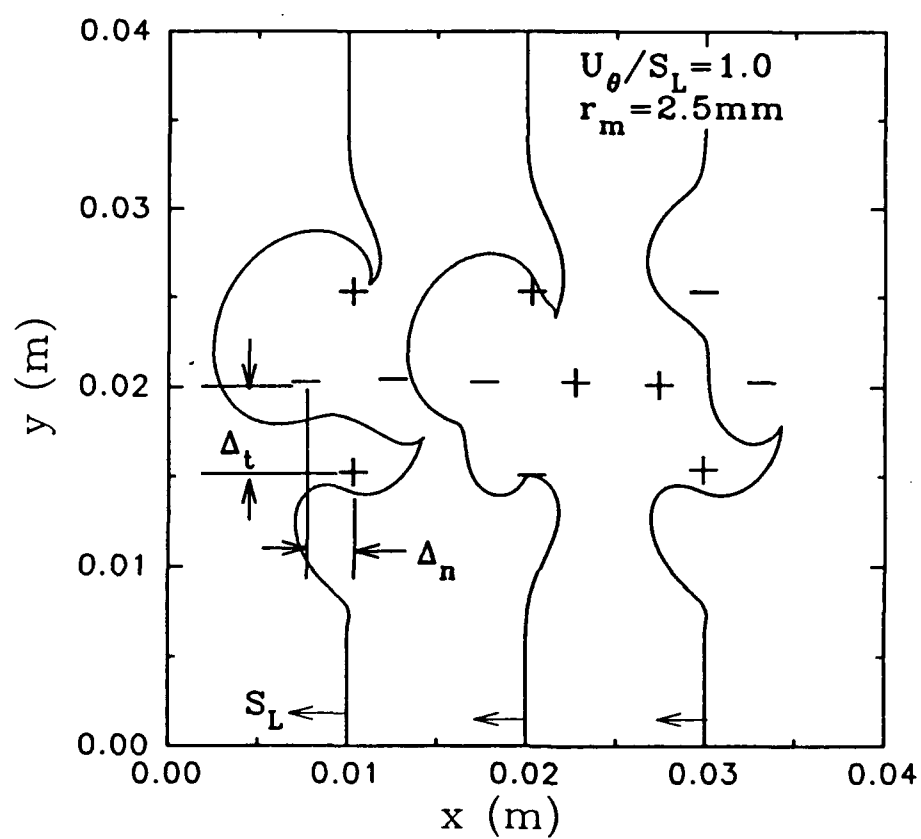
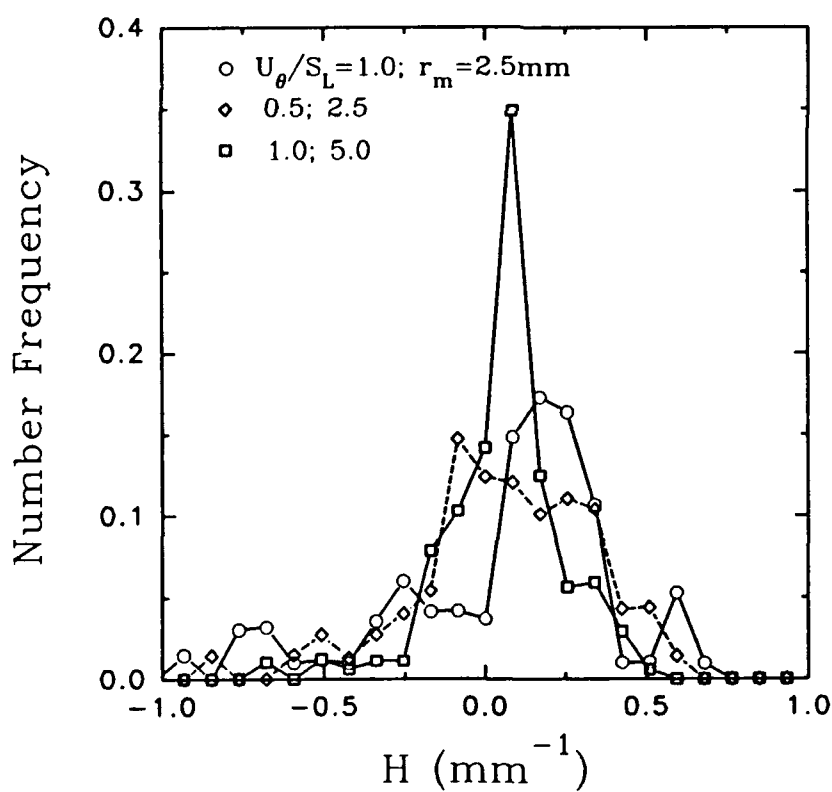
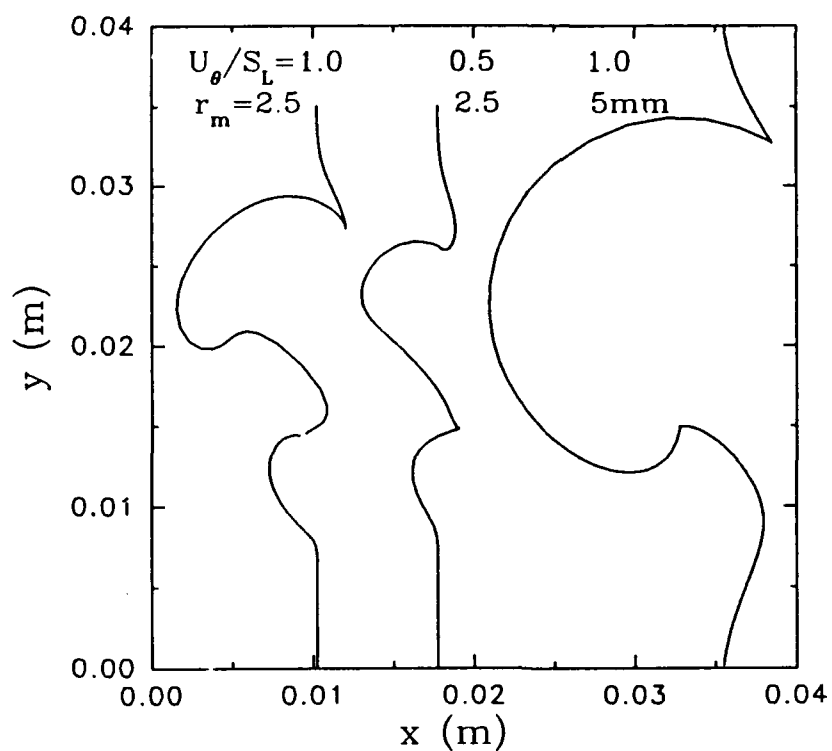


Figure 7. Flame contours caused by vortex arrays.



Figures 8 (a) and (b). Effects of the vortex velocity and size on (a) flame contours (top) and (b) flame curvature pdf's (bottom).

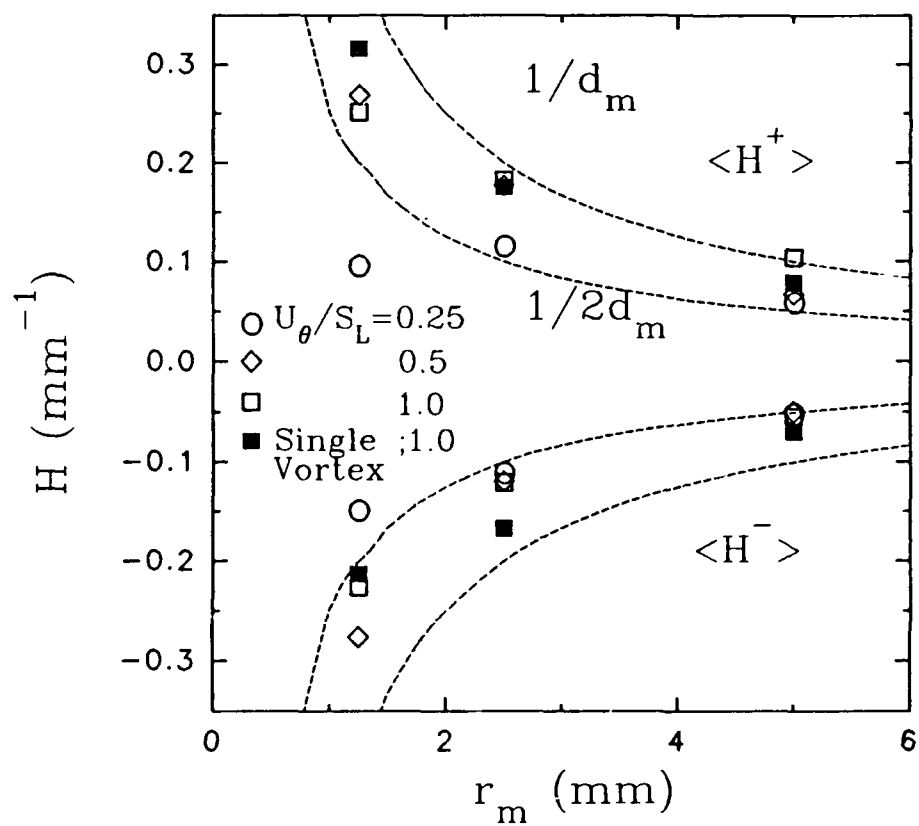
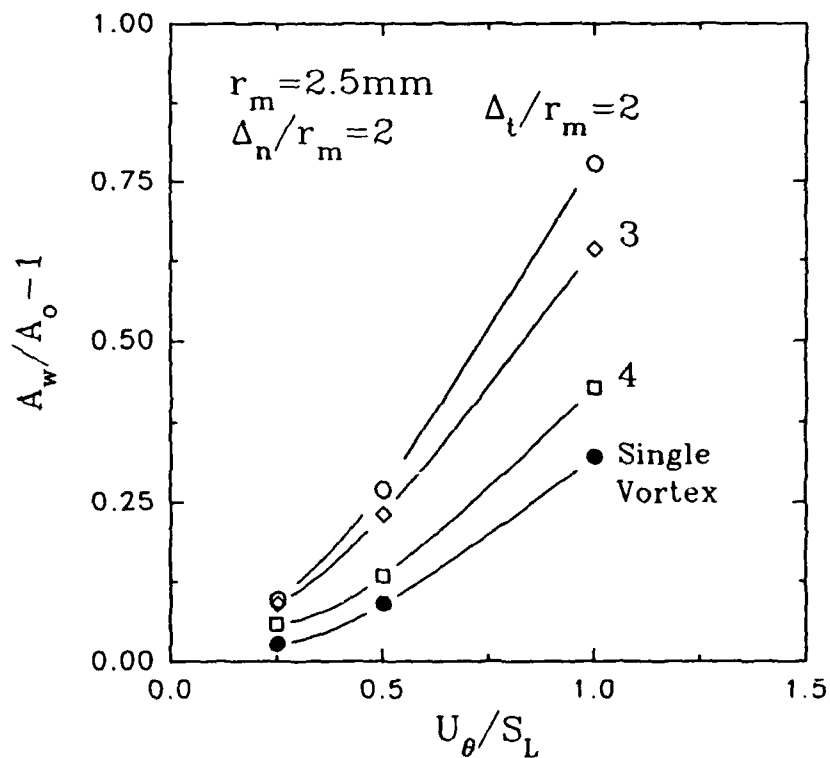
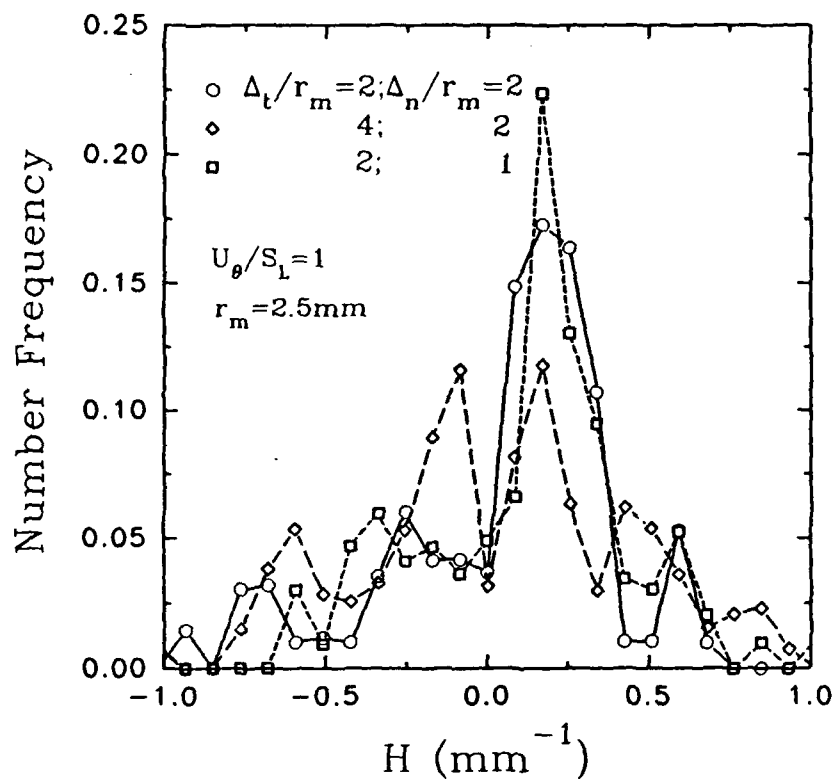


Figure 9. Dependence of mean flame curvatures on vortex radius.



Figures 10 (a) and (b). Effects of vortex spacings on (a) flame curvature pdf's (top) and (b) fractional flame area increase (bottom).

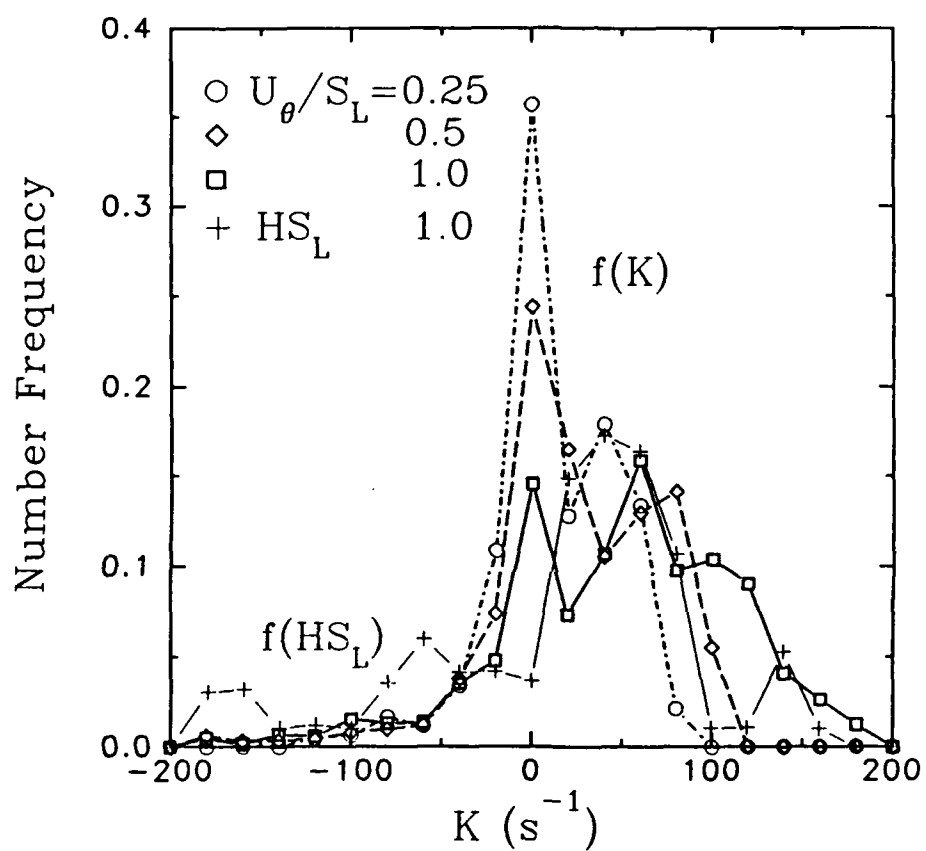


Figure 11. Flame stretch pdfs at various U_θ/S_L .

LOCAL RESPONSE AND SURFACE PROPERTIES OF PREMIXED FLAMES DURING INTERACTIONS WITH KÁRMÁN VORTEX STREETS

T.-W. Lee, J.G. Lee, D.A. Nye and D.A. Santavicca

Turbulent Combustion Laboratory
Department of Mechanical Engineering
Penn State University

Abstract- Premixed flames interacting with Kármán vortex streets have been experimentally investigated, in which local flame responses consistent with the results of stretched laminar flame theories are observed in that the OH LIF intensity increases when the local flame curvature becomes positive (negative) for thermodynamically unstable (stable) flames. Departure of the peak OH LIF intensity for hydrogen flames ranges from 20 to 150% of the value at zero flame curvature for flame curvature ranging from -1.5 to 0.7 mm^{-1} , while for propane/air flames the variation is within $\pm 20\%$ of the value at zero curvature. Thus, widely-used approximation of assigning constant local flame speed in turbulent premixed flames may be subject to significant errors for hydrogen flames for which the magnitude of $(1/Le-1)$ is relatively large, while for typical hydrocarbon flames this approximation appears to be more reasonable. Variation in the averaged peak OH LIF intensity is nearly linear with respect to the variation in flame curvature from -1.2 to 0.8 mm^{-1} , indicating that the application of the stretched laminar flame theory to turbulent premixed flames in which the local flame speed is a linear function of the flame stretch and Markstein length is reasonably accurate. The flame area during interactions with Kármán vortex streets increases as a relatively weak function of U_θ/S_L , while the vortex size affects the flame area increase in that smaller vortices are found to be less effective in generating flame area. The effect of Lewis number on the flame front is to enhance (suppress) the amplitude of the wrinkles generated by vortices for thermodynamically unstable (stable) flames, thus resulting in larger (smaller) flame area. The flame curvature pdf's for flames interacting with Kármán vortex streets exhibit a bias toward positive flame curvature due to the large area of positively-curved flame elements that develop downstream along the V-flame. A decrease in vortex size tends to increase the flame curvature and thus broaden the pdf's, while U_θ/S_L and Lewis number have relatively small effects on the flame curvature pdf's. The flame orientation distribution is peaked near the normal direction of flame propagation for small U_θ/S_L , while an increase in U_θ/S_L results in broadening of the flame orientation distribution and a shift toward larger flame angle due to the increased distortions in the flame front and increase in the effective flame propagation speed, respectively. An increase in the vortex size and decrease of Lewis number below unity for similar reasons result in broadening and shift of the flame orientation distributions although the effect is not as pronounced.

INTRODUCTION

Premixed flames in turbulent flow fields exhibit complex and unpredictable characteristics due to the multiplicity of vortex scales that simultaneously interact with the flame. A spectrum of vortex scales not only act to produce distortions in the flame front and to cause flame stretch, but the vorticity structures themselves are altered by the presence of the flame via thermal and baroclinic effects. In order to arrive at a fundamental understanding of turbulent premixed flames, flames interacting with organized vortex structures, such as a vortex ring, Kármán vortex streets, and an isolated single vortex, have been investigated in an attempt to isolate effects of a known vortex scale on the behavior of the premixed flames. Recent investigations following this approach include those of Poinso et al. [1], Roberts et al. [2] and Wu and Driscoll [3] in which premixed flames interacting with a vortex ring have been studied in order to identify various regimes of premixed combustion, e.g., wrinkled flamelet, multiply-connected or corrugated flamelet, and quenched flamelet regimes. Computational studies of premixed flames interacting with a single isolated vortex include that of Ashurst and McMurtry [4], where the changes in the vorticity structure arising from the flame-vortex interactions were investigated; of Rutland and Ferziger [5], who similarly identified the changes in the flow and flame structures as a function of the vortex strength; and of Lee and Santavica [6], in which the flame stretch characteristics for both single vortices and vortex arrays have been considered. References of earlier works on flame-vortex interaction can also be found in the above-mentioned articles.

For premixed flames, understanding of the changes in the vortex structure during flame-vortex interactions is important not only since the vortices cause the distortions in the flame front and corresponding increase in the flame surface area, but also due to the fact that the vorticity structure itself is altered during flame-vortex interactions via baroclinic vorticity generation and vorticity dissipation due to heat release effects. Also, quantitative descriptions of the flame surface properties, such as the flame surface area, flame curvature and orientation, are important elements in

understanding of turbulent premixed combustion. The flame surface area as a first approximation is proportional to the propagation speed of the wrinkled flame, while the flame curvature and orientation provide additional geometrical descriptions of the wrinkled flame surface. Furthermore, flame stretch arising from flow strain and flame curvature can cause local variations in the flame properties, such as the local flame speed and flame temperature. For sufficiently severe flame stretch, departure of the flame properties from unstrained values may be so large that the flames are locally quenched; in this regard, quantitative description of the local flame response to flame stretch is an additional element required in a complete analysis of turbulent premixed flames. Thus, it would be of interest to observe the variation in local flame properties in a dynamic situation as in flame-vortex interactions, in which unsteady flow strain and flame curvature are imposed on the flame similar to the processes involved in turbulent flames.

In view of this, the objective of the present investigation is to quantify the local response and the surface properties of premixed flames interacting with vortices within Kármán vortex streets. In the following, the experimental methodology will first be described, followed by the presentation of results concerning the local flame properties as observed by the changes in OH laser-induced fluorescence intensity as well as the surface properties including the flame surface area, flame curvature and orientation.

EXPERIMENTAL METHODS

Test Apparatus. The test apparatus consisted of a flow tube with 10 cm x 10 cm cross-section in which Kármán vortex streets generated from a cylindrical rod of various diameters were allowed to interact with a premixed V-flame, as shown in Figure 1. Premixed fuel/air mixtures entered through four ports at the bottom of the flow tube, and the vertically upward flow was laminarized through a sintered porous plate and a honeycomb flow straightener. The uniformity of the flow in the absence of the Kármán vortex street was verified using laser Doppler velocimetry, which showed that the

mean velocity was uniform within 1-2% while the velocity fluctuations were negligible (less than 3%). The flame was stabilized on a steel rod ($d = 1$ mm) positioned at the mid-section of the tube; while a vortex-generating rod was placed upstream at various positions with respect to the flame-holder. The variability in the position of the vortex-generating rod allowed additional control over the vortex parameters by adjusting the time that required for the vortices to arrive at the interaction region. As will be shown subsequently, the vortices become weaker and larger with increasing time through viscous dissipation. In this arrangement, the vortex streets interacted with one side of the V-flame as shown in Figure 1.

Diagnostics. OH planar laser-induced fluorescence (PLIF) was used for flame front demarcation and for the measurements of OH LIF intensity profiles along the flame front, while particle image velocimetry (PIV) was used to ascertain the vortex properties within the Kármán vortex streets. The OH PLIF setup involved an Nd:YAG laser which pumped a tunable pulsed dye laser at 532 nm with energy of ca. 300 mJ/pulse, while the tunable pulsed dye laser output after being frequency-doubled was ca. 5 mJ/pulse at 283.92 nm with approximately 10 ns pulse duration. A spherical-cylindrical lens combination was used to generate a beam sheet of 60 mm height and approximately 250 μ m thickness. The excitation of OH radicals involved tuning the laser beam to the $Q_2(8)$ and $Q_1(9)$ lines in the $(1,0)$ $A^2\Sigma^+ - X^2\Pi$ transition, while broadband detection of the vibrationally relaxed $(1,1)$ and $(0,0)$ fluorescence signal near 310 nm was used. Typically, a 50 mm x 50 mm field of view was employed using a uv-reflective camera lens ($f/1.1$) that focused the image onto a dual microchannel plate intensified Reticon (EG&G) camera. The synchronization between the laser pulse and intensified camera gate (1 μ s duration) was accomplished through a custom-made electronic circuit. Nonuniformity in the laser intensity across the beam sheet was normalized by a unique method of reading the maximum OH LIF intensity on the undisturbed side of the premixed V-flame and dividing by this value all the observed signal intensity along that particular horizontal line. Tests with undisturbed laminar premixed flames showed excellent normalization characteristics with uniform OH

LIF intensity along the flame front.

Particle image velocimetry was used to verify the analytical method used to determine the vortex properties. Two Nd:YAG lasers were used to generate spatially overlapping beam sheets with an adjustable temporal separation of 100 μ s to 10 ms. The resulting pairs of Mie-scattered signals from the seeded titanium dioxide particles were captured using a conventional 35 mm reflex camera (Nikon 8008) with Nikor microlens at 1:1 magnification. The photographic slides thus obtained were analyzed via a digital imaging system employing a CCD camera and a traversing mechanism to automatically shift the slide position. Spatial Fourier transforms were then performed in order to locate peaks in the correlations of the paired Mie-scattering signals from which the vortex velocity field could be constructed. A full description of the PIV system can be found in Nye and Santavicca [7]. A conventional dual-beam backscatter laser Doppler velocimetry was also employed in order to check the uniformity of the flow within the test section as mentioned above and also in the determination of the laminar flame speeds.

Kármán Vortex Street and Test Conditions Kármán vortex streets consist of two nearly parallel rows of alternating vortices, the strength and size of which depend on the Reynolds number of the flow based on the mean flow velocity and the vortex-generating rod diameter and also on the transit time that the vortices take in arriving at the interaction regions. For Reynolds number between 40 and 150, the vortex streets are laminar and stable vortices with well-defined characteristics within the vortex streets are observed [8]. The vortex parameters such as the vortex rotational velocity, vortex diameter, longitudinal and lateral vortex spacings can be determined by methods following Roshko [8] and Schaefer and Eskinazi [9]. Each of the vortices in the street is considered to behave like a single vortex filament with the rotational velocity of the vortex being described by:

$$u_{\theta} = \Gamma / (2\pi r) (1 - \exp(-r^2/4\nu t)) \quad (1),$$

where Γ and r are the circulation and the radial distance from the vortex center, respectively. Time, t , is the transit time that the vortices take in arriving at the interaction zone at the flame, while ν is the viscosity. Differentiating, the maximum rotational velocity of $U_\theta = 0.72\Gamma/2\pi r_m$ occurs at $r_m = 2.24(\nu t)^{1/2}$. U_θ divided by the laminar flame speed, S_L , and $\delta_v = 2r_m$ normalized by the laminar flame thickness, δ_L , are used as the characteristic vortex velocity and vortex size, respectively. The circulation, Γ , is estimated from $0.343U_0d/St$ following Schaefer and Eskinazi [9]; while the Strouhal number, St , is obtained from the experimental correlations of Roshko [8]. The longitudinal spacing can be obtained from the Strouhal number, since it gives the nondimensional shedding frequency of the vortices that can be converted to spatial frequency using the mean flow velocity; while the lateral spacing is related to the vortex size [8,9]. The vortex parameters obtained in this manner have been verified using PIV for selected conditions as shown in Table I, which shows that there is reasonably good agreement between the data and the vortex velocities and diameters determined using the above method; thus the above method was used to determine the test conditions as listed in Table II.

The test conditions have been selected in order first to examine the effects of Lewis number and secondly to study the effect of the vortex velocity and size on the behavior of the wrinkled premixed flames. A variation in Lewis number from 0.21 to 1.79 has been obtained using hydrogen/helium/air, methane/air, and propane/air flames, as shown in Table II. The addition of helium as a diluent was necessary for hydrogen flames in order to sufficiently slow the flame speed so that the parameter U_θ/S_L could be set equal to the values for the methane/air and propane/air flames, as shown in Table II. The laminar flame speeds for methane/air and propane/air flames were obtained from results of Egolfopoulos et al.[10], while for the hydrogen/helium/air flames it was necessary to determine the flame speed using the present V-flame setup by measuring the component of the flow velocity normal to the tilted flame. The flame thickness has been estimated using $\delta_L = 4.6\alpha/S_L$ where α is the thermal diffusivity, which yielded typical values near 1 mm. The remainder of the test conditions in which U_θ/S_L and δ_v/δ_L were independently varied are listed in Table II.

RESULTS AND DISCUSSION

Figures 2-4 show typical binarized OH PLIF images of the premixed V-flames wrinkled by the Kármán vortex streets. Figures 2 (a)-(c) and 3 (a)-(c) correspond to methane/air flames for which the vortex rotational velocity (U_θ/S_L) and vortex size (δ_v/δ_L) have been varied, respectively; while Figures 4 (a)-(c) show the effect of Lewis number on the flame front wrinkle structures. All of the images in Figures 2-4 exhibit the typical dynamics of flame fronts wrinkled by vortices: The parallel alternating vortices in the Kármán vortex street create a velocity defect in the middle of the street; and as these alternating vortices interact with the flame front, this velocity defect causes the protruding feature (convex toward the reactant) on the flame front, while the excess velocity adjacent to this region pushes the flame back to create a concave (toward the reactant) feature. Due to the vertically upward mean flow velocity, the flame front wrinkles thus created are convected along the V-flame; and the wrinkles further develop into features which involve an increase in the positively-curved (convex toward the reactant) flame element areas due to normal flame propagation, while the negatively-curved flame elements propagate toward one another to form cusps as observed in the upper parts of the images in Figures 2-4. Thus, cusp formation involves a kinematical process in which normal flame propagation causes adjacent concave flame elements to collide when the wrinkles initially created by the vortices are allowed to develop in space and time. Figures 2 and 3 also show the effect of both the vortex velocity and vortex size in increasing the degree of flame front wrinkling when these vortex parameters are increased, as will be quantified subsequently. The effect of Lewis number on the flame structure is exhibited in Figures 4 (a)-(c), which correspond to images of the hydrogen/helium/air, methane/air, and propane/air flames, respectively, with Lewis numbers of 0.21, 0.94 and 1.79. For thermodynamically unstable ($Le < 1$) hydrogen/helium/air flames, the concave (convex) flame elements are subject to reduced (enhanced) flame speeds due to the differential rates at which thermal energy and the deficient reactant diffuse to the surrounding, which leads to the amplification of the flame front wrinkles initially created by the vortices for $Le < 1$. This effect is

clearly evidenced in Figure 4 (a), where there is a significant penetration into the concave region on the flame front in the upper part of the image. In contrast, a comparison of Figures 4(b) and (c) shows that there is a substantial suppression of the flame front wrinkles for propane/air flames ($Le=1.79$) in Figure 4 (c), where the amplitude of the wrinkles is very weak compared to methane/air flames.

Figures 5 (a)-(c) are typical contour plots showing the spatial distribution of the OH LIF intensities normalized by the maximum observed intensity for hydrogen/helium/air, methane/air, and propane/air flames, respectively; while the vortex properties are kept nearly constant at $U_\theta/S_L = 0.8$ and $\delta_\nu/\delta_L = 2.7-4.2$. Each line in Figures 5 (a)-(c) thus represents a constant OH LIF intensity, where the intensity scale is ranged from 0 to 100. OH LIF intensities from 3600 (60 x 60) pixels are plotted with second-order interpolation between the pixels to generate continuous contour lines. In all of the contour plots, the preheat zone is distinguished by steep gradients in the OH LIF intensities, as shown by the dense and parallel iso-intensity lines along the flame front. In the post flame regions, the OH LIF intensity gradually decreases to equilibrium levels. A very weak OH LIF intensity is observed at the cusped region in Figure 5 (a) where the flame thickness has also been significantly increased, distinguishable by the large distance between iso-intensity lines; while relatively high OH LIF intensity is associated with positively-curved regions. A decrease in the OH LIF intensity and broadening of the flame thickness indicates a decrease in local reaction rate and thus lower flame speed; and this effect is pronounced at cusps where the most severe negative flame stretch typically is imposed on the flame front [6]. This is consistent with the results of the stretched laminar flame theory [11] in which the combined effects of non-unity Lewis number and flame stretch lead to variations in flame properties. Although both flow strain and flame curvature contribute to total flame stretch in premixed flames, in cusped regions the severe negative flame curvature usually dominates, resulting in significant negative flame stretch [6]. The significant negative flame stretch when combined with less-than-one Lewis number causes the OH LIF intensity to decrease as shown

in Figure 5 (a). In contrast, methane/air flames in Figure 5 (b) with Lewis number of 0.94 exhibit relatively uniform OH LIF intensities along the flame front since the departure of the Lewis number from unity is minimal. Figure 5 (c) is the corresponding contour plot for propane/air flames that shows suppressed amplitudes in the flame front wrinkles similar to Figure 4 (c) and relatively small variations in the OH LIF intensities.

The local behavior of the premixed flames wrinkled by vortices can be examined in a more quantitative manner by plotting the OH LIF intensity profiles normal to the flame front and grouping them according to the sign of the flame curvature that they are subject to, as shown in Figures 6 (a)-(c); i.e., different symbols are used to represent OH LIF intensity profiles at positive local flame curvatures ($0.1\text{mm}^{-1} < H < 1.0\text{mm}^{-1}$), nearly zero curvatures ($-0.1\text{mm}^{-1} < H < 0.1\text{mm}^{-1}$), and negative curvatures ($-1.5\text{mm}^{-1} < H < -0.1\text{mm}^{-1}$). Positive flame curvature corresponds to convexity toward the reactant. It can be seen that for thermodynamically unstable hydrogen/helium/air flames there is a large spread in the extent of the OH LIF intensity profiles, indicating that the local response of the flame is very sensitive to the flame curvature. For example, the observed peaks in the OH LIF intensity for positive local flame curvatures exceed corresponding peaks at zero flame curvature by up to 50%; i.e., the local reaction rate and thus OH concentration and flame speed are enhanced due to the positive flame stretch associated with the positive flame curvature. In contrast, there are dramatic dropoffs in peak OH LIF intensity for negative flame curvatures; and in some cases, the gradients in the OH LIF intensity profiles have become so small as to suggest incipient flame quenching. These substantial dropoffs in OH LIF intensity in most cases occur at cusp points which, as indicated earlier, are associated with severe negative flame stretch. The spread in the OH LIF intensity profiles for $H \approx 0$ may be, to some extent, due to the variations in flame curvatures sampled; i.e. since exactly zero curvatures are seldom observed experimentally, $H \approx 0$ corresponds to the flame curvature between $\pm 0.1\text{mm}^{-1}$ as noted above. Also, there are additional variations in the local flame stretch caused by different flow strain rates that can cause such variations in OH LIF

intensity profiles. For methane/air flames with Lewis number close to one, there are only minimal variations in the OH LIF intensity profiles for a similar range of flame curvatures, verifying that it is the combined effect of flame stretch and non-unity Lewis number that affects the local flame properties in premixed flames. As expected, the local behavior of propane/air flames ($Le > 1$) is reversed in comparison to hydrogen flames ($Le < 1$) in that OH LIF intensity is increased for negative flame curvatures, as shown in Figure 6 (c). Furthermore, at this condition the spread in the OH LIF intensity profiles is not as pronounced as in the hydrogen flames, which implies reduced sensitivity of the propane/air flames to flame stretch or flame curvature. The parameter, $(1/Le-1)$, that determines the sensitivity of local flame properties to flame stretch [11] varies from -0.44 for propane/air flames to 3.76 for hydrogen flames; thus not only the absolute value of $(1/Le-1)$ for propane/air flames is smaller than for hydrogen flames but also the sign of $(1/Le-1)$ is opposite of hydrogen flames, consistent with the observation that the local response of propane/air flames is less sensitive and reversed from that of hydrogen flames. The peak OH LIF intensity variation for hydrogen flames in Figure 6 (a) is from 20 to 150 % of the value at zero flame curvature, indicating that the approximation of assigning a constant local flame speed to turbulent premixed flames is likely to lead to substantial errors since the flame stretch distribution in turbulent flow field is expected to be biased toward positive values due to the predominant positive flow strain rates [12]. The variations in peak OH LIF intensity for methane/air flames is minimal while for propane/air flames the changes are ± 20 %; thus the assumption of constant local flame speed may yield reasonably accurate results for typical hydrocarbon flames. In most instances, the steepest gradients in the OH LIF intensities are confined to a region of approximately 1 mm in thickness in agreement with the flame thickness calculated by $\delta_L = 4.6\alpha/S_L$, except in instances where the OH LIF intensity has dropped to anomalously low values in Figure 6 (a).

From these OH LIF intensity profiles, correlations between the peak OH LIF intensity and the local flame curvature can be obtained by averaging over many samples for fixed flame curvature,

the rest of which is plotted in Figure 7. Since the frequency of occurrence for moderate flame curvatures is substantially higher than for extreme flame curvatures (see Figures 10 (a)-(c)), the number of samples averaged for $-0.25\text{mm}^{-1} < H < 0.5\text{mm}^{-1}$ is 40-200, while for flame curvatures outside this range the number of samples is typically less than ten. The effect of averaging over many samples is to cancel out the effects of flow strain, or in the least average over the fluctuations in the flow strain, so that the effect of the flame curvature on the peak OH LIF intensity is recovered. Strained laminar premixed flame calculations show that the peak OH concentration can be used as a measure of the level of chemical activity of the flame since it is observed to depend monotonically on the strain rate [13]. Thus, by using a relatively temperature-insensitive excitation scheme for OH LIF as done in the present study, the observed peak OH LIF intensity can be used to compare the local reaction rate and corresponding flame speeds. It can be observed in Figure 7 that for thermodynamically unstable hydrogen/helium/air flames the slope of the correlation between peak OH LIF intensity and flame curvature is positive. For methane/air flames, the peak OH LIF intensity is relatively insensitive to variations in flame curvature showing only a very weak positive slope since the departure of the Lewis number from unity is minimal. A negative slope in the correlation is observed for propane/air flames, indicating a stabilizing response of the flames with respect to the variation in flame curvature; i.e., the flame speed is enhanced (reduced) for concave (convex) flame elements leading to suppression of flame wrinkles as shown in earlier flame front images. For all mixtures, the relationship between the peak OH LIF intensity and the flame curvature is nearly linear for curvature varying from approximately -1.5mm^{-1} to 1.0mm^{-1} , which converts to flame stretch of -340s^{-1} to 230s^{-1} when multiplied by the average flame speed of 0.23m/s . Thus, for turbulent flames for which the flame stretch is expected to be within this range a linear relationship between the laminar flame speed and flame stretch may be applied with reasonable accuracy. It is also interesting to note that the negative slope of the correlation of the peak OH LIF intensity with local flame curvature for propane/air flames is much smaller in magnitude than the positive slope for the

hydrogen/helium/air flames, indicating a variation in the response of the premixed flames that depends on the parameter $1/Le-1$ as discussed earlier.

Next, the surface properties of premixed flames wrinkled by vortices are considered, including the effects of vortex velocity, vortex size and Lewis number on flame area increase, flame curvature and orientation statistics. Figure 8 shows the variations of the flame area for methane/air flames as a function of the vortex rotational velocity for various vortex sizes. It can be observed that the flame area increase is a relatively weak function of U_θ/S_L for the present configuration. For flames wrinkled by Kármán vortex streets, the vortices interact with the flame in a region where the vortex street intersects with the V-flame, while the wrinkles created in this region convect away along the V-flame due to the mean flow velocity and further develop their structures via normal flame propagation. Thus, in this type of flame-vortex interactions flame area is produced both through direct interaction with the vortices and via normal flame propagation of positively curved flame elements; and since the contribution to total flame area by normal flame propagation is nearly independent of the vortex velocity, this explains the continuous decrease of the slope in the dependence of flame area on U_θ/S_L in Figure 8. This process is comparable to weakly turbulent flames in which weak vortices sparsely distributed in space wrinkle the flame front and the flame front wrinkles thus created subsequently develop large areas of positively-curved flame elements terminated by cusps; thus flame area increases both as a direct consequence of vortex action and normal flame propagation. In Figure 8, vortex size plays an important role in the functional relationship between flame area and U_θ/S_L , as these curves are shifted toward larger U_θ/S_L for smaller vortices. Thus, for smaller vortices it takes a larger value of U_θ/S_L in order to generate the same level of flame areas, indicating that the smaller vortices are less effective in wrinkling the flame fronts. Other results concerning the effect of vortex size on the flame front wrinkling include those of Poinso et al. [1], Roberts et al. [2], and Rutland and Ferziger [5]. While the first two studies conclude that smaller vortices are less effective in wrinkling the flame front due to curvature and viscous effects, Rutland

and Ferziger assert that the vortex size for a single isolated vortex interacting with the flame has a negligible effect on the flame area. For a single vortex case, as in Rutland and Ferziger, the undisturbed flame area used as the reference area about which the wrinkled flame area is measured needs to be adjusted depending on the extent of the flame-vortex interaction, i.e., on the vortex size itself; while in the present case, the reference area remains fixed as the undisturbed V-flame area within the field of view. If the vortices within the Kármán vortex street are smaller, then the extent of the interaction is also reduced. Furthermore, the scale of the wrinkles developing further downstream is decreased for smaller vortices; thus, this leads to smaller flame area increase when the vortex size is decreased for a fixed reference flame area in the present configuration.

Figure 9 shows the effect of Lewis number on the flame area as the Lewis number is varied from 0.21 to 1.79 for nearly constant $U_\theta/S_L=0.8$ and $\delta_v/\delta_L=2.7-4.2$. The parameter δ_v/δ_L could not be kept at a fixed value due to the differences in the flame thickness while the vortex diameter (δ_v) itself was nearly constant as shown in Table II. However, the variation in δ_v/δ_L is relatively small and there is actually an increase in the flame area when the mixture is thermodiffusively unstable in spite of the slight decrease in δ_v/δ_L . Thus, a strong effect of the Lewis number is observed by a 20% increase in flame area when the Lewis number is varied from 1.79 to 0.21 in Figure 9. This increase in the flame area is primarily due to the increase in amplitude of the wrinkles when the local flame speed of convex (concave) regions is increased (decreased) as shown earlier in Figures 4 (a)-(c). Similar increases in flame area when the mixture becomes thermodiffusively unstable ($Le < 1$) have been observed for turbulent premixed flames [14-16].

Figures 10 (a)-(c) contain plots of the area-weighted flame curvature probability density functions (pdf's) at various U_θ/S_L , δ_v/δ_L , and Lewis numbers, respectively. In all instances, the pdf's are biased toward positive curvature reflecting the large convex (toward the reactant) flame areas generated as the wrinkles are convected downstream, while the cusps are represented by large negative curvatures ($H \approx -1.0\text{mm}^{-1}$) with very low number frequency due to the negligible area that

they occupy. The effect of U_θ/S_L on the flame curvature pdf's is found to be very weak. The increase in flame curvature observed for turbulent premixed flames with increasing turbulence Reynolds numbers [17] can be attributed to the decrease in the length scale of turbulence; for example the mean flame radius of curvature has been found to follow the Taylor scale of the turbulent flow field [17]. Furthermore, a computational study from this laboratory [6] showed that flame curvature is more strongly dependent on the vortex size than on the vortex velocity. Thus, for these reasons the flame curvature pdf's exhibit minimal change with respect to the variations in U_θ/S_L , while there is an increase in the flame curvature and a corresponding broadening of the flame curvature pdf's when the vortex size is decreased; although this effect is somewhat damped due to the fact that in area-weighted statistics the large areas of positively-curved flame elements that develop downstream on the V-flames (see Figures 2-4) dominate the pdf's. In spite of the changes in flame structure and a substantial increase in the flame area with respect to the Lewis number variations shown earlier, the flame curvature pdf's exhibit relatively minor changes. This is due to the same effect of the large areas of positively-curved flame elements dominating the pdf's and also because of the fact that when the instability mechanism increases the amplitude of the flame front wrinkles both large flame curvatures at the trough and crest of the flame front wrinkles as well as weak curvatures in between are produced; thus the effect of Lewis number on area-weighted flame curvature pdf's is minimal in spite of the increase in flame area. Similar results for turbulent premixed flames in which the flame curvature pdf's undergo relatively small changes with respect to variations in Lewis number have been observed by Haworth and Poinso [12], Goix and Shepherd [15] and Lee et al. [16].

The distributions of the flame orientation angle measured with respect to the direction of propagation of the undisturbed flame are shown in Figures 11 (a)-(c). It can be observed in Figure 11 (a) that for weak vortices (small U_θ/S_L) the flame orientation distributions are peaked around the normal direction of flame propagation, while with stronger vortices the flame orientation distribution

becomes wider as the increase in flame front wrinkling causes the flame to be oriented at random angles with respect to the normal direction of flame propagation. There is also a slight shift toward positive flame orientation angles due to the fact that the flame front wrinkling increases the effective propagation speed of the flames and thus the overall flame angle becomes larger. The effects of vortex size and Lewis number on the flame orientation are relatively weak, although a slight positive shift and broadening in the flame orientation distribution are observed as the vortex size is increased while the decrease in the Lewis number causes a broadening in the distribution.

CONCLUSIONS

From the discussion above, we make following conclusions concerning the local response and surface properties of premixed flames interacting with Kármán vortex streets:

- (1) Local flame properties during interactions with vortices exhibit responses consistent with the results of stretched laminar flame theories [11] in that the OH LIF intensity increases when the local flame curvature becomes positive (negative) for thermodynamically unstable (stable) flames.
- (2) Departure of the peak OH LIF intensity for hydrogen flames ranges from 20 to 150% of the value for unstretched flames (zero flame curvature) for flame curvature ranging from -1.5 to 0.7 mm^{-1} , while for propane/air flames the variation is within $\pm 20\%$ of the value at zero curvature. Thus, the widely-used approximation of assigning constant local flame speed in turbulent premixed flames may be subject to significant errors for hydrogen flames for which the magnitude of $(1/Le-1)$ is relatively large, while for typical hydrocarbon flames this approximation appears to be more reasonable.
- (3) The variation in the averaged peak OH LIF intensity is nearly linear with respect to the variation in flame curvature from -1.2 to 0.8 mm^{-1} , indicating that the application of the stretched laminar flame theory to turbulent premixed flames in which the local flame speed is a linear function of the flame stretch and Markstein length is reasonably accurate.
- (4) The flame area during interactions with Kármán vortex streets increases as a relatively weak

function of U_θ/S_L , while the vortex size affects the flame area increase in that smaller vortices are less effective in generating flame area. The effect of Lewis number on the flame front is to enhance (suppress) the amplitude of the wrinkles generated by vortices for thermodynamically unstable (stable) flames, thus resulting in larger (smaller) flame area.

(5) The flame curvature pdf's for flames interacting with Kármán vortex streets exhibit a bias toward positive flame curvature due to the large area of positively-curved flame elements that develop downstream along the V-flame. A decrease in vortex size tends to increase the flame curvature and thus broaden the pdf's, while U_θ/S_L and Lewis number have relatively small effects on the flame curvature pdf's.

(6) The flame orientation distribution is peaked near the normal direction of flame propagation for small U_θ/S_L , while an increase in U_θ/S_L results in broadening of the flame orientation distribution and a shift toward larger flame angle due to the increased distortions in the flame front and increases in the effective flame propagation speed, respectively. An increase in the vortex size and decrease of Lewis number below unity for similar reasons results in broadening and a shift of the flame orientation distributions although the effect is not as pronounced.

ACKNOWLEDGEMENTS

The financial support for this research provided by the Air Force Office of Scientific Research under Grant AROSR-90-0005 through Dr. Julian Tishkoff, program manager, is gratefully acknowledged.

REFERENCES

1. Poinso, T., Veynante, D. and Candel, S., J. Fluid Mech. 228:561 (1991).
2. Roberts, W. L., Driscoll, J. F., Drake, M. C. and Ratcliffe, J. W., Twenty-Fourth Symposium (International) on Combustion, in press.

3. Wu, M.-S. and Driscoll, J. F., Combust. Flame, to appear.
4. Ashurst, W. T. and McMurtry, P. A., Combust. Sci. Tech. 66:17 (1989).
5. Rutland, C. J. and Ferziger, J. H., Combust. Flame, 84:343 (1991).
6. Lee, T.-W. and Santavica, D. A., Combust. Sci. Tech., to appear.
7. Nye, D. A. and Santavica, D. A., Experiments in Fluids, submitted.
8. Roshko, A., NACA Technical Note 2913, 1953.
9. Schaefer, J. W. and Eskinazi, S., J. Fluid Mech. 6:16 (1959).
10. Egolfopoulos, F. N., Zhu, D. L. and Law, C. K., Twenty-Third Symposium (International) on Combustion, The Combustion Institute, Pittsburgh, p. 471, 1990.
11. Law, C. K., Twenty-Second Symposium (International) on Combustion, The Combustion Institute, Pittsburgh, p. 1381, 1988.
12. Haworth, D. C. and Poinot, T. J., Combust. Sci. Tech., to appear.
13. Becker, H., Monkhouse, P. B., Wolfrum, J., Cant, R. S., Bray, K. N. C., Maly, R., Pfister, W., Stahl, G., Warnatz, J., Twenty-Third Symposium (International) on Combustion, The Combustion Institute, Pittsburgh, p. 817, 1990.
14. Wu, M.-S., Kwon, S., Driscoll, J. F. and Faeth, G. M., Combust. Sci. Tech. 73:327 (1990).
15. Goix, P. J. and Shepherd, I. G., Combust. Sci. Tech., to appear.
16. Lee, T.-W., North, G. L. and Santavica, D. A., Combust. Flame, submitted.
17. Lee, T.-W., North, G. L. and Santavica, D. A., Combust. Sci. Tech. 84:121 (1992).

LIST OF TABLES

Table I. Comparison of measured and estimated vortex properties.

Table II. Test Conditions.

FIGURE CAPTIONS

Figure 1. Schematic of the experimental apparatus.

Figures 2 (a)-(c). Binarized images of flame fronts at $Le=0.94$, $\delta_v/\delta_L=5.2$ and (a) $U_\theta/S_L=0.4$; (b) 0.6; (c) 0.7.

Figures 3 (a)-(c). Binarized images of flame fronts at $Le=0.94$, $U_\theta/S_L=0.7$ and (a) $\delta_v/\delta_L=3.4$; (b) 3.8; (c) 5.3.

Figures 4 (a)-(c). Binarized images of flame fronts at $U_\theta/S_L=0.8$, $\delta_v/\delta_L=2.8-4.2$ and (a) $Le=0.21$; (b) 0.94; (c) 1.79.

Figure 5 (a). Contour plot of OH LIF intensity for $H_2/He/air$ flame ($Le=0.21$).

Figure 5 (b). Contour plot of OH LIF intensity for CH_4/air flame ($Le=0.94$).

Figure 5 (c). Contour plot of OH LIF intensity for C_3H_8/air flame ($Le=1.79$).

Figures 6 (a)-(c). OH LIF intensity profiles normal to the flame for (a) $Le=0.21$; (b) 0.94; (c) 1.79.

Figure 7. Averaged peak OH LIF intensity as a function of local flame curvature at various Lewis numbers.

Figure 8. Flame area increase as a function of U_θ/S_L .

Figure 9. Effect of Lewis number on flame area.

Figure 10. Flame curvature pdf's at various (a) U_θ/S_L ; (b) δ_v/δ_L ; (c) Le .

Figure 11. Flame orientation distribution at various (a) U_θ/S_L ; (b) δ_v/δ_L ; (c) Le .

Table I. Comparison of measured and estimated vortex properties.

U_0^a (m/s)	d^b (mm)	Re_d	U_θ/U_0 (Measured)	δ_v/d	U_θ/U_0 (Estimated)	δ_v/d
0.6	1.5	60	0.18	2.3	0.20	3.0
0.6	2.0	80	0.24	2.4	0.22	2.3
0.6	3.0	120	0.28	1.5	0.29	1.5
0.7	1.5	70	0.23	2.2	0.19	2.8
0.7	2	93	0.22	2.0	0.23	2.1
0.9	1	67	0.15	5.0	0.15	3.6
0.9	1.5	91	0.18	2.3	0.20	2.4
0.9	2	121	0.20	3.5	0.24	1.8
1.1	1.5	113	0.15	1.9	0.21	2.2

^aMean flow velocity; ^bDiameter of the vortex generating rod.

Table II. Test conditions.

U_0 (m/s)	d (mm)	Re_d	ϕ	S_L (m/s)	δ_L (mm)	U_θ/S_L	δ_v/δ_L	a^2/δ_L	h^b/a	Δy^c (mm)
Hydrogen/Helium/Air ($Le=0.21$):										
0.65	2.0	70	0.09 ^d	0.18	1.6	0.84	2.8	7.5	0.40	25
Methane/Air ($Le=0.94$):										
0.80	2.0	70	0.74	0.23	1.0	0.84	4.0	11.0	0.41	25
Propane/Air ($Le=1.79$):										
0.87	2.0	87	0.74	0.27	0.9	0.82	4.2	12.0	0.42	25
Methane/Air:										
0.63	1.0	47	0.71	0.21	1.1	0.39	5.2	8.3	0.53	50
0.63	1.5	64	0.71	0.21	1.1	0.44	5.2	9.3	0.55	50
0.63	2.0	92	0.71	0.21	1.1	0.55	5.2	11.6	0.51	50
0.63	3.0	133	0.71	0.21	1.1	0.72	5.2	15.0	0.46	50
0.78	1.0	58	0.73	0.23	1.0	0.57	3.8	7.6	0.46	25
0.78	1.5	79	0.73	0.23	1.0	0.67	3.8	9.0	0.44	25
0.78	2.0	114	0.73	0.23	1.0	0.85	3.9	11.1	0.41	25
0.78	3.0	130	0.73	0.23	1.0	0.93	3.9	12.1	0.40	25
0.93	1.0	68	0.75	0.24	1.0	0.75	3.1	7.2	0.40	12.5
0.93	1.5	94	0.75	0.24	1.0	0.95	3.1	8.5	0.39	12.5
0.93	2.0	135	0.75	0.24	1.0	1.16	3.2	10.6	0.35	12.5
0.63	1.5	64	0.71	0.21	1.1	0.68	3.4	8.9	0.34	12.5
0.78	1.5	79	0.73	0.23	1.0	0.67	3.8	9.0	0.44	25
0.63	3.0	133	0.71	0.24	1.0	0.72	5.2	15.0	0.46	50

^aLongitudinal vortex spacing; ^bLateral vortex spacing; ^cDistance between vortex rod and flame rod; ^d $V(H_2)/V(H_2+He+Air)=0.09$, $V(He)/V(He+Air)=0.43$.

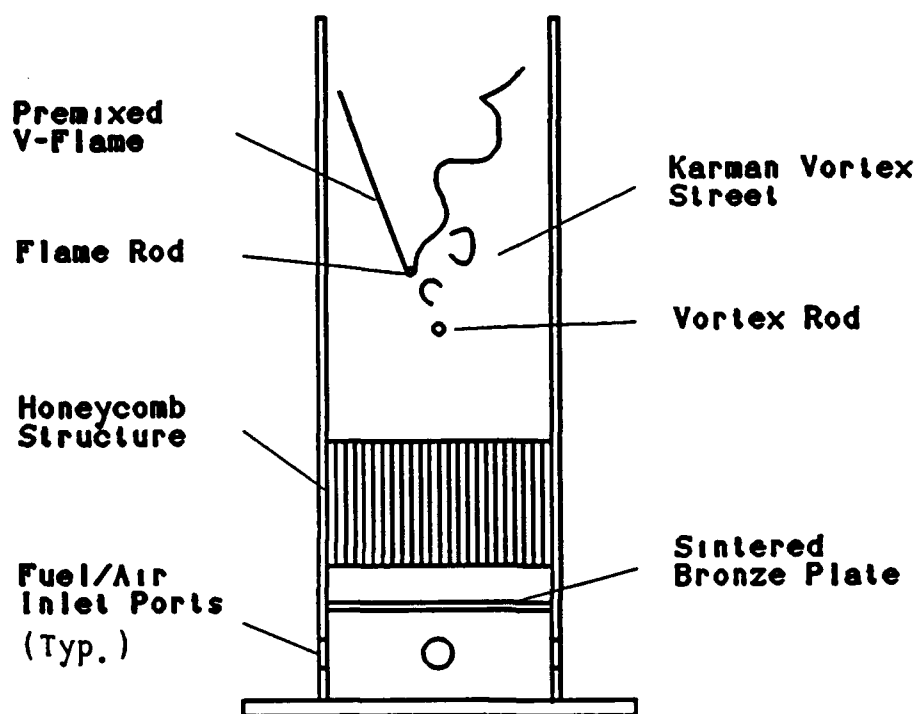
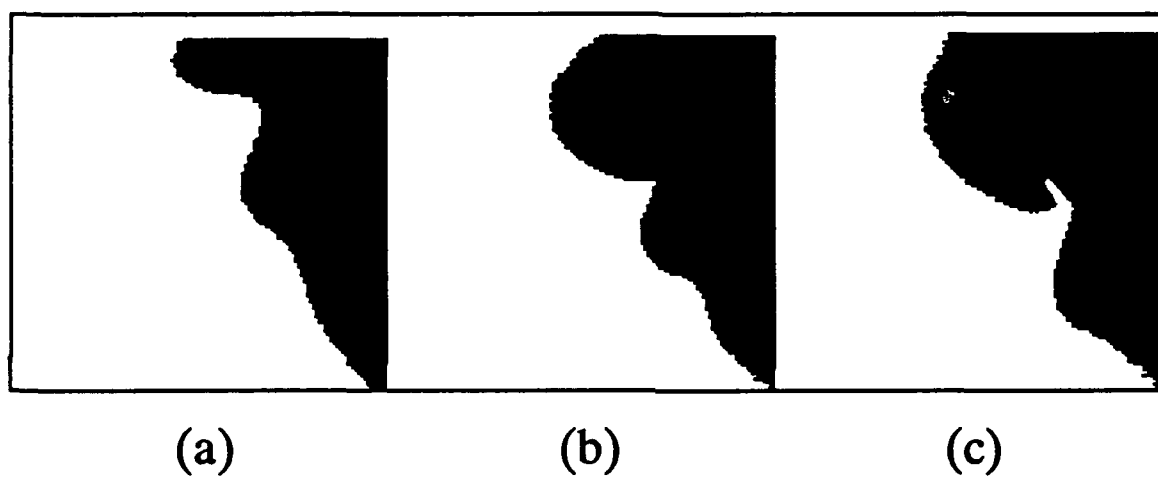
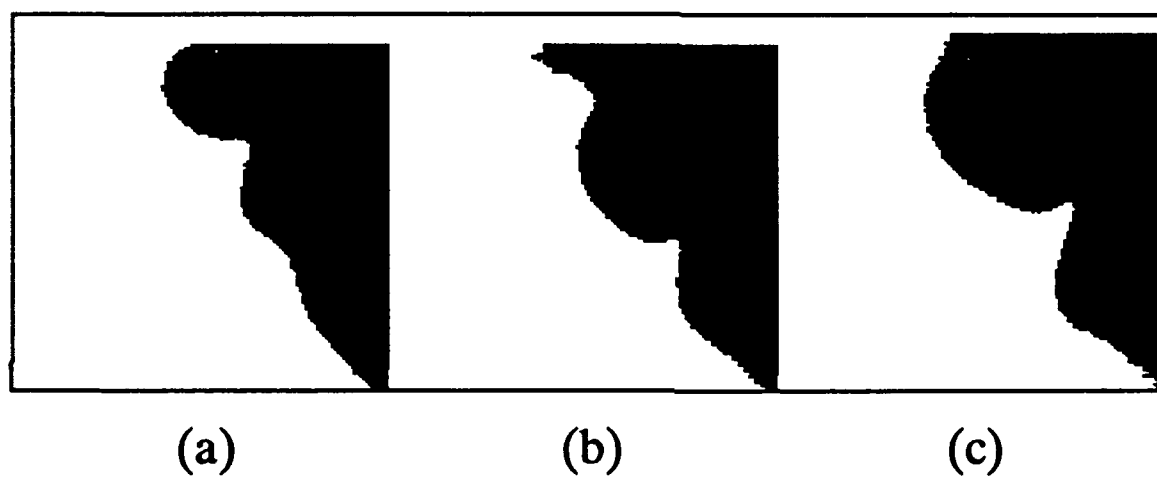


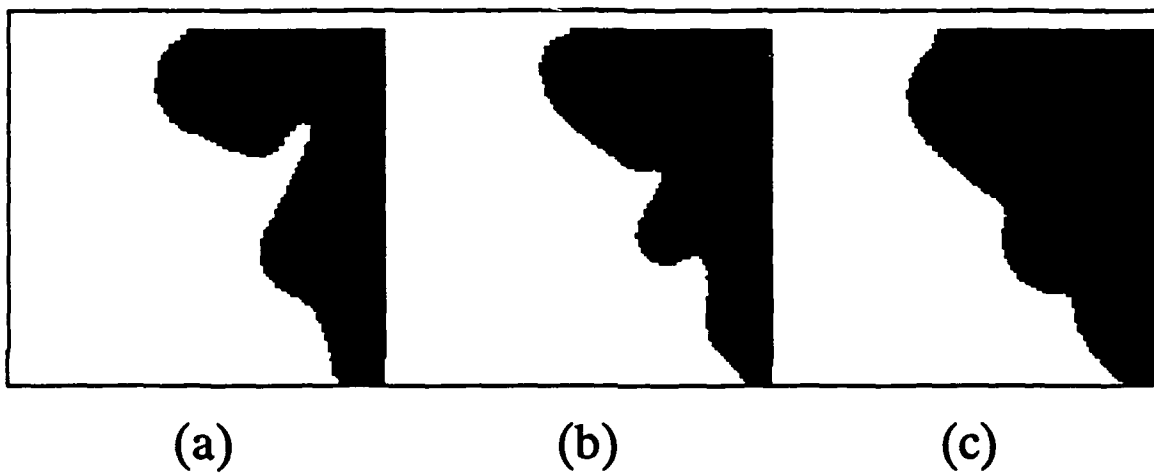
Figure 1. Schematic of the experimental apparatus.



Figures 2 (a)-(c). Binarized images of flame fronts at $Le=0.94$, $\delta_v/\delta_L=5.2$ and (a) $U_\theta/S_L=0.4$; (b) 0.6; (c) 0.7.



Figures 3 (a)-(c). Binarized images of flame fronts at $Le=0.94$, $U_\theta/S_L=0.7$ and (a) $\delta_v/\delta_L=3.4$; (b) 3.8; (c) 5.3.



Figures 4 (a)-(c). Binarized images of flame fronts at $U_0/S_L=0.8$, $\delta_v/\delta_L=2.8-4.2$ and (a) $Le=0.21$; (b) 0.94; (c) 1.79.

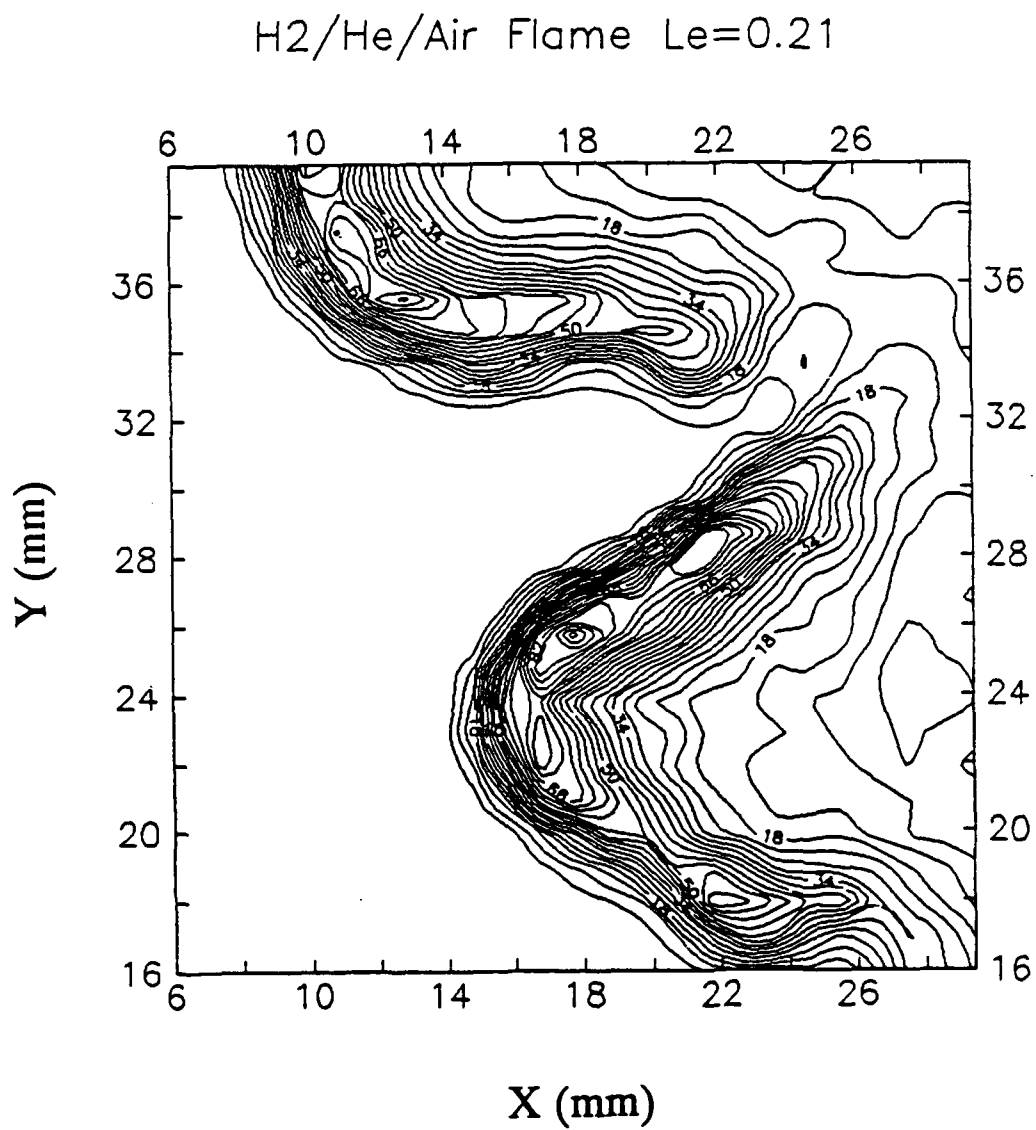


Figure 5 (a). Contour plot of OH LIF intensity for H₂/He/air flame ($Le=0.21$).

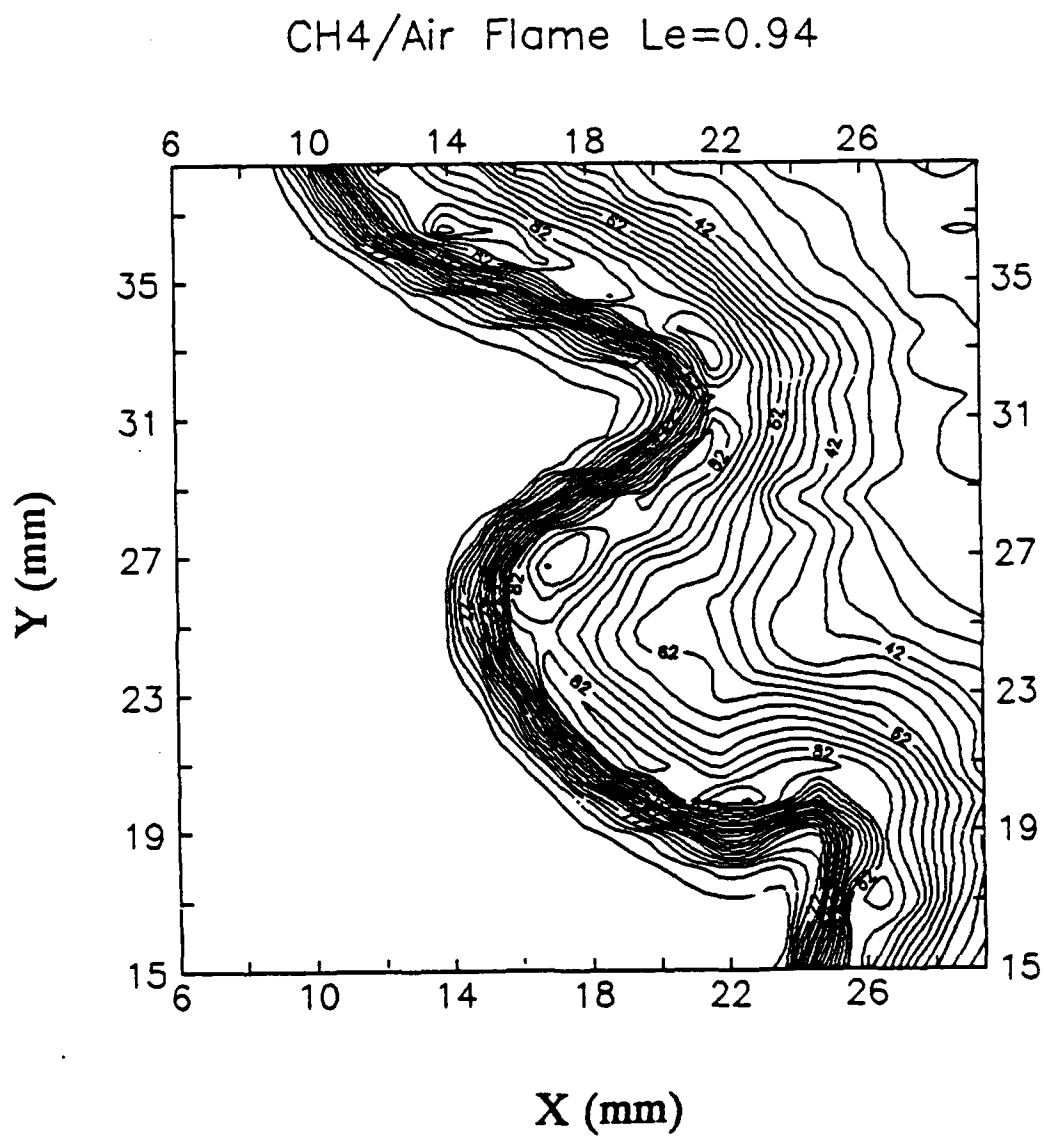


Figure 5 (b). Contour plot of OH LIF intensity for CH₄/air flame ($Le=0.94$).

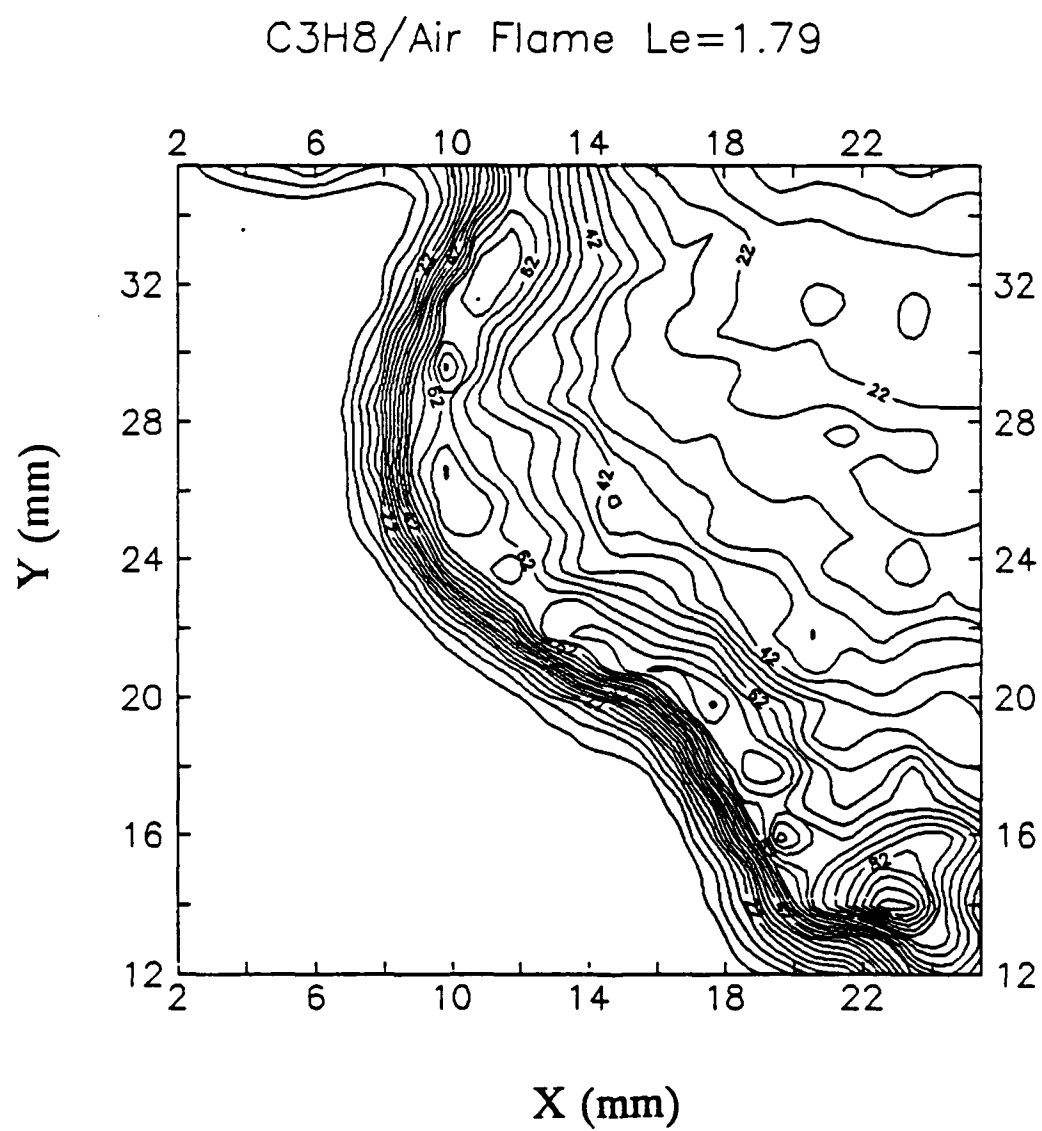
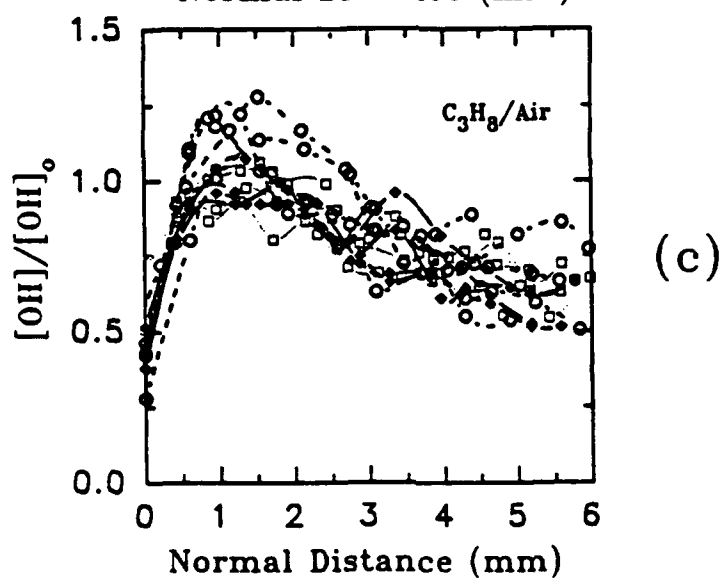
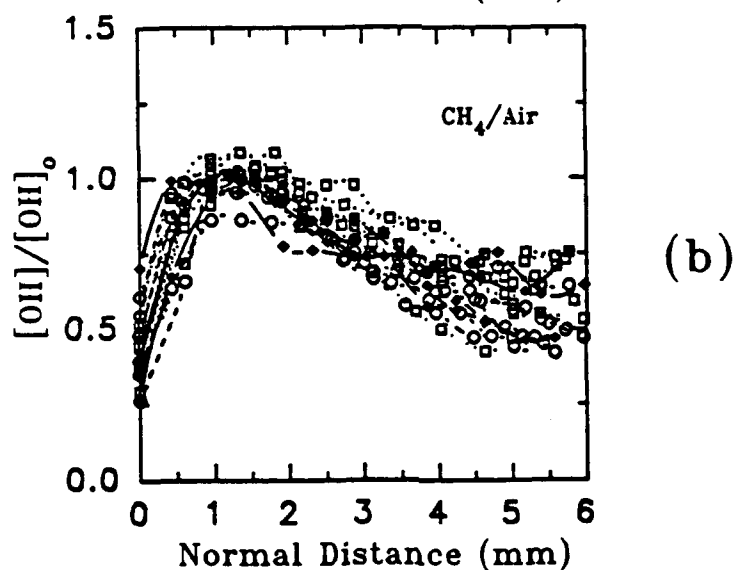
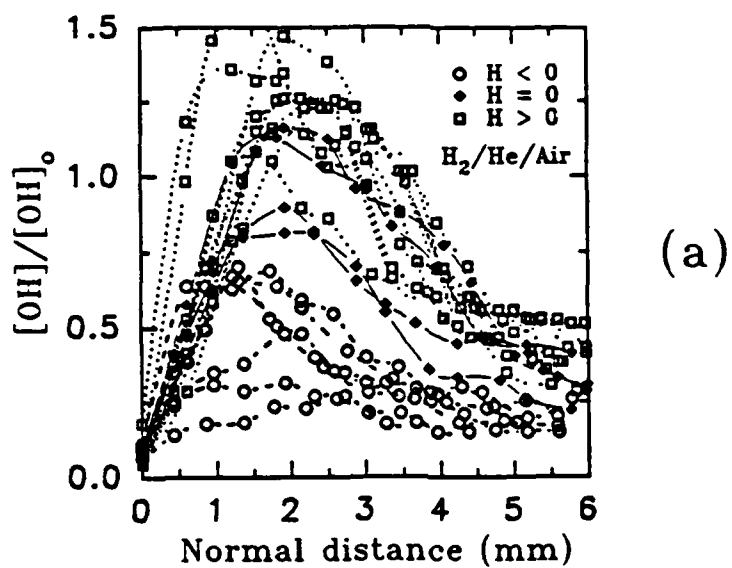


Figure 5 (c). Contour plot of OH LIF intensity for $\text{C}_3\text{H}_8/\text{air}$ flame ($\text{Le}=1.79$).



Figures 6 (a)-(c). OH LIF intensity profiles normal to the flame for (a) $Le=0.21$; (b) 0.94; (c) 1.79.

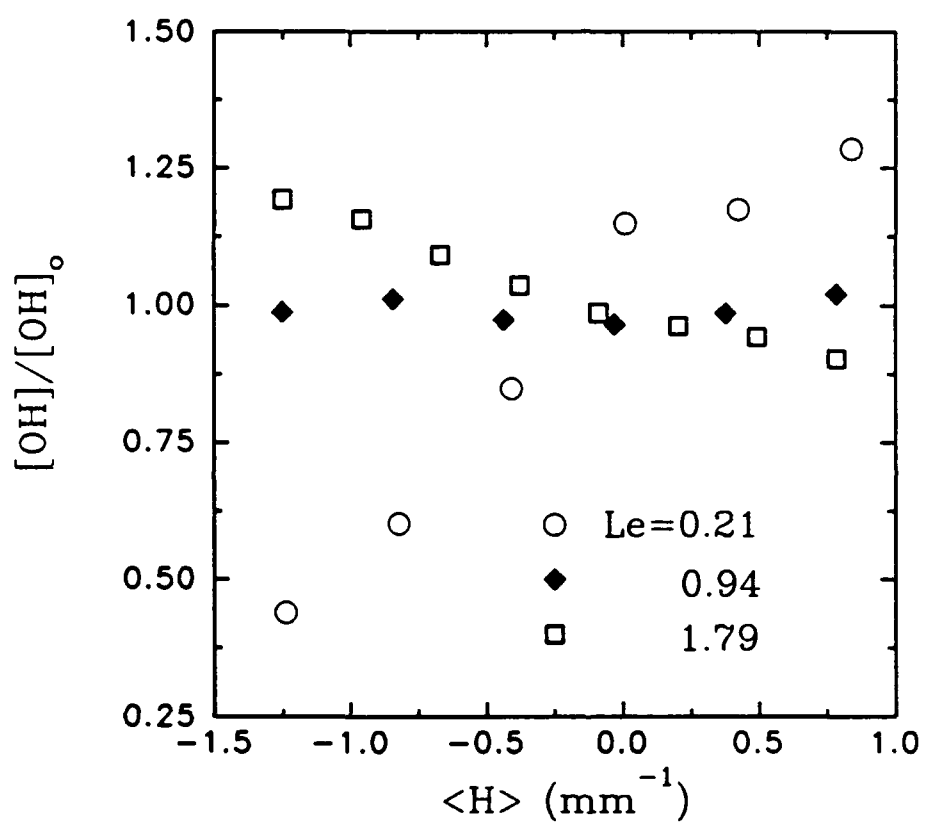


Figure 7. Averaged peak OH LIF intensity as a function of local flame curvature at various Lewis numbers.

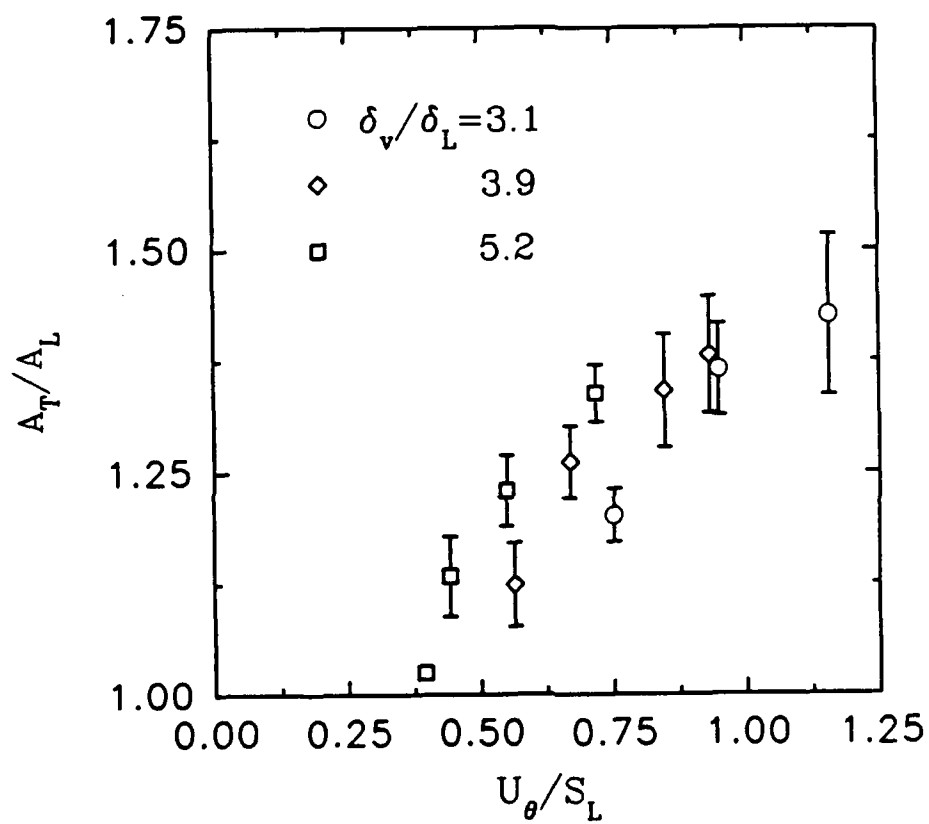


Figure 8. Flame area increase as a function of U_θ/S_L .

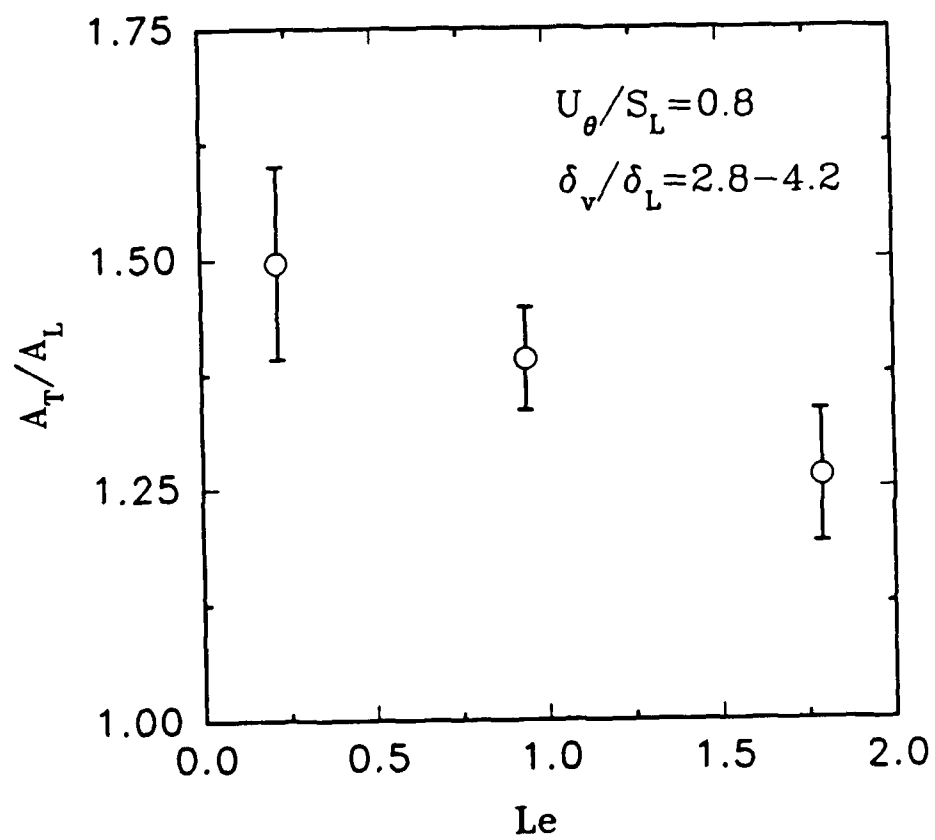


Figure 9. Effect of Lewis number on flame area.

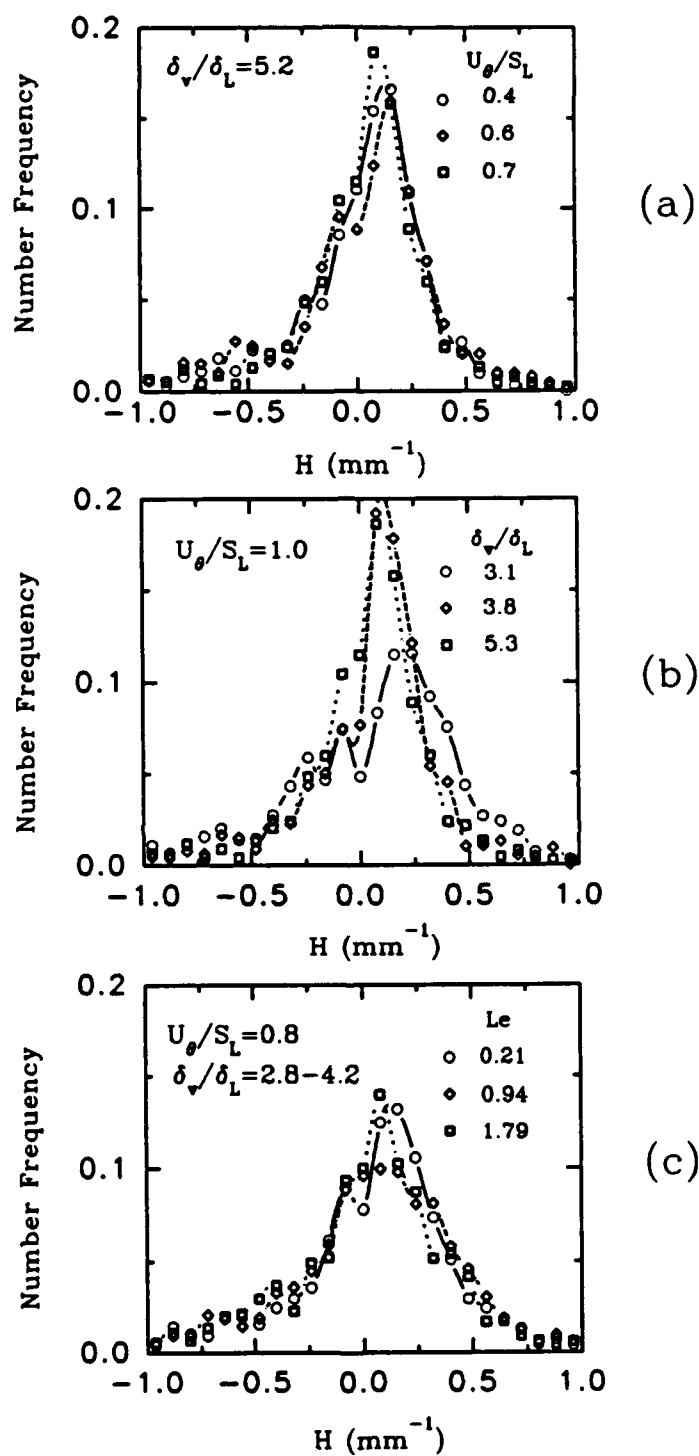


Figure 10. Flame curvature pdf's at various (a) U_e/S_L ; (b) δ_v/δ_L ; (c) Le .

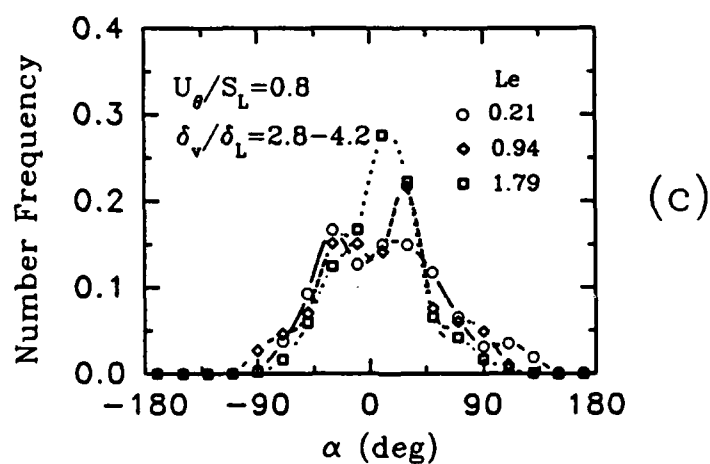
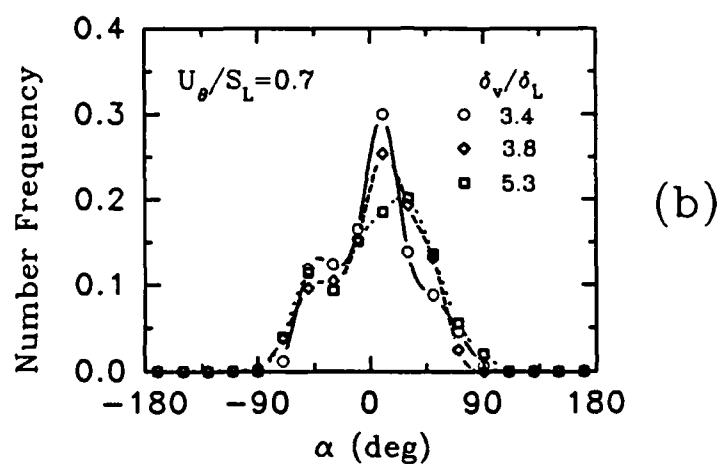
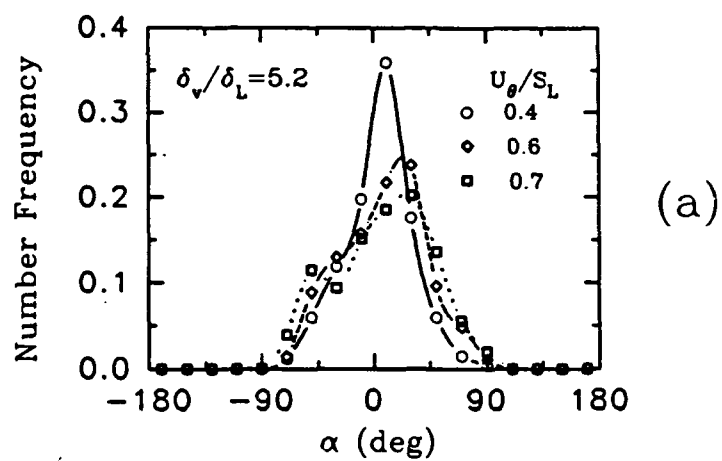


Figure 11. Flame orientation distribution at various (a) U_θ/S_L ; (b) δ_v/δ_L ; (c) Le .